

Nanoelectromechanical systems from two-dimensional materials

Cite as: Appl. Phys. Rev. **10**, 031302 (2023); doi: [10.1063/5.0106731](https://doi.org/10.1063/5.0106731)

Submitted: 29 June 2022 · Accepted: 25 April 2023 ·

Published Online: 19 July 2023



Paolo F. Ferrari,¹  SunPhil Kim,¹  and Arend M. van der Zande^{1,2,a} 

AFFILIATIONS

¹Department of Mechanical Science and Engineering, University of Illinois at Urbana-Champaign, Urbana, Illinois 61801, USA

²Materials Research Laboratory, University of Illinois at Urbana-Champaign, Urbana, Illinois 61801, USA

^aAuthor to whom correspondence should be addressed: arendv@illinois.edu

ABSTRACT

Micro- and nanoelectromechanical systems have numerous applications in sensing and signal transduction. Many properties benefit from reducing the system size to the nanoscale, such as increased responsivity, enhanced tunability, lower power consumption, and higher spatial density. Two-dimensional (2D) materials represent the ultimate limit of thickness, offering unprecedented new capabilities due to their natural nanoscale dimensions, high stability, high mechanical strength, and easy electronic integration. Here, we review the primary design principles, properties, applications, opportunities, and challenges of 2D materials as the building blocks of NEMS (2D NEMS) with a focus on nanomechanical resonators. First, we review the techniques used to design, fabricate, and transduce the motion of 2D NEMS. Then, we describe the dynamic behavior of 2D NEMS including vibrational eigenmodes, frequency, nonlinear behavior, and dissipation. We highlight the crucial features of 2D NEMS that enhance or expand the functionalities found in conventional NEMS, such as high tunability and rich nonlinear dynamics. Next, we overview the demonstrated applications of 2D NEMS as sensors and actuators, comparing their performance metrics to those of commercial MEMS. Finally, we provide a perspective on the future directions of 2D NEMS, such as hybrid quantum systems, integration of active 2D layers into nanomechanical devices, and low-friction interfaces in micromachines.

Published under an exclusive license by AIP Publishing. <https://doi.org/10.1063/5.0106731>

TABLE OF CONTENTS

I. INTRODUCTION	2	3. Diameter and thickness scaling	9
II. MATERIALS, GEOMETRY, AND FABRICATION		B. Resonance frequency tuning	10
OF 2D NEMS.....	2	C. Nonlinearity	11
A. Materials.....	2	1. Dynamic thermal fluctuations and amplitude calibration	12
B. Common configurations and fabrication strategies	4	2. Linear dynamic range in 2D NEMS	12
III. TRANSDUCTION, ACTUATION, AND DETECTION	5	3. Geometric nonlinearity in 2D NEMS	13
A. Free-space optical transduction	6	4. Bistability and switching	13
B. Electrical transduction	6	D. Energy dissipation	13
C. Other transduction schemes	7	1. Quality factor and dissipation in 2D resonators.....	14
1. Scan probe sensing.....	7	2. Comparing mechanisms of dissipation in 2D NEMS.....	16
2. Piezoelectric transduction	7	3. FPUT dissipation from nonlinear thermal fluctuations	17
3. Optical proximity transduction	7	V. COUPLED SYSTEMS.....	18
IV. DYNAMIC BEHAVIOR OF 2D NEMS.....	7	A. Parametric coupling between eigenmodes in a single resonator.....	19
A. Mechanical resonance frequency and lumped element models of 2D NEMS.....	7	B. Coupled resonators and mechanical metamaterials	20
1. Resonance mode harmonics and eigenmodes	8	C. Optomechanical coupling	21
2. Using eigenmodes to probe anisotropy and heterogeneity	9		

D. Hybrid coupled systems.....	21
1. Interlayer interactions in 2D heterostructures.	21
2. Coupled graphene-NEMS systems.....	22
VI. APPLICATIONS	23
A. Actuators	23
1. Switches	23
2. Oscillators	24
3. Speakers	24
B. Sensors	25
1. Pressure sensors	25
2. Acoustic and vibration sensors.....	27
3. Other types of sensors.....	27
C. Probing material properties.....	29
1. Mechanical properties	29
2. Thermal properties.....	29
3. Quantum phase transitions.....	29
VII. PERSPECTIVES: CHALLENGES AND OPPORTUNITIES.....	30
A. Challenges	30
B. Frontiers and new opportunities	31

I. INTRODUCTION

Microelectromechanical systems (MEMS) are a diverse and ubiquitous technology in smart electronics. Just as in Moore's law for transistors, there are many benefits and challenges to scaling down to smaller sizes to produce nanoelectromechanical systems (NEMS).^{1–5} The miniaturization of mechanical devices requires materials that are stable at small sizes and mechanically robust, yet electronically active. Yet, thin-film materials typically used in MEMS and NEMS have limits on how thin they can be before crystal grains or surface effects alter their structure and properties. For example, silicon forms native oxides of ~ 1 nm under ambient conditions.⁶ These surface effects begin to dominate the dynamics of NEMS as dimensions approach the nanoscale, setting practical lower limits on the size of devices.² Two-dimensional (2D) materials like graphene and molybdenum disulfide are stable down to a single molecular monolayer and thus overcome these traditional limits.

Figure 1 shows the relation between the unique material properties of 2D atomic membranes and the highly desirable performance in nanoelectromechanical systems. The broad class of 2D materials has diverse and outstanding electronic properties like high electronic mobilities exceeding $140\,000 \text{ cm}^2/\text{V s}$ ^{7,8} and strong light-matter interactions.^{9–12} At the same time, 2D materials are outstanding mechanical membranes. In plane, 2D materials are the strongest in the world, with high 2D Young's modulus (340 N/m for single-layer graphene) and high breaking strains ($\sim 25\%$), stronger than steel.¹³ Yet, because of their atomic scale thickness, 2D materials push the limits of low mass and flexibility, with bending moduli of $1.2\text{--}1.7 \text{ eV}$ for monolayer graphene,^{14–16} or about the stiffness of a cell wall.

Taken together, 2D materials represent both the ultimate limit of a molecular electronic thin film and a mechanical atomic membrane, making them ideal candidates for nanoelectromechanical systems, hereafter referred to as 2D NEMS. The nanoscale dimensions lead to devices that are orders of magnitude smaller, more responsive, and more tunable while consuming less power than conventional silicon MEMS, while also containing useful quantum properties and rich

nonlinear behavior. These enhanced properties lead to direct applications in sensors, actuators, and signal processing. Moreover, the high sensitivity makes 2D NEMS an ideal platform to probe nanoscale material mechanics, as well as coupling to electronic, magnetic, and quantum mechanical states.

In this review, we will focus on the utilization of graphene and other 2D materials as building blocks for resonant nanoelectromechanical systems, with a specific focus on nanomechanical drum head resonators. We will outline the design principles for producing NEMS from 2D material atomic membranes. We will then describe how the unique mechanics translate into dynamic device behavior, describe the applications that take advantage of these capabilities, and provide our perspective on the prospects, challenges, and opportunities for the future. We will not discuss the nanocharacterization of the surface and mechanical properties of 2D materials, as there are already many excellent reviews with this focus.^{17–23} We hope that our review will be informative to all researchers of 2D materials, which are curious about NEMS or are interested in applying NEMS techniques on their own research, as well as researchers in the MEMS/NEMS community wishing to learn how 2D NEMS compare.

II. MATERIALS, GEOMETRY, AND FABRICATION OF 2D NEMS

Few-layer graphene was first isolated and demonstrated as a field effect transistor in 2004,³¹ and single-layer graphene was first demonstrated as a mechanical resonator in 2007.³⁰ The first graphene resonator was fabricated by directly exfoliating graphite over pre-fabricated trenches in a silicon dioxide surface. By luck, some monolayer and few-layer flakes were suspended as membranes or plates over the trenches. Hereafter, we will primarily use the word membrane to discuss the suspended 2D region, though technically it may be a membrane or plate. We will discuss the transition between the two regimes in Sec. IV A 3. As outlined in Fig. 1, in the intervening years since this initial work, there has been explosive growth in the variety of 2D materials studied, and the sophistication of the materials synthesis and fabrication techniques used to engineer and characterize mechanical devices. Yet, because of common material requirements, all of these systems rely on similar geometries for clamping and schemes for transduction. Here, we will review these common considerations and how they affect 2D NEMS design.

A. Materials

As shown in Fig. 2(a), 2D materials such as hexagonal boron nitride (hBN), MoS₂, and black phosphorus all share the layered structure of graphene, though the exact chemistry, mass density, electronic properties, and symmetry may change. As a result, it is possible to fabricate suspended monolayer membranes out of nearly any air-stable 2D material. While these 2D materials have very different electronic structure and other properties, in the end, they all have very similar mechanical behavior, and resulting dynamic performance. For the majority of this review, we will focus on the common mechanics and dynamics, and give only a few select examples rather than reporting similar results for many systems. Below, we summarize examples of the different materials that have been studied with 2D NEMS. For a more in-depth comparison, we highlight a recent review, which collates and contrasts the relative performance of resonators from different 2D materials, as well as 1D NEMS such as carbon nanotubes.³²

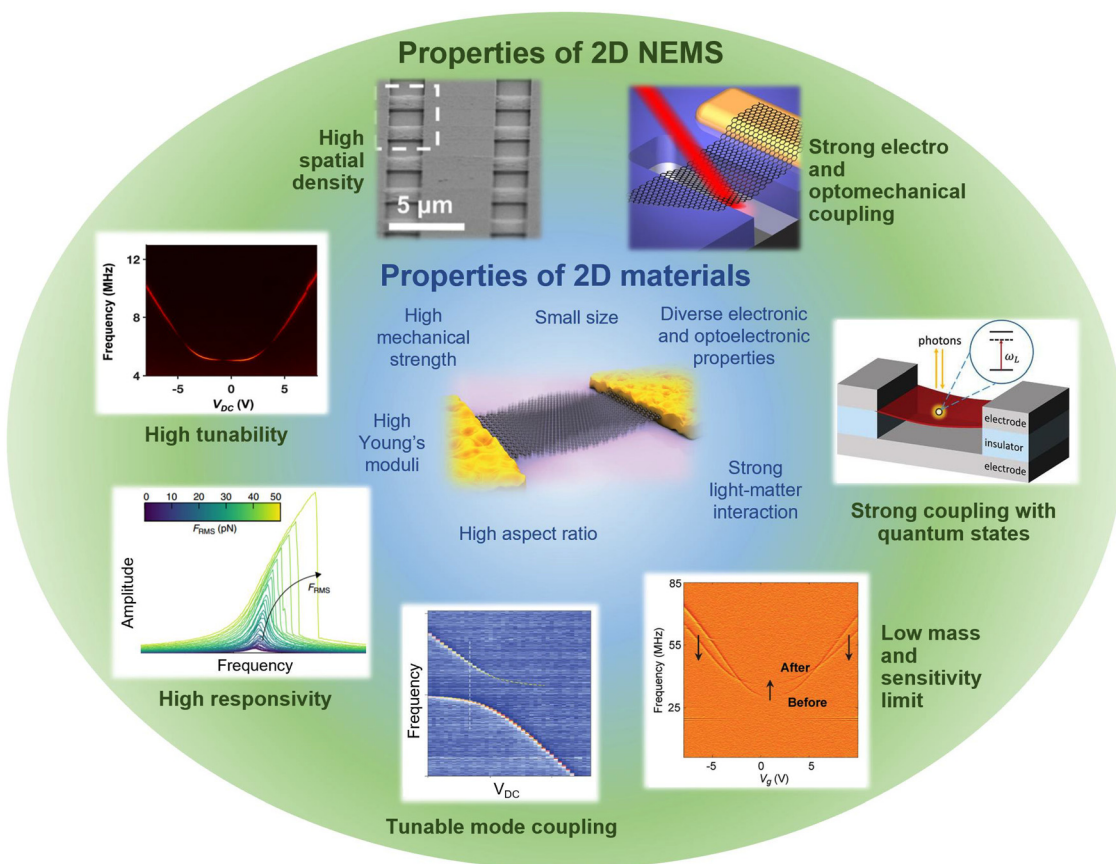


FIG. 1. Relation between the unique material properties of 2D atomic membranes and the desirable performance in nanoelectromechanical systems. The center image is a nanoscale representation of a monolayer graphene resonator.²⁴ Starting from the top, counter-clockwise: large-scale array of monolayer graphene resonators.²⁵ Reprinted with permission from van der Zande *et al.*, *Nano Lett.* **10**(12), 4869–4873 (2010). Copyright 2010 American Chemical Society, electrostatic frequency tuning curve of a monolayer graphene resonator.²⁶ Reprinted with permission from Kim *et al.*, *Nano Lett.* **20**(2), 1201–1207 (2020). Copyright 2020 American Chemical Society, amplitude vs frequency response of a graphene resonator under increasing pN drive forces.²⁷ Adapted with permission from Davidovikj *et al.*, *Nat. Commun.* **8**(1), 1253 (2017). Copyright 2017 Authors, licensed under a Creative Commons Attribution Unported License., electrostatic frequency tuning of two coupled eigenmodes in a graphene resonator.²⁸ Reprinted with permission from Mathew *et al.*, *Nat. Nanotechnol.* **11**, 747 (2016). Copyright 2016 Springer Nature Customer Service Center GmbH: Nature Nanotechnology, mass sensing of pentacene molecules as a shift in the electrostatic tuning.²⁹ Reprinted with permission from C. Chen and J. Hone, *Proc. IEEE* **101**(7), 1766–1779 (2013). Copyright 2016 IEEE, a single-photon emitter coupled to the vibrations of a suspended 2D membrane.³⁰ Reprinted with permission from Gao *et al.*, *Ann. Phys.* **532**(10), 2000233 (2020). Copyright 2020 Wiley-VCH GmbH, a graphene resonator representing electrical and optical transduction.³¹ Reprinted with permission from Bunch *et al.*, *Science* **315**(5811), 490–493 (2007). Copyright 2007 AAAS.

23 July 2023 15:16:56

Each 2D material provides access to unique electrical, optical, or quantum properties enabling new scientific opportunities and technological applications.³² As a brief summary, black phosphorous has a corrugated structure, leading to in-plane anisotropy in Young's modulus, electrical, and thermal conductivities.^{33–35} hBN is a 2D insulator with a wide bandgap of ~ 4.7 eV and is often used for encapsulating and passivating other air-sensitive 2D materials or reducing environmental dielectric disorder.³⁶ CrI₃ has ferromagnetic and antiferromagnetic phases depending on stacking and applied fields.^{37,38} Fabricating membranes of different material types either enables new device functionality taking advantage of those properties or utilizes the excellent sensitivity of 2D resonators to probe or transduce those properties, as we will explore in the sections below. For example, just in the family of graphene derivatives, there have been demonstrations of exfoliated,³⁰ chemical vapor deposition grown,²⁵ SiC epitaxially grown graphene,³⁹

reduced from graphene oxide,⁴⁰ and fluorinated graphene.⁴¹ In addition to graphene, there have been demonstrations of drum head membranes from monolayer or few-layer 2D materials, reflecting the diversity in properties of the entire material class. Demonstrations of resonators from 2D semiconductors include transition metal dichalcogenides (TMDCs) like MoS₂,^{42–49} WSe₂,⁵⁰ MoSe₂,⁵¹ WTe₂,⁵² and black phosphorus,^{33–35} or As₂S₃.⁵³ Resonators from insulators include hexagonal boron nitride^{54–56} or oxidized TaS₂.⁵⁷ Recently, there are demonstrations from metallic MXenes like Ti₃C₂T_x.⁵⁸ Then, there are resonators probing more exotic material properties including magnetic 2D materials CrI₃,³⁸ FePS₃,⁵⁹ and Cr₂Ge₂Te₆,⁶⁰ or superconducting 2D materials like NbSe₂ and TaS₂.^{59,61–63} It is also possible to make resonators from 2D materials heterostructures such as bimorphs from graphene-MoS₂,^{64,65} graphene-hBN,^{66,67} encapsulated graphene-NbSe₂-graphene,⁶² or WSe₂-CrI₃-graphene,³⁸ and magnetic

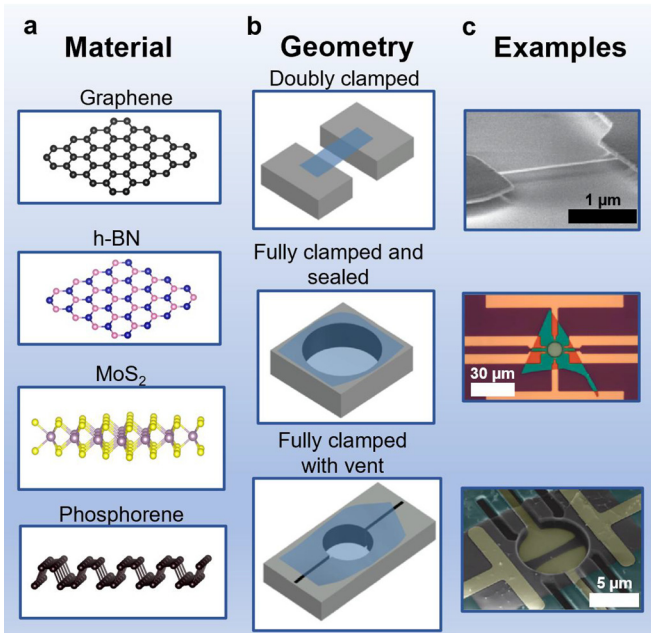


FIG. 2. Structure of 2D mechanical resonators. (a) Schematics of monolayer 2D materials: graphene, hBN, MoS₂, and black phosphorus. (b) Schematics of three different geometries for clamping membranes: Doubly clamped, Fully clamped and sealed, and Fully clamped with vent. (c) Images of fabricated mechanical resonators with different materials and geometries.^{54,80,85} Top figure: Reprinted with permission from Chen *et al.*, Nat. Nanotechnol. 4(12), 861–867 (2009). Copyright 2009 Springer Nature Customer Service Center GmbH: Nature Nanotechnology; Center FIG: Adapted with permission from Zheng *et al.*, Microsyst. Nanoeng. 3(1), 17038 (2017). Copyright 2017 Authors, licensed under a Creative Commons Attribution Unported License. Bottom figure: adapted with permission from Mathew *et al.*, Nat. Nanotechnol. 11, 747 (2016). Copyright 2016 Springer Nature Customer Service Center GmbH: Nature Nanotechnology.

Cr₂Ge₂Te₆ heterostructures.⁶⁰ Finally, there has been a recent trend in leveraging similar techniques to explore quasi-2D membranes made from materials like complex oxides such as SrTiO₃ and SrRuO₃,^{68–70} or BSSCO.^{71,72}

B. Common configurations and fabrication strategies

Figures 2(b) and 2(c) show schematics and images of examples of three common configurations used for 2D NEMS: a doubly clamped resonator, a fully clamped and sealed resonator, and a fully clamped and vented resonator. While many different shapes and configurations have been explored, generally the geometry of 2D NEMS may be categorized by (1) the clamping conditions (as is common in beam theory) of the suspended diaphragm, (2) by whether they form sealed or vented cavities with respect to their environment, and (3) by whether and how they are electrically contacted and gated (which defines the methods of transduction and tuning). While this last category is not strictly geometric, the presence of and location of electrodes can alter how the 2D material is clamped. For example, the first image in Fig. 2(c) shows a suspended graphene ribbon clamped underneath two gold electrodes. In addition, the presence and location of gates alters the symmetry of the drive. For instance, the bottom image in

Fig. 2(c) shows a graphene membrane whose gate consists of two separate electrodes. Actuation of only one electrode, or use of different voltages in the two electrodes, breaks the symmetry of actuation and favors different eigenmodes.

Clamping geometry is important because it defines how stress is distributed and what eigenmodes are allowed. Early studies utilized 2D monolayers doubly clamped by electrodes or trenches, where two edges are clamped, and two edges are free. However, the small asymmetric stress left over from transfer and asymmetric adhesion combined with the negligible bending stiffness of few-layer graphene lead to inhomogeneous rippling or buckling of the diaphragm,^{73–75} dramatically affecting the local stiffness^{25,30} and thus the predictability of the eigenmodes.⁷⁶ In contrast, fully clamped diaphragm where all edges are attached to the substrate provides much more symmetric distribution of stress, smoothing many of the ripples in the graphene, leading to more predictable eigenmodes.²⁵ However, some rippling or asymmetry in the fully clamped geometries is still present and difficult if not impossible to fully remove in the monolayer limit.^{54,64,77} Taken together, most 2D NEMS studies now focus on fully clamped membranes for the improved control.

The second important categorization is whether the membrane forms a sealed or vented cavity with respect to the environment. If a membrane is clamped on all sides over a hole that does not go through the substrate [second example in Figs. 2(b) and 2(c)], then gas in the hole is sealed inside, causing the graphene to inflate like a balloon when measured under vacuum.⁷⁸ While sealing the cavity has useful applications for pressure sensors, discussed later, in most other cases, trapped gasses, liquids, or processing residue cause undesirable frequency tuning or damping. There are several strategies for venting the cavity while maintaining the mechanically preferred full clamping. As shown in the third example in Figs. 2(b) and 2(c), the most common strategy is to lithographically pattern small trenches to come off the side of an otherwise fully clamped membrane.^{26,51,79–82} Other demonstrated strategies include a through hole etched in the substrate⁴⁰ or a freely suspended membrane with no underlying substrate.⁸³

An important consideration particular to monolayer 2D NEMS that affects both the design of clamping and fabrication procedures is the bending energy is much smaller than the adhesion energy to the substrate, at least for typical devices, where lateral size is larger than 1 μm. As a result, the graphene wraps onto the clamped edges of the suspended structure, causing it is a residual tensile stress.⁷⁸ The adhesion strength of the graphene is ~0.1 J/m²,⁸⁴ so by balancing the line tension/stress at the clamping edges, the resulting stress in the graphene is typically ~0.1 N/m. In devices without side-walls, such as when the material is doubly clamped underneath electrodes, the stress is typically ~0.03 N/m at room temperature.⁸⁵ However, there are more complex methods that provide higher tensions. These methods include stretching the material by thermal contraction of the supporting electrodes,⁸⁵ using thermal expansion rings⁸⁶ or comb-drive actuators.⁸⁷

In most cases, variations on one of three fabrication processes are used to fabricate 2D NEMS. In the first approach, trenches or holes are prefabricated into a substrate; then, 2D materials are directly exfoliated onto the surface.³⁰ Some fraction of 2D materials, either monolayer or few layers, will stick and be suspended over the pre-existing features. As with any MEMS, the suspended structures are delicate, and so cannot undergo any liquid processing after suspension. Thus, any additional features like electrical contacts must be prefabricated

on the surface or made using shadow mask lithography after suspension. The advantage of this approach is that it guarantees the cleanest 2D materials, which is important for applications requiring high electronic mobility or low added mass.⁸⁸ The disadvantage of this approach is the low statistics of success, making it only useful for scientific study. In the second approach, the 2D material is transferred onto a flat substrate, then shaped and electrically contacted using lithography, and then finally suspended by etching the underlying sacrificial substrate and performing a critical point dry.⁸⁵ The second approach is most similar to how conventional MEMS/NEMS are fabricated, and is scalable when using large-area CVD materials.^{25,39} However, this approach has some 2D material specific limitations, which limit its utility. First, it is difficult to remove the lithographic processing residue, because many conventional cleaning processes used in MEMS will destroy the 2D membranes. Second, liquid etchants like buffered oxide etch (BOE) commonly used in MEMS processing can actually wick along the 2D-substrate interface,⁸⁹ making it difficult to control the etch rate or define structure size unless the entire 2D material is being suspended. The third approach consists of using polymer-assisted transfer techniques, either CVD materials or

prefabricated heterostructures that may be aligned and transferred onto prefabricated features.^{25,26,64} The advantage of this approach is that it has the highest yield and scalability, and it allows the most flexibility and control over what the membrane is. The disadvantage is that it still makes it difficult to remove processing residue on the 2D surfaces. Annealing the 2D materials in vacuum or argon/hydrogen forming gas does remove much of the processing residue, but the changes in adhesion and thermal expansion lead to the membranes slipping at high temperature, which affects the stress and morphology.⁷³

III. TRANSDUCTION, ACTUATION, AND DETECTION

Many two-dimensional materials are semi-transparent^{11,12} and electrically conductive,^{7,8,41} enabling diverse optical, electrical, or scan probe methods of transduction to actuate and detect the motion. Of course, it is also possible to use different mechanisms to actuate vs sense the motion. For example, Fig. 3(a) schematically shows a common measurement paradigm where the 2D membrane is electrically actuated and the motion is optically sensed. In this section, we review the most common transduction schemes utilized for 2D NEMS.

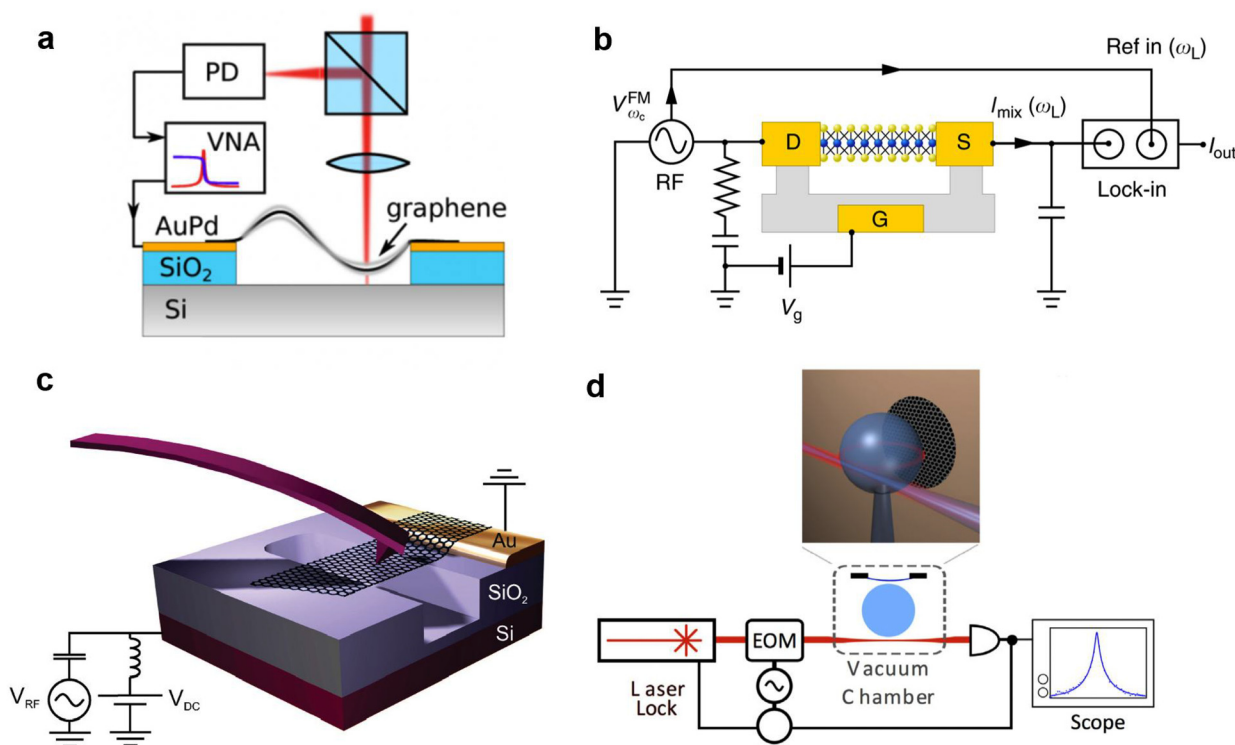


FIG. 3. Transduction schemes for actuation and detection of 2D NEMS. (a) Optical transduction of a graphene resonator.⁷⁷ Reprinted with permission from Davidovikj *et al.*, Nano Lett. **16**(4), 2768–2773 (2016). Copyright 2016 American Chemical Society. A 633 nm laser focused on the sample detects the motion by the dynamic change in reflectance. (b) Electrical transduction of a MoS₂ resonator.⁴⁵ Reprinted with permission from Manzeli *et al.*, Nat. Commun. **10**(1), 4831 (2019). Copyright 2019 Authors, licensed under a Creative Commons Attribution Unported License. A frequency-modulated voltage $V_{\omega_c}^{FM}$ applied on one of the contacts of the MoS₂ excites the motion through the electrostatic force between the membrane and the gate under voltage V_g . The dynamic strain in the MoS₂ modulates the current $I_{mix}(\omega_L)$ by the transconductive effect, measuring the amplitude of vibration. (c) Scanning probe sensing of a graphene resonator motion by an AFM cantilever.⁷⁶ Reprinted with permission from Garcia-Sanchez *et al.*, Nano Lett. **8**(5), 1399–1403 (2008). Copyright 2008 American Chemical Society. (d) Proximity transduction of a graphene membrane.¹¹¹ Adapted with permission from Cole *et al.*, Phys. Rev. Appl. **3**, 024004 (2015). Copyright 2015 American Physical Society. A silicon microsphere detects the motion of the graphene by the change in the optical coupling to the sphere and the graphene membrane vibrates. The sphere sustains whispering-gallery optical modes, which are excited by a tapered fiber coupled to the sphere and to a laser source. The vibrations of the graphene induce modulations in the transmitted light.

A. Free-space optical transduction

Free-space optical transduction is perhaps the simplest method for actuating and detecting motion in 2D NEMS because it has the fewest sample requirements with no electrodes or gates needed.³⁰ For the same reasons, free-space optical transduction is not feasible for technological integration, and is mostly used to characterize the mechanical properties of different 2D materials, and for explorations of light-matter interactions. Because the density of devices can be much higher when no electrodes or other components are needed, optical transduction is ideal for examining of the size scaling of 2D atomic membranes, which often requires comparison of many different membranes.^{25,30,90,91}

For optical actuation, a modulated free-space laser is focused on the suspended 2D membrane. The modulation of absorbed light causes periodic thermal expansion and relaxation of the membrane, leading to out-of-plane mechanical vibration. The laser also applies optical pressure to the 2D membrane, but the forces are orders of magnitude smaller than the thermal forces, and may usually be ignored. For optical detection, another laser with a different wavelength is focused on the suspended membrane. Figure 3(a) illustrates the mechanism of optical detection in a graphene resonator. The reflection of light off the 2D membrane and Si substrate underneath forms a Fabry-Pérot interferometer. The change in path length as the 2D membrane moves results in a time varying change in the reflected light, which is monitored by a fast photodetector. The interference conditions and resulting signal magnitude depend sensitively on the gap size and the presence of any other thin-film layers under the suspended membrane. It is important to take the interference conditions into account when designing new 2D NEMS systems for optical transduction.⁹²

B. Electrical transduction

Integrating NEMS into most technologies requires all electronic transduction. Most 2D materials are electrically active, so it is easy to integrate them with electrodes and gates for actuation and sensing of motion. Figure 3(b) shows a common geometry for electrical transduction. The 2D material is contacted by source and drain electrodes with a gate under the membrane. Voltages applied to the gate actuate the membrane, and motion is detected by monitoring the current through the membrane.⁸⁵ While electrical integration adds many desirable capabilities, it is more complex to design the layout of the devices, so many studies of basic materials characterization or parametric studies usually use the simpler optomechanical measurements. In addition to electrostatic actuation of 2D NEMS, which is detailed below, it is possible to electrically actuate a 2D membrane by applying current to it in the presence of a magnetic field via the Lorentz force, although this method is much less common since it requires a magnet or coil.⁹³

Electrostatic actuation is achieved via the application of a voltage on the membrane with respect to a local or global back gate located underneath the membrane. Just as with most capacitive MEMS, the gate simultaneously enables electrostatic actuation and tuning of the tensile stress in the membrane. A combination of a DC voltage V_{DC} and radio frequency voltage V_{RF} are applied between the gate and drain, creating a static F_{DC} and oscillating F_{RF} attractive force between the membrane and the gate, given by

$$F_{DC} = \frac{1}{2} \frac{\partial C_g}{\partial z} V_{DC}^2, \quad (1)$$

$$F_{RF}(t) = \frac{\partial C_g}{\partial z} V_{DC} V_{RF} \cos(\omega t), \quad (2)$$

where applying the commonly used rough approximation of an initially flat membrane and a parallel plate model, C_g is the capacitance of the membrane with respect to the gate and $\frac{\partial C_g}{\partial z}$ is the change in capacitance as the membrane moves. The static force tensions the membrane, while, if driven at the right frequency, the oscillating force causes the membrane to resonate. If only actuation is desired, such as in the case shown in Fig. 3(a), it is sufficient to use a global back gate wherein the gate voltage is applied to the conducting substrate, and only a single electrode is needed to contact the membrane.

Electronic readout in 2D NEMS typically takes advantage of the electronic properties of the 2D materials for transconductive sensing.⁸⁵ Transconductive sensing leverages the semimetal or semiconducting properties of 2D materials, where the material conductance G depends on the carrier density in the material, which is modulated by changing the Fermi level. The conductivity of a 2D membrane is thus a function of both the applied gate bias and the capacitance, which means there is a change in the conductance as the membrane moves with respect to the gate. Applying a bias V_{ds} through a membrane using source and drain electrodes enables detection of the motion as a change in conductivity, resulting in an oscillating transconductive current I_{trans} given by Chen *et al.*,⁸⁵ Sazonova *et al.*,⁹⁴ and Xu *et al.*⁹⁵

$$I_{trans}(t) = V_{ds} \frac{dG}{dV_{DC}} V_{RF} \cos(\omega t) - V_{ds} \frac{dG}{dV_{DC}} \frac{z_0 \cos(\omega t)}{d} V_{DC}. \quad (3)$$

Here, ω is the angular frequency, z_0 is the amplitude of motion, and d is the equilibrium distance between the resonator and the back gate. The first term in this equation is a background electronic current coming from modulation of the carrier density by the oscillating voltage V_{RF} , while the second term rises from modulation of the carrier density as the membrane moves with respect to the gate.

We note that the transconductance sensing is different from the capacitive or piezoresistive electrical sensing techniques more commonly used in typical MEMS. Piezoresistivity depends on a strain-induced change in band structure leading to a change in conductivity. Typically, the changes in strains in 2D NEMS are very small, so piezoresistivity does not play a significant role. Capacitive sensing comes directly from the charge flowing on and off the membrane as it moves with respect to the gate. Assuming that the applied RF voltage is much smaller than the DC voltage, the capacitive current I_{cap} is given by Xu *et al.*⁹⁵

$$I_{cap}(t) = -\omega C_{tot} V_{RF} \sin(\omega t) - \omega V_{DC} C_g \frac{z_0 \sin(\omega t)}{d}. \quad (4)$$

Here, C_{tot} is the total capacitance of the entire device with respect to the gate, including the parasitic capacitance of the source-drain electrodes in the case of a non-local gate. The first term is a purely electrical current rising from capacitive charging and discharging by the oscillating voltage V_{RF} , whereas the second term arises from the charging and discharging from the mechanical vibration as the membranes moves with respect to the gate.

The transconductive current is typically orders of magnitude larger than the capacitive current rising from device motion. However,

because of the small devices size, the signals from both techniques are small compared with the parasitic currents at the same frequency coming from parasitic capacitance, particularly when a global gate is used. There are a few strategies for overcoming this limitation. First, the parasitic capacitance may be minimized by fabricating a local gate under the membrane.^{28,95–97} The use of local gates can have the added benefit of enabling multiple gates to actuate specific eigenmodes with different symmetry within the membrane.⁸⁰ Second, using transconductance allows amplitude or frequency modulation, where the signal from the mechanical motion mixes to a different, usually <1 kHz signal.^{85,94,98} This low-frequency modulated signal allows readout of the amplitude of motion at a frequency where the parasitic capacitance no longer dominates. Finally, when measuring at low temperature and operating the device near a Coulomb blockade peak, the transconductance dG/dV_{DC} and thus the current I_{trans} become orders of magnitude larger.^{99,100}

C. Other transduction schemes

Optical and electrical transduction make up the vast majority of 2D NEMS studies. However, there are other less commonly used approaches as well, which have specific strengths.

1. Scan probe sensing

Figure 3(c) shows the concept behind scan probe sensing of 2D motion.¹⁰¹ An atomic force microscope (AFM) tip is touched on the surface of a 2D membrane. When the membrane is driven electrostatically or piezoelectrically, the cantilever also vibrates and reads out the motion. This approach may be used to measure small displacements off the 2D material resonance¹⁰¹ or, by scanning the tip, may be used to map out the eigenmodes at below the optical diffraction limit, both of which will be discussed later.⁷⁶

2. Piezoelectric transduction

Piezoelectricity is commonly used in MEMS and NEMS for electromechanical transduction because it scales well with system size and can be used for simultaneous actuation and sensing, making it useful for GHz frequency devices.^{102,103} Some 2D materials like hBN and MoS₂ are not piezoelectric in the bulk, but become piezoelectric as monolayers due to a breaking of the in-plane mirror symmetry.¹⁰⁴

For example, from AFM indentation measurements, the forward piezoelectric coefficient of MoS₂ is approximately $e_{11} = (2.9) \times 10^{-10} \text{ C m}^{-1}$, similar to the values estimated from theory of $e_{11} = (3.06) \times 10^{-10} \text{ C m}^{-1}$.¹⁰⁴ From these values, the transduction conversion efficiency $k^2 = (\text{stored mechanical energy}) / (\text{supplied electrical energy})$, also known as electromechanical coupling coefficient, should be $\sim 1\%$ up to 1 GHz.¹⁰⁵ This value is comparable to most piezoelectric MEMS materials, which cite k^2 between 1% and 10%,¹⁰⁶ though higher values are achievable.^{107–109} However, the absolute magnitude of the signal coming from a monolayer is small, and other external factors such as contact resistance¹¹⁰ may significantly reduce the effective measured k^2 . Recent papers claim evidence of resonant in-plane piezoelectric transduction of monolayer MoS₂ and monolayer MXene Ti₃C₂T_x NEMS, but the results are problematic. A more recent paper on MXene resonators, but not piezoelectricity, discusses the issues in the piezoelectricity papers depth.⁵⁸ There have not been any conclusive

studies showing a resonant 2D NEMS, which is actuated or sensed piezoelectrically, which would require demonstration of resonance in the absence of a gate.

3. Optical proximity transduction

While free-space optical detection is excellent for fundamental studies, integrating 2D NEMS into photonic systems such as high-finesse microcavities, photonic waveguides, and optical fibers is useful for many high-bandwidth applications in the same way as electrical integration.

As one example, Fig. 3(d) shows a schematic for reading the dynamic thermal fluctuations of a graphene resonator by positioning a Si microsphere above it.¹¹¹ A tapered optical fiber, positioned close to the membrane, excites an optical mode of the microsphere. The evanescent field of the optical mode couples to the graphene resonator by dispersive and dissipative mechanisms, shifting the frequency and linewidth of the optical mode resonance as the gap between the sphere and graphene diminishes. Other examples of evanescent field readout were demonstrated for hBN⁵⁶ and carbon nanotube resonators.¹¹² The displacement sensitivity of this technique is $\sim 100 \text{ fm/Hz}^{1/2}$, comparable but still not as low as using free-space interferometric detection.¹¹³

IV. DYNAMIC BEHAVIOR OF 2D NEMS

In this section, we will review the dynamic behavior of 2D NEMS and highlight their links to the mechanical properties of 2D materials. The interplay between the molecular-scale thickness of the 2D membranes, high mechanical strength, and unique material properties gives rise to very unusual behavior, which is not found in other M/NEMS. In particular, the high responsivity of 2D membranes makes the resonances highly tunable to applied forces or external perturbations, as well as more susceptible to nonlinear effects and thermomechanical effects, affecting both the dynamic behavior and energy dissipation.

A. Mechanical resonance frequency and lumped element models of 2D NEMS

In the simplest model, 2D NEMS behave as membranes or plates, where the out-of-plane resonance eigenmodes are well described by continuum mechanics. In the linear regime, the dynamics of each eigenmode are well described by a lumped element differential equation for a driven mass-spring-damper system. These quantities rise from the differential equation of a damped harmonic oscillator

$$m_{\text{eff},i}\ddot{z} + b_{\text{eff},i}\dot{z} + k_{\text{eff},i}z = F_d \cos(\omega t). \quad (5)$$

According to this model, the i -th eigenmode has a lumped element effective membrane stiffness $k_{\text{eff},i}$ rising from the combination of the distributed stretching and bending energies, an effective mass $m_{\text{eff},i}$ originating from the inertia of the distributed motion of atoms, and an effective damping coefficient $b_{\text{eff},i}$ corresponding with distributed coupling of the coherent motion in the eigenmode to either the outside system or to other modes or phonons in the resonator. All parameters depend on the number of layers, initial stress, material type, added mass from processing, clamping boundary conditions, and membrane geometry, as well as the specific eigenmode that is being excited. Derivations for using continuum mechanics to predict frequencies and lumped element analysis can be found in many elasticity and MEMS textbooks,^{114,115} and will not be Reprinted here. In general, the natural

angular frequency of the i th eigenmode of a mechanical oscillator is related to these effective parameters by

$$\omega_i = \sqrt{\frac{k_{\text{eff},i}}{m_{\text{eff},i}}} \quad (6)$$

In this review, all frequency equations will be presented in terms of the angular frequency ω , while many experiments and results will be presented in terms of the cyclic frequency f , where $f = \omega/2\pi$.

Because of the discrete nature of the thickness of 2D resonators, when modeling their mechanics, it is often more natural to use the material parameters normalized by the number of layers, such as the 2D density ρ_{ML} and 2D Young's modulus Y . For instance, in graphene, $\rho_{ML} = \rho_{3D}t_{IL} = 0.76 \text{ mg/m}^2$, where $\rho_{3D} = 2.26 \text{ g/cm}^3$ and $t_{IL} = 0.34 \text{ nm}$ is the interlayer center-to-center distance; similarly, $Y = Et_{IL} \approx 340 \text{ N/m}$, where $E \approx 1 \text{ TPa}$ is the in-plane 3D Young modulus.¹³

In the mono- to few-layer limit and under most experimental conditions, 2D NEMS are best described as tensioned membranes, but in thicker structures, they transition to plate behavior. The transition between these regimes depends on geometry, aspect ratios, and built-in tension, which we will explore further in Subsection IV A 3. For example, for a circular membrane, the resonant angular frequency of the fundamental eigenmode ω_1 is given by Wah¹⁶

$$\omega_1^{\text{membrane}} = \frac{2.404}{R} \sqrt{\frac{\sigma_0}{t_{IL}\rho_{ML}N}}, \quad (7)$$

where R is the radius, σ_0 is the initial 2D tensile stress in units of N/m on the membrane, and N is the number of layers. Meanwhile, for a circular plate of the same dimensions, the frequency is given by Wah¹⁶

$$\omega_1^{\text{plate}} = \frac{10.21}{2R^2} \sqrt{\frac{Yt_{IL}^2N^2}{3\rho_{ML}(1-\nu^2)}}, \quad (8)$$

where ν is the Poisson ratio.

In many cases, these two continuum models for the stiffness hold. However, in the monolayer limit, new phenomena become important, which impact the effective stress, such as the self-tensioning through sidewall adhesion and nonlinear thermal fluctuations. Moreover, it is difficult to perfectly control the stress in the membrane, leading to nonlinear geometric effects like anisotropic stress, rippling and buckling which affect the mechanical stiffness, resonance frequencies, and eigenmode shapes.¹¹⁷ In IV A 1–IV A 3, we will review the resonance behavior of 2D NEMS in the perspective of linear continuum mechanics, then tackle the more complex behavior in future sections.

1. Resonance mode harmonics and eigenmodes

Figure 4(a) shows the spectrum of the fundamental resonance mode for a circular heterostructure of graphene and MoS₂ monolayers, which is typical for nearly any 2D resonator.⁶⁴ The fundamental mode appears as the first resonance peak centered on $f_1 = 15.6 \text{ MHz}$. As shown in Fig. 4(b), the extended spectrum displays the higher harmonic peaks f_2, f_3, \dots, f_6 . The dashed lines labeled as (m, n) represent the ideal frequencies from a circular tensioned membrane $f_{m,n} = \alpha_{m,n}f_{0,1}$, where $\alpha_{m,n}$ is a numeric constant corresponding to azimuthal node number m and radial node number n . Overall, the measured values follow the predicted frequencies for the first few eigenmodes, showing the tensioned membrane model holds. However, the higher harmonics show mode splitting and become increasingly different from the predicted values.

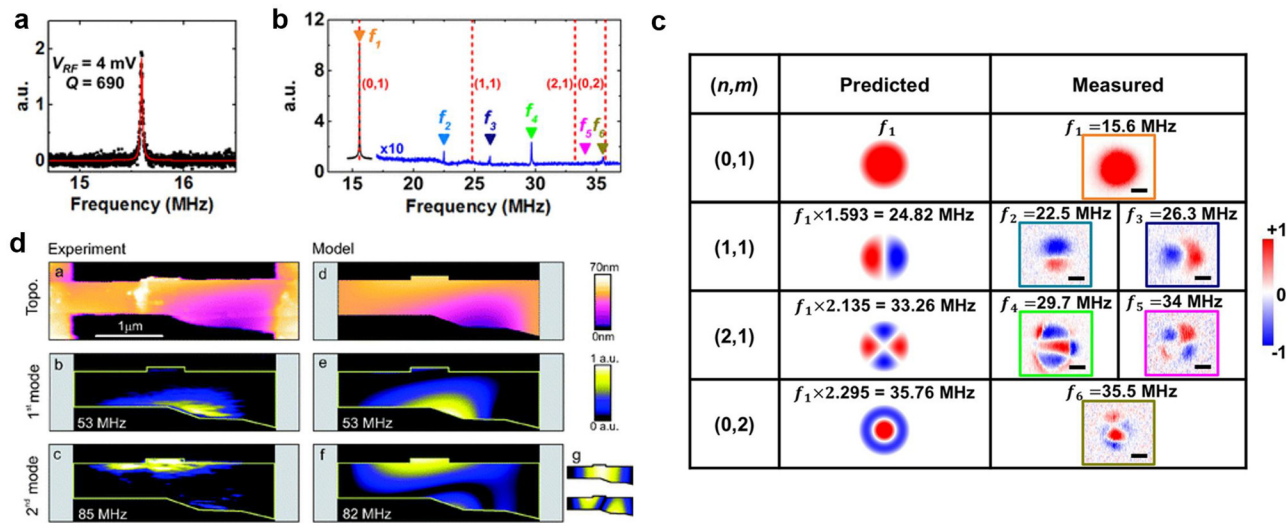


FIG. 4. Harmonics and eigenmodes in 2D NEMS. (a) Frequency spectrum near the fundamental eigenmode resonance of a graphene-MoS₂ circular drumhead resonator.⁶⁴ (b) Extended spectrum showing higher-order resonances along with the expected frequency values from continuum mechanics (dashed lines). (c) and (d): Schematic of imaging 2D NEMS mechanical motion (c) with scanning optical interferometry,⁶⁴ and (d) with tip-based scanning-force microscopy.⁷⁶ Figures (a)–(c): Reprinted with permission from Kim et al., Nano Lett. 18(11), 6686–6695 (2018). Copyright 2018 American Chemical Society. Figure (d): Reprinted with permission Garcia-Sanchez et al., Nano Lett. 8(5), 1399–1403 (2008). Copyright 2008 American Chemical Society.

A major challenge of 2D materials is achieving enough control to produce uniform resonators with predictable, reliable resonances. Even small heterogeneity in the clamping, initial stress, or flatness of the resonators can lead to drastic changes in the resonance. Because most of these changes are spatially inhomogeneous, we need spatially resolved tools to understand their impact.

2. Using eigenmodes to probe anisotropy and heterogeneity

Eigenmodes are the collective vibrations of the 2D membranes at each resonance harmonic. In general, eigenmodes may be measured by exciting the resonator at a resonance frequency, then using a localized probe to measure the dynamic position-dependent deflection of the membrane motion. The localized probe may be an atomic force microscope tip,⁷⁶ a focused laser spot rastered over the surface using scanning mirrors,^{54,64} or a motorized stage.⁹⁰ The dynamic change in tip deflection or reflected light is then measured with a lock-in amplifier. The optical measurement has the advantage of being able to be performed in vacuum but has lower spatial resolution to ~ 500 nm, so is only useful on larger devices. The scanned probe technique is difficult to integrate into a vacuum system, but has much better spatial resolution related to the tip diameter of ~ 20 nm, and is able to directly correlate the membrane morphology with the resulting eigenmode.

For example, Fig. 4(c) shows both the predicted frequencies and corresponding eigenmodes along with the actual measured frequencies and eigenmodes from the spectra shown in Fig. 4(b).⁶⁴ The eigenmodes reveal that the mode splitting rises from small anisotropic or non-uniform stress in the bimorph resonator, which breaks the degeneracy of the harmonics along the strain axis. Similarly, engineering non-symmetric rectangular or oval clamping geometries will also break the degeneracy of eigenmodes.¹¹⁸ These effects have been explored in many 2D NEMS such as hBN,⁵⁴ single-layer graphene,^{77,90} and TMDC resonators.^{118,119}

As another example, shown in Fig. 4(d), small variations in clamping, in-plane shear or irregular edges in doubly clamped few-layer graphene cause the membrane to buckle asymmetrically out-of-plane.⁷⁶ The free edges in doubly clamped beams enhance the heterogeneity, leading to isolated and unpredictable edge modes. Similar results are seen in more complex geometries, like one free edges on incomplete circular or elliptical TMDC membranes.¹¹⁸

In addition, more complex material properties can be extracted using eigenmode analysis.⁵³ For example, the anisotropic Young's moduli of black phosphorus were extracted by modeling their impact on the eigenfrequencies of the different eigenmodes of circular resonators.³⁴ Similarly, the anisotropic Young's moduli of As_2S_3 were extracted by examining the eigenfrequencies of rectangular resonators oriented along different axis of the same crystal.⁵³

3. Diameter and thickness scaling

At a single monolayer, 2D materials should have a negligible contribution from bending rigidity to the overall stiffness k_{eff} of the resonator.^{14,15} As a result, the resonator is well described as a tensioned membrane.⁹⁰ Figure 5(a) plots the measured frequency vs membrane diameter for monolayer graphene up to $25 \mu\text{m}$, showing an inverse diameter (or radius) dependence as predicted by Eq. (7). Similar

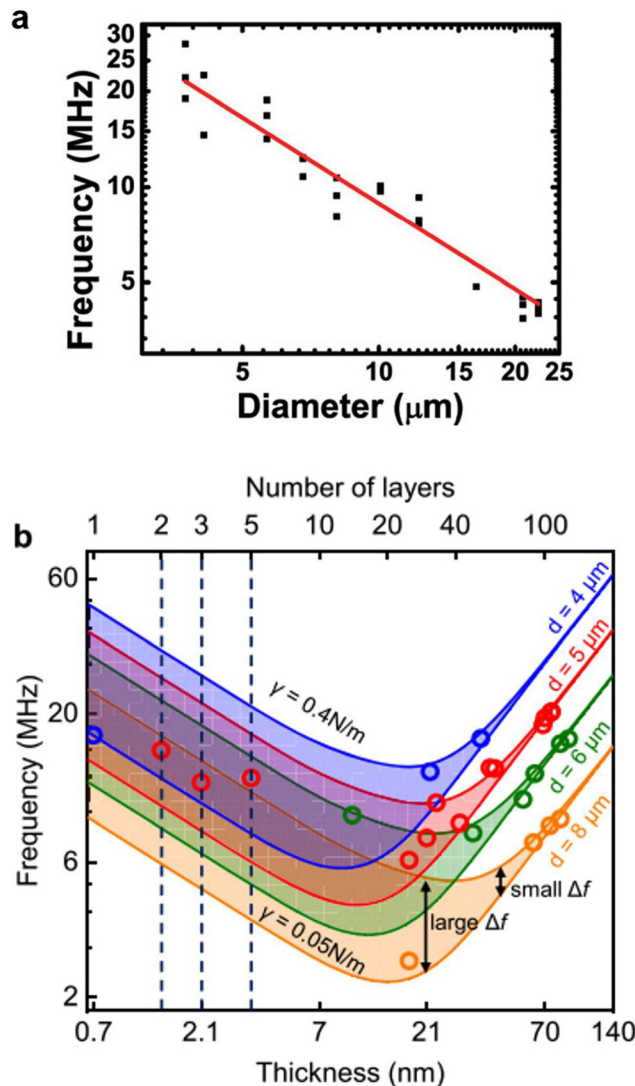


FIG. 5. Frequency scaling with 2D resonator size and thickness. (a) Frequency of monolayer graphene resonators as a function of diameter.⁹⁰ Reprinted with permission from Barton *et al.*, *Nano Lett.* **11**(3), 1232–1236 (2011). Copyright 2011 American Chemical Society. (b) Membrane to plate transition in WSe₂ resonators.¹²¹ Reprinted with permission from Zhu *et al.*, *Nano Lett.* **22**(13), 5107–5113 (2022). Copyright 2022 American Chemical Society. The plot shows the predicted frequency of the resonators for different thicknesses, initial tensions, and diameter (solid curves) along with some experimental data points (small circles). Note that the dispersion of frequencies for a fixed diameter and thickness is nicely explained by the different initial tensions of the resonators.

studies show that this scaling is valid up to $750 \mu\text{m}$ large monolayer membranes.¹²⁰

For thicker resonators, consisting of multiple layers, the faster scaling of bending rigidity ($k_{\text{bending}} \sim N^3$) compared with stress rigidity ($k_{\text{stress}} \sim N^1$) means that eventually, the bending rigidity will dominate, leading to a crossover from membrane-like behavior to plate-like behavior.

The exact crossover depends on thickness, lateral size, and initial stress.^{42,44} In practice, both the stress and bending-induced restorative forces add up to yield the effective spring constant of a resonator as $k_{\text{eff}} = k_{\text{stress}} + k_{\text{bending}}$. In terms of frequency, these two forces are combined to yield the angular resonant frequency of the resonator as¹⁸

$$\omega_1^2 = (\omega_1^{\text{membrane}})^2 + (\omega_1^{\text{plate}})^2. \quad (9)$$

Figure 5(b) shows the calculated resonant frequencies of a WSe₂ resonator using both pure membrane and plate equations along with measured frequencies of WSe₂ resonators for different thicknesses and diameters.¹²¹ Up to a certain thickness, the resonator frequencies follow the membrane model. As shown by the figure, the transition depends on the diameter and pre-stress of the resonators and occurs when $\omega_1^{\text{membrane}} \approx \omega_1^{\text{plate}}$. In the membrane regime, the scaling of the frequency is roughly $\omega_1 \sim 1/\sqrt{N}$, which follows from Eq. (7). The figure also shows that larger diameters and larger initial stress favor membrane behavior and make the transition to plate behavior occur at higher thicknesses, which can also be seen from Eqs. 7 and 8. Although this plot is specific for WSe₂, other 2D materials have been theoretically predicted or experimentally demonstrated to show the same trend, such as MoS₂,^{42,43} BP,³³ hBN,⁵⁴ and Ti₃C₂T_x.⁵⁸

B. Resonance frequency tuning

The frequency tuning of a resonator is relevant to applications in sensors¹²² and signal processing.^{96,123} The ultra-high aspect ratio of 2D membranes means that the spring constant is unusually small compared with their large Young's modulus, yet large compared with the mass. As a result of the high aspect ratio, even small applied out-of-plane forces induce displacements large compared with the material thickness, leading to large tuning of the tension and resulting resonance frequency. Figure 6(a) shows a typical tuning curve of frequency vs gate voltage for monolayer graphene.⁸⁵ The resonator tunes by >150%, whereas most MEMS typically have frequency tuning of ~1%–10%. Resonators from other 2D materials show similar tunability.⁴³

Frequency tuning in 2D resonators is determined by a competition between electrostatic tensioning and capacitive softening, where the final shape sensitively depends on clamping, thickness, aspect ratios, initial tension or out-of-plane buckling, and added mass. For example, for a flat circular membrane being pulled toward an underlying back gate, the resulting frequency tuning of the fundamental eigenmode is⁴³

$$\omega_1 = \frac{1}{R} \sqrt{\frac{4.9E\epsilon_0 + \frac{\pi\epsilon_0^2}{8(1-\nu^2)} \frac{R^2}{d^4} V_{DC}^4 - \frac{\epsilon_v \pi R^2 V_{DC}^2}{3d^2}}{0.27\pi(\rho_{ML} t_{IL} N + \rho_m t_m)}}, \quad (10)$$

where $\epsilon_v = 8.854 \times 10^{-12}$ F/m is the vacuum permittivity and $\rho_{ML} t_{IL} N$ and $\rho_m t_m$ are the planar density and thickness of all added masses on the membrane, which are assumed to be uniformly distributed on its surface. The first term on the numerator of Eq. (10) is fixed and a result of the built-in tension in the membrane. The second term rises from the electrostatically induced tension, which leads to a hardening or increase in the effective spring constant k_{eff} of a resonator, and an increase in the resonance frequency. The third term rises from capacitive softening, which is a nonlinear effect resulting from the $1/d^2$ dependence of electrostatic force with respect to the gate. The gradient in force as the membrane moves leads to an effective softening or decrease in the resonance frequency.

Figure 6(b) schematically shows how the competition between tensioning and capacitive softening affects the electrostatic frequency tuning in the resonator. Because electrostatic forces are always attractive, both tensioning and capacitive softening are symmetric with gate voltage, leading to a symmetric tuning curve around the neutral point. However, Eq. (10) states that the competition leads to quartic and quadratic V_{DC} terms with opposite signs. Depending on the relative initial stress, out-of-plane displacement, and geometric parameters of the 2D membrane, both U-shaped and W-shaped frequency tuning curves are possible. Because of the sensitivity to initial parameters, even membranes with identical dimensions can have dramatically different tuning curves. Finally, the added mass also affects the initial frequency of the membrane and the magnitude of the tuning. This added mass might come from residue or polymers from transfer or device

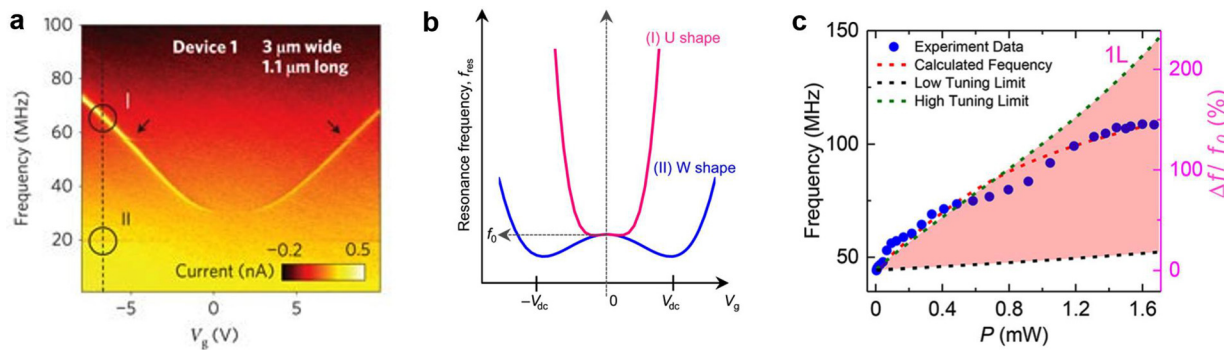


FIG. 6. Frequency tuning in 2D NEMS. (a) Frequency tuning from a doubly clamped monolayer graphene resonator with electrostatic tensile stress.⁸⁵ Reprinted with permission from Chen et al., Nat. Nanotechnol. 4(12), 861–867 (2009). Copyright 2009 Springer Nature Customer Service Center GmbH: Nature Nanotechnology. (b) Two possible tuning shapes from NEMS under electrostatic tensile stress.⁴³ Adapted with permission from Lee et al., Sci. Adv. 4(3), eaao6653 (2018). Copyright 2018 Authors, licensed under a Creative Commons Attribution Unported License. (c) Thermomechanical tuning of suspended graphene membrane.¹²⁷ Reprinted with permission from Ye et al., Nano Lett. 18(3), 1678–1685 (2018). Copyright 2018 American Chemical Society.

fabrication and is highly variable depending on fabrication methods. It is not unusual to have $\rho_m t_m \sim (1 - 10) \rho_{ML} t_{IL}$, where ρ_{ML} is the 2D monolayer planar density.⁸⁵

The model of Eq. (10) enables the extraction of membrane stress and mass from the tuning curve. In practice, the model is not very reliable because it makes strong assumptions about homogeneity in mass and stress distributions and initial flatness of the membrane that is rarely accurate and very difficult to correct for. Thus, all values should be taken as approximations.

The exact shape of the tuning curve is also very sensitive to temperature, due to changes in the initial stress of the membrane from thermal expansion of the 2D material vs the clamping substrate.^{25,85,124} Typically, at low temperatures, the initial stress ε_0 becomes higher. As can be seen in Eq. (10), the increase in initial tension suppresses the electrostatic tensioning, but does not affect the capacitive softening. Thus, most devices at lower temperature display higher initial frequency and negative frequency tuning with gate.^{85,124–126}

In addition to changing the substrate temperature, thermomechanical tuning of the stress and frequency is possible by local Joule heating or through optical absorption of intense laser light.^{79,124,129} For example, Fig. 6(c) shows the change in frequency of a graphene resonator as a function of dissipated power induced by running a current through the device. The resonator showed a thermomechanical frequency tunability of greater than 300%, which corresponds with heating the graphene up to around 1200 K.¹²⁷ However, the control of thermomechanical tuning is poor. The membrane stress-induced during thermal cycling leads to slip at the edges or inelastic changes in morphology.^{40,73} The slip leads to hysteresis in the initial stress and resulting tuning behavior, confounding detailed analysis of the thermomechanical properties of the graphene.^{40,82}

One last mechanism of tuning the stress and thus the natural frequency of a resonator is through pressure. There are two mechanisms for pressure tuning of the frequency, depending on whether the membrane is sealed or vented. First, in a sealed cavity, a pressure difference ΔP between the inside and outside of the membrane inflates or deflates the membrane like a balloon.⁷⁸ From bulge mechanics, which defines the shape of the inflated membrane, the stress is proportional to $\Delta P^{2/3}$.

Following from Eq. (7), the pressure differential leads to a frequency tuning of $\Delta(f^3) \sim \Delta P$.⁷⁸ As observed in both graphene⁷⁸ and MoS₂,¹²⁸ in the monolayer limit, it can take hours or days for the sealed chambers to equilibrate to the ambient pressure. The primary route of leaking is the van der Waals interface between the 2D material and the underlying substrate, though the quality of the material and interface strongly affects these leak rates.¹²⁹ Recently, the new class of quasi-2D complex oxide membranes has demonstrated a different self-sealing mechanism through chemical bonding with the substrate.⁶⁸ In comparison, in a leaky cavity, the space inside and outside the cavity are connected through a channel. In this case, the static pressure inside and outside the cavity are equal. However, during vibration, the dynamic gas pressure changes as the membrane compresses the gas underneath due to its rapid oscillation compared to the equilibrating time of the cavity. Called the squeeze-film effect, this leads to an effective change in the spring constant of the membrane,^{130,131} causing the resonant frequency to tune as $\Delta(f^2) \sim P$, where P is the environmental pressure. Between the two configurations, the tuning in the sealed cavity has much higher responsivity with pressure than the squeeze film pressure tuning. Over a range of 0–100 kPa, sealed cavities can have frequency tuning of $\sim 300\%$ vs $\sim 70\%$ in squeeze-film resonators.^{78,128,130,131}

C. Nonlinearity

Nonlinearity is critical to many NEMS technologies, and it dictates the dynamics of resonators at large amplitudes. In addition to technological implications, such as setting limits on the linear operation of sensors/actuators, nonlinearity is responsible for many scientifically important phenomena, such as phonon cavity effects,⁸⁰ bistability,¹³² and chaotic dynamics.^{80,133} When driven at sufficiently high amplitudes, the response of MEMS and NEMS becomes nonlinear; that is, the amplitude of motion does not scale proportionally to the driving force.¹³⁴ In general, due to scaling laws, the onset of nonlinearity occurs at smaller amplitudes for smaller systems, with 2D materials representing the ultimate limit for the thickness dimension. Similarly, 1D systems like carbon nanotubes also have small onset of nonlinearity and small or no linear dynamic range.¹³⁵ Figure 7(a)

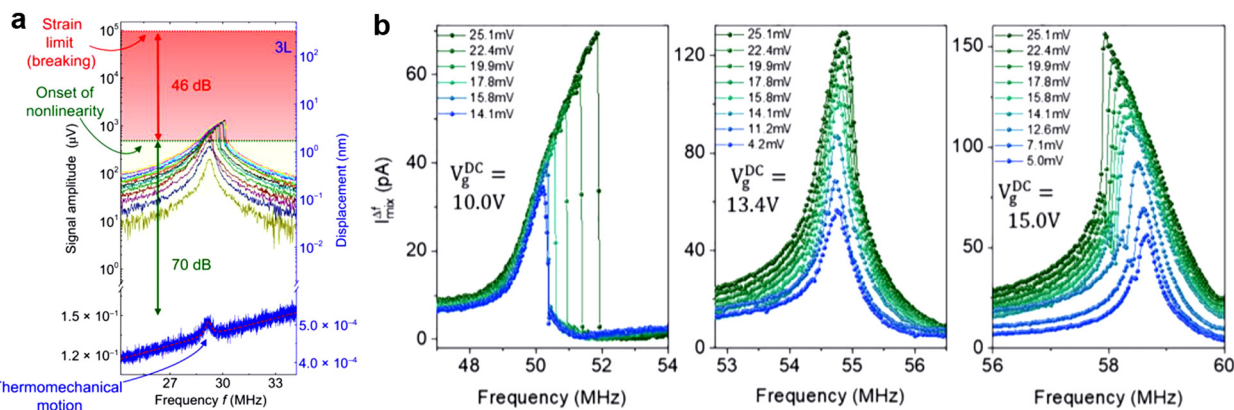


FIG. 7. Nonlinear effects in 2D resonators. (a) Frequency response of a MoS₂ resonator consisting of three layers.⁴³ The dynamic range of 70 dB is shown (green shaded area), along with the thermal amplitude (bottom curve) and nonlinear regime before breakage (red shaded area). Adapted with permission from Lee *et al.*, Sci. Adv. 4(3), eaao6653 (2018). Copyright 2018 Authors, licensed under a Creative Commons Attribution Unported License. (b) Frequency response curves for a bilayer MoS₂ resonator at three gate voltages, showing tuning of the nonlinear behavior.¹⁴⁸ Reprinted with permission from Samanta *et al.*, Appl. Phys. Lett. 113(11), 113101 (2018).¹⁴⁸ Copyright 2018 AIP Publishing LLC.

shows an example of the drive-dependent mechanical resonance of a three-layer MoS₂ drum head membrane. At moderate amplitudes, shown in green, the resonator operates in the linear regime. At low amplitudes of motion, shown in blue, the high aspect ratio of 2D NEMS leads to relatively large dynamic thermal fluctuations of the membrane, also referred to as thermomechanical or Brownian motion, which sets the smallest measurable signals. At high amplitudes of motion, shown in red, the low spring constant and high Young modulus lead to large geometric nonlinearities. Generally, the strain on 2D membranes is on the scale of 0.01%, while the onset of material elastic nonlinearity due to bond stretching occurs around 5%, so material nonlinearities do not play a role in experiments.¹³⁶

1. Dynamic thermal fluctuations and amplitude calibration

The smallest motion of 2D NEMS is set by the dynamic thermal fluctuations of the out-of-plane eigenmodes due to coupling to the phonon vibrations of the atoms in the lattice and from the substrate. The dynamic thermal fluctuations of a resonator in any microsystem are well-defined based on the equipartition theorem, and there are several expressions useful for understanding the behavior of 2D NEMS. First, the equipartition theorem states that the average energy in each eigenmode is $E = \frac{1}{2}k_B T$, where $k_B = 1.38065 \times 10^{-23}$ JK⁻¹ is the Boltzmann constant and T is the temperature. Simultaneously, the energy of an eigenmode is also given by the elastic potential energy as $E = \frac{1}{2}k_{\text{eff}} z_{th}^2$, where z_{th} is the integrated root mean square (RMS) amplitude of vibration over all frequencies. Relating these two energies gives the RMS amplitude of a resonator at finite temperature

$$z_{th} = \sqrt{k_B T / k_{\text{eff}}} \quad (11)$$

While the frequencies of these vibrations mostly match with the resonant frequency of the eigenmode, there is a finite dispersion due to the presence of dissipation. This is quantified by the thermal noise power $S_{zz}(\omega)$ vs frequency of a resonator for different eigenmode frequencies ω_i . It is given by Lee *et al.*⁴³

$$S_{zz}(\omega) = \frac{4k_B T \omega_i}{m_{\text{eff}} Q [(\omega^2 - \omega_i^2)^2 + (\omega \omega_i / Q)^2]} \quad (12)$$

Note that z_{th} can be calculated by integrating $S_{zz}(\omega)$ over ω and taking the square root. Most relevant to measurement, however, is the peak noise power density, occurring at the resonance frequency of each eigenmode. It is given by

$$S_{zz}(\omega_i) = \frac{4Qk_B T}{m_{\text{eff}} \omega_i^3} = \frac{4Qk_B T}{\omega_i k_{\text{eff}}} = \frac{4Q}{\omega_i} z_{th}^2 \quad (13)$$

Because of their atomic thicknesses, 2D resonators have very low effective masses and spring constants, which makes the amplitude of the dynamic thermal fluctuations very large compared to other M/NEMS.⁴³ Typically, the value of z_{th} for a typical graphene membrane is on the scale of 1–5 Å at room temperature. While this amplitude sounds small, bear in mind that monolayer graphene has “thickness” of 3.4 Å (or zero depending on who you ask), so that the dynamic thermal fluctuations are on the scale of the size of the material. Meanwhile, the dynamic thermal fluctuations at resonance from Eq. (13) are much smaller $\sqrt{(S_{zz}(\omega_i))} \sim 0.1\text{--}1 \text{ pm/Hz}^{1/2}$, with the exact

amplitude depending on the bandwidth of the measurement.⁴³ Using a BW comparable to the FWHM of a resonance recovers an amplitude consistent with Eq. (11).

Beyond their impact on thermomechanical material properties, the thermal fluctuations have a practical utility in amplitude calibration. A desirable performance metric in any MEMS is the amplitude of motion on an absolute scale. There are two common methods to infer the change in measured signal as the moving surface vibrates, and the second is by measuring the resonator response with respect to well-defined thermal motion. There are also more advanced techniques such as modifying the Fabry-Pérot gap⁸¹ or leveraging nonlinearities of the optical transduction.¹³⁷ These techniques require displacement of the membrane with respect to a reflecting surface comparable to the wavelength of the sensing laser, so are restricted to either specialized setups with moveable mirrors or very large devices with correspondingly large amplitude of vibration.

Since the thermal amplitude of motion is always present in the system and based on measurable properties, it makes an excellent reference. Thus, many papers use thermal motion as a method of calibration that provides a scale factor relating measured signals to an absolute amplitude, and the exact procedure of different measurement techniques can usually be found in supporting methods.^{30,43,64,138} Importantly, the calibration is only valid for the specific operating conditions. Any change in membrane deflection due to thermal or electrostatic force requires re-calibration.¹³⁹

2. Linear dynamic range in 2D NEMS

Understanding the linear range of operation is critical for any application of M/NEMS. The linear dynamic range (LDR) defines the range of amplitudes in which the device’s response is linear, with thermal fluctuations setting the lower limit and nonlinear dynamics setting the upper limit. Above the LDR, the range of amplitudes before failure defines the nonlinear dynamic range (NDR). Thus, the total operable range of a resonator, with amplitudes between thermomechanical motion and mechanical failure, is the sum LDR + NDR.

Given in dB, the LDR is calculated as¹³⁵

$$\text{LDR} = 20 \log_{10} \left(\frac{0.745 a_c}{\sqrt{2S_{zz}(\omega_i) \Delta f}} \right), \quad (14)$$

where a_c is the amplitude on the onset of bistability and Δf is the measurement bandwidth. The amplitude 0.745 a_c is the 1 dB compression point of the resonant response, which corresponds to the amplitude of motion that is 1 dB below the one expected from linear scaling. The LDR is graphically displayed in Fig. 7(a) as the vertical size of the regions highlighted in green (70 dB).⁴³

The dynamic range increases with larger diameter, strain, and number of layers.¹⁴⁰ So far, for MoS₂, the highest reported linear dynamic range is around 70 dB and nonlinear dynamic range is around 40 dB, for a total dynamic range of 110 dB.⁴³ However, most resonators built from 2D materials have lower dynamic ranges, in the range of 40–60 dB.^{30,64,85,90,141} Some variability in LDR is due to differences in the mechanics of the 2D resonator; however, much of the variability is actually due to external factors like the responsivity of the transduction mechanism and bandwidth used for measurement.

The higher numbers are the more physically meaningful, as they come from experiments that were intentionally optimizing the signal-to-noise.

In comparison, MEMS and NEMS resonators made from silicon- and piezoelectric-based materials have commonly shown dynamic ranges around 100 dB or more.^{142–146} That most 2D resonators have lower LDR than other MEMS and NEMS devices with larger dimensions is consistent with the larger thermomechanical noise amplitude for devices with reduced dimensions.¹⁴⁷

Optimizing the dynamic range of 2D resonators is critical to many applications and making them competitive with more traditional MEMS. This requires understanding the physical origins and scaling laws defining nonlinearity, damping, and thermomechanical motion, which we will address in Secs. IV C 3–IV D 3.

3. Geometric nonlinearity in 2D NEMS

The two geometric nonlinearities dominating the behavior of 2D NEMS are common to many MEMS systems: nonlinearities from amplitude-dependent membrane stress and capacitive softening. The lumped element model allows treatment of nonlinearities as a Taylor expansion of the position-dependent force and spring constant on the resonator around a static equilibrium position as

$$F_{\text{total}}(z) = -k_1 z - k_2 z^2 - k_3 z^3 + \dots, \quad (15)$$

where z is the deflection from the equilibrium position, and k_1 , k_2 , and k_3 are the linear, quadratic, and cubic spring constants. Progressively, higher-order terms become important at large enough deflection. However, for the majority of applications explored in 2D NEMS, the first three terms are sufficient to describe the observed behavior. Thus, we do not consider the higher-order terms k_n with $n > 4$ in the following analysis. The nonlinear force terms lead to an effective frequency of the resonator vs amplitude, called the backbone curve, given by Nayfeh and Mook¹⁴⁹

$$\omega'_i = \omega_i(1 + \kappa z_0^2), \quad (16)$$

where ω_i and ω'_i are the linear- and amplitude-dependent resonant frequency, respectively, and z_0 is the amplitude of motion and

$$\kappa = \frac{3k_3}{8k_1} - \frac{5k_2^2}{12k_1^2}. \quad (17)$$

The exact values may be extracted from Galerkin analysis^{148,149} and are highly sensitive to membrane geometry, static equilibrium shape, and dynamic eigenmode shape. For example, the expressions for the stress forces due to deflection of an initially flat circular membrane operating at the fundamental resonance eigenmode under initial in-plane stress σ_0 are

$$F_{\text{stress}}(z) = -4\pi\sigma_0 z - \frac{8\pi YN}{3R^2(1-\nu)} z^3 + \dots. \quad (18)$$

We can write a similar expression for the nonlinear force rising from electrostatic capacitive attraction

$$F_{\text{electrostatic}}(z) = -\frac{1}{2}\varepsilon_0\pi R^2 V^2 \left(\frac{1}{d^2} + \frac{2z}{d^3} + \frac{3z^2}{d^4} + \frac{4z^3}{d^5} + \dots \right). \quad (19)$$

Here, we used the parallel-plate capacitor approximation for a flat circular drumhead. While the exact values would depend on the shape of the eigenmode, the approximate values are on the correct order of magnitude and capture the essential physics. These equations show that for a flat membrane, the stress nonlinearities only have odd terms because the force must be symmetric, e.g., $k_2 = 0$. Typical values are $k_1 \sim 0.1 - 1 \text{ N/m}$ and $k_3 \sim 10^{14} - 10^{15} \text{ N/m}^3$.^{27,140} If, however, the symmetry is broken, either from pull down of the membrane with electrostatic gates, or from initial buckling out-of-plane, then it becomes necessary to include even terms as well. In contrast, the capacitive nonlinearities always have both even and odd terms due to the broken symmetry. In the simplest case, the lowest stress nonlinearity is cubic and positive, and the lowest capacitive nonlinearity is quadratic. As a result, according to Eq. (17), the two terms compete with each other with capacitive nonlinearity leading to a negative frequency shift with amplitude, called softening, while the stress nonlinearity leading to a positive frequency shift with amplitude, called hardening. Figure 7(b) shows the change in the nonlinear resonance vs drive of the same resonator at different gate bias and shows a gate-dependent transition from nonlinear softening to hardening behavior. Between, there is a narrow range of gate voltages at which the two nonlinearities cancel, leading to a larger linear regime before higher-order nonlinearities emerge. The strong dependence of nonlinearity and dynamic range on applied strain and gate is potentially useful in reconfigurable devices whose response may be switched on and off from the nonlinear regime by the electrostatic gate voltage.¹⁴⁸

4. Bistability and switching

Just as with many nonlinear mechanical resonators, at high drive, the nonlinearity in 2D resonators leads to a bistability, characteristic of a Duffing oscillator.^{137,150} Figure 8(a) shows the nonlinear response of a graphene resonator driven at high amplitude.¹³² The resonator shows a hysteresis of 70 kHz when it is swept upward vs downward in frequency. The hysteresis is a result of switching from a high-amplitude state to a low-amplitude state if the frequency is swept upward, and vice versa if swept downward. Figure 8(b) shows the amplitude vs time response of the same resonator driven at a fixed frequency inside the hysteresis loop, as shown in Fig. 8(a). The amplitude stochastically switches between the upper and lower solutions due to thermal fluctuations after a noise signal is applied to the gate in conjunction with the drive that enhances the effective temperature. The switching frequency reaches rates up to 4.1 kHz, a factor of 100 faster than state-of-the-art MEMS.¹⁵¹ This high switching rate has applications for graphene resonators as ultrasensitive microphones¹³² and chaotic signal generators.¹⁵²

D. Energy dissipation

For all MEMS, energy dissipation or damping plays an important role in determining the fundamental limits on performance. For instance, low dissipation is ideal for efficient transduction of classical and quantum signals,^{153–157} while high dissipation broadens the frequency bandwidth of operation. The ability to dynamically tune the dissipation or quality factor of a resonator is advantageous in applications that benefit from having a variable bandwidth, such as reconfigurable RF filters, AFM imaging,¹⁵⁸ and tunable inertial sensors.¹⁵⁹

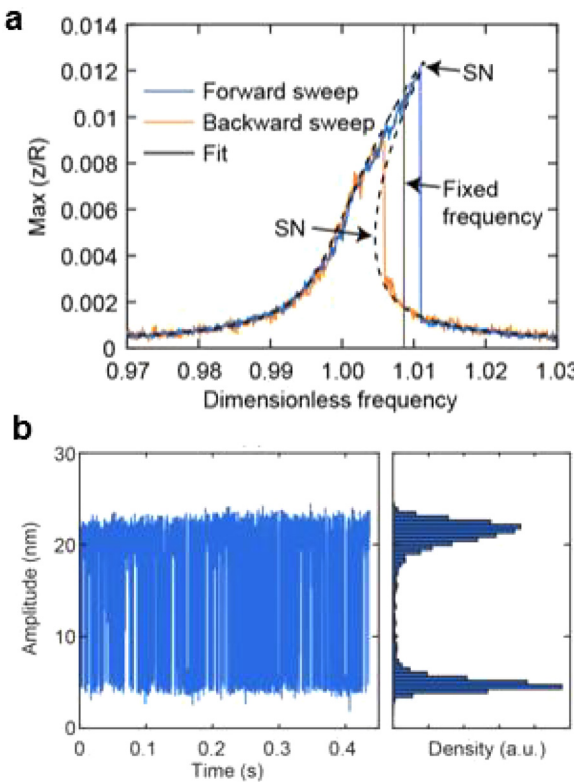


FIG. 8. (a) Duffing response of a monolayer graphene resonator showing hysteresis in forward and backward sweeps in frequency and (b) amplitude vs time response of a nonlinearly driven graphene resonator at the fixed frequency shown in (a) within the hysteresis loop. The resonator shows stochastic switching between the upper and lower solutions with a frequency of 4 kHz.¹³² Reprinted with permission from Dolleman *et al.*, Nano Lett. **19**(2), 1282–1288 (2019).¹³² Copyright 2019 American Chemical Society.

Dissipation is mathematically described by the effective damping coefficient b_{eff} in the lumped element equation of motion, Eq. (5). In any M/NEMS system, there are many potential linear and nonlinear dissipation mechanisms, which we will detail Secs. IV D 1–IV D 3. Linear dissipation mechanisms add, leading to a total effective damping b_{eff} or similarly a normalized dissipation rate Q_{eff} that is the sum of the individual dissipation contribution from each mechanism b_j ,

$$b_{\text{eff}} = \sum_j b_j. \quad (20)$$

From the equation, it is clear that the largest dissipation mechanism dominates. Yet, each mechanism can have different physical origin and scaling as a function of geometric, environmental, and experimental parameters. As a result, isolating and identifying the dominant mechanism is quite challenging and requires extensive parametric measurements to explore the scaling of dissipation, nanoscale simulation, and developing new theories. Dissipation is typically measured in the frequency domain from the full-width-half max (FWHM) of the resonance peak or in the time domain by the ringdown in amplitude vs time after drive is removed. As a result, dissipation is most often represented through the dimensionless quality factor Q , or

the peak width/dissipation rate $\gamma = b_{\text{eff}}/m_{\text{eff}}$. The quality factor and other measures of dissipation are related in the following ways:

$$Q = \frac{2\pi E}{\Delta E} = \frac{\omega_i}{\gamma} = \omega_i \tau = \frac{m_{\text{eff}} \omega_i}{b_{\text{eff}}}, \quad (21)$$

where E and ΔE are, respectively, the stored energy and dissipated energy in one cycle, and τ is the decay time. Generally, a lower-quality factor corresponds with higher dissipation, wider resonance, and faster ringdown.

An unusual feature of graphene and 2D resonators, with profound implications on their applicability, is that they have a surprisingly low-quality factor in the range of $Q \sim 10 - 500$ at room temperature.^{42,43,50,54,56} In contrast, at room temperature, NEMS built from silicon show quality factors in the scale of thousands² or even 10^6 in high-stress SiN_x resonators.^{160,161} Even more interesting, as discussed further later, Q in 2D resonators shows strong tuning with temperature, and much higher-quality factors at low temperature, $Q > 10^5$ in graphene, and $Q > 10^4$ in TMDCs,^{50,62,126} showing that if we can fully understand and engineer the mechanisms, there is room for drastic improvement of the quality factor and thus the utility of 2D NEMS.

In this section, we will first summarize the measured scaling of quality factor as a function of experimentally relevant parameters and then discuss the theories on the dominant dissipation mechanisms.

1. Quality factor and dissipation in 2D resonators

Here, we will discuss the experimental measurements and simulations of quality factor in 2D mono and few-layer resonators vs environmental and design parameters like pressure, lateral size, eigenmode, temperature, and strain, then discuss potential mechanisms in Sec. IV D 2. We will focus our discussion mostly on graphene, but other 2D materials show similar trends of Q . For example, under similar experimental and design conditions, TMDCs show slightly higher Q at room temperature^{42,43,50} and lower Q at low temperature,^{50,62,126} though variations between studies are large. Simulations attribute the higher-quality factor in TMDCs vs graphene to a larger phonon bandgap in the former, which reduces scattering of the eigenmodes into other phonon modes.¹⁶² However, the exact models describing the differences have yet to be established, and the differences between 2D materials are minor compared with the overall behavior of all 2D materials compared with conventional thin films.

First, as with any MEMS, the presence of gas adds strong dissipation. In 2D NEMS, this dissipation typically yields quality factors of $Q < 10$ at atmospheric pressure compared with $Q \sim 50-500$ in vacuum ($P < 10^{-6}$ Torr).^{78,128–131} The scaling of Q vs pressure depends on whether the resonator forms a sealed cavity or is vented to the environment.¹²⁸ For example, fully clamped and vented resonators show scaling $Q \sim 1/P$ for pressures below 100 mbar,^{130,131} consistent with the predicted dissipation due to the squeeze-film effect, which results from coupling membrane deflection with gas compression. For higher pressures, gas flows into and out of the cavity become more significant and the assumption of pure gas compression breaks, leading to a more complex pressure dependency. In contrast, as discussed earlier in Sec. IV B, fully clamped and sealed membranes allow gas to get trapped in the cavity, leading to more complex interplay between inflation-induced tensioning and damping. At high (near atmospheric) pressure, Q scales as ω_i/P , where P is the pressure outside the cavity.¹²⁸ At

low pressure (below ~ 50 Torr), the damping from the internal gas pressure dominates and the quality factor saturates. Additionally, if there is slow leakage into or out of the sealed membranes, it can be difficult to predict hysteresis in the damping and resonance frequency.^{78,128}

Figure 9(a) plots the quality factor Q vs membrane diameter from 2 to $30 \mu\text{m}$ in monolayer graphene resonators at room temperature.⁹⁰ The quality factor increased with increasing diameter, following $Q \sim D^{1.1}$ and reaching $Q \sim 2400$ for the larger membranes. Of course, the frequency also scaled inversely with membrane size $\omega \sim D^{-0.9}$. This systematic dependence of Q on diameter only occurs in fully clamped membranes. In contrast, in doubly clamped resonators, Q is lower and more unpredictable, due to the presence of dissipative modes originating from the free edges.^{25,76,165} Deconvolving the contribution to quality factor from frequency required comparing the

dissipation from multiple eigenmodes with different frequencies for each resonator at each diameter. This comparison showed that the quality factor did not scale directly with frequency, just membrane diameter.

The trend for quality factor vs thickness t is less clear.⁴² While some thicker resonators show higher-quality factors, the variation at a particular thickness is at the same magnitude as any trend with thickness, likely due to sample variations in stress and morphology.⁴² An important factor that determines the dissipation in multilayer resonators is the van der Waals interactions between layers.^{26,163} In particular, due to the low energy threshold for sliding 2D materials against each other,^{164,166–168} interlayer friction should be an important extra mechanism of dissipation starting from bilayer to few-layer resonators. Figure 9(b) is a plot of the simulated quality factor in a bilayer resonator as a function of the interlayer friction stress σ_f starting from a

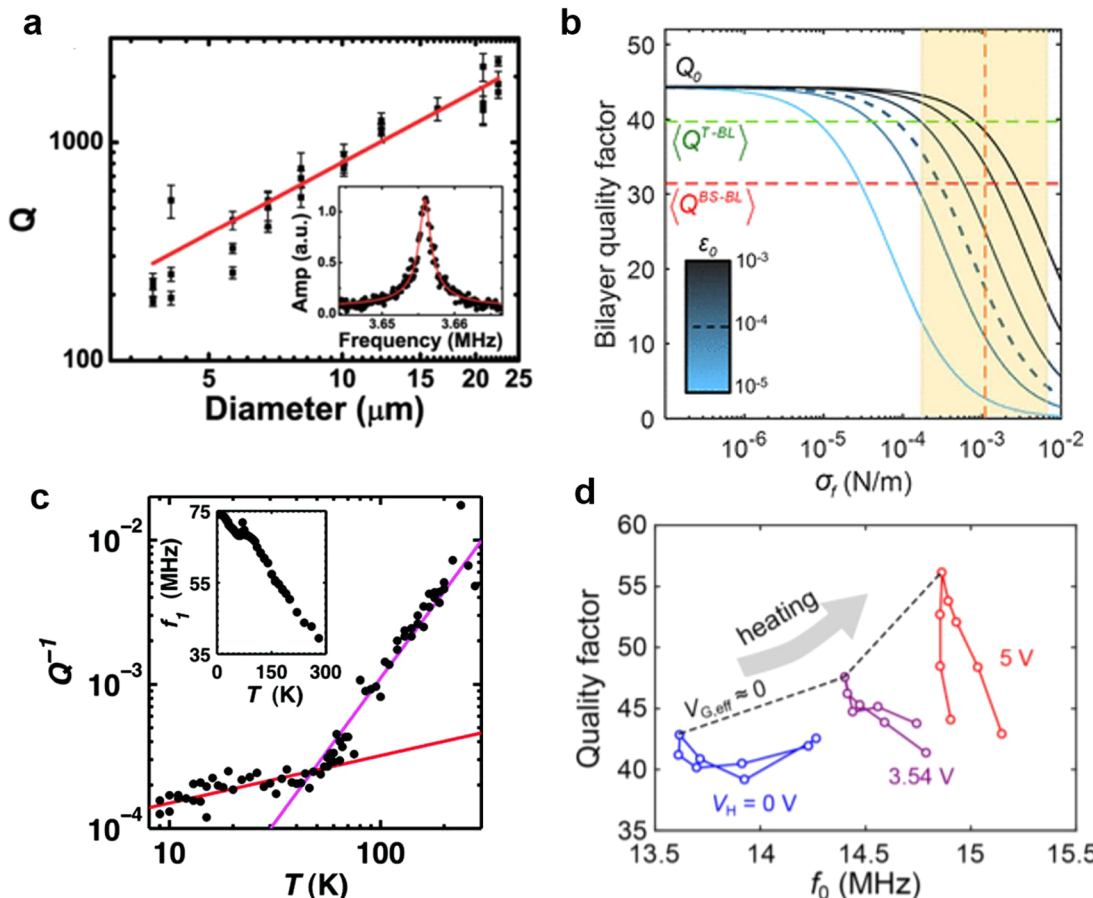


FIG. 9. Parametric dependence of the quality factor Q in 2D resonators. (a) Plot of quality factor vs membrane diameter for monolayer CVD grown graphene membranes.⁹⁰ Reprinted with permission from Barton et al., Nano Lett. **11**(3), 1232–1236 (2011). Copyright 2011 American Chemical Society. (b) Plot of simulated quality factor vs interlayer friction σ_f for a bilayer resonator under different pre-strains.¹⁶³ Red and green dashed lines correspond to measured average quality factors of Bernal-stacked and twisted bilayer resonators. The yellow panel shows the range of interlayer friction values estimated from static friction measurements, with the orange dashed line being the average of these measurements.¹⁶⁴ To help interpretation, the dashed blue line corresponds to pre-strain $\varepsilon_0 = 10^{-4}$, which is a typical pre-strain in the resonators.²⁶ Reprinted with permission from Kim et al., Nano Lett. **20**(2), 1201–1207 (2020). Copyright 2021 American Chemical Society. (c) Temperature dependence of monolayer graphene resonators.²⁵ Reprinted with permission from van der Zande et al., Nano Lett. **10**(12), 4869–4873 (2010).²⁶ Copyright 2010 American Chemical Society. (d) Quality factor of a monolayer graphene resonator clamped to an expansion ring. The plot shows Q for three different in-plane strains (set by V_H) and multiple gate voltages ($V_{G,\text{eff}}$).⁸⁶ Reprinted with permission from Davidovikj et al., Nano Lett. **18**(5), 2852–2858 (2018). Copyright 2018 American Chemical Society.

frictionless case Q_0 .¹⁶³ The model is based on a structural dissipation model commonly used in macroscopic systems.¹⁶⁹ As denoted by the inset color bar, the plot compares the decay in quality factor for different pre-strains, from $\varepsilon_0 = 10^{-5}$ to $\varepsilon_0 = 10^{-3}$. For comparison, the figure shows the average quality factor of many Bernal-stacked ($\langle Q^{BS-BL} \rangle$) and twisted ($\langle Q^{T-BL} \rangle$) bilayer graphene resonators measured on a single chip. The yellow panel is an estimation of the interlayer friction from sliding measurements of a graphite-graphite interface,¹⁶⁴ which indicates that σ_f should be in the range of 10^{-4} – 10^{-3} N/m. These frictions are enough to significantly decrease the quality factor compared with the frictionless case and can explain the reported trend of higher-quality factor in monolayer vs bilayer resonators,¹⁶³ confirming predictions from previous MD simulations.¹⁷⁰ The higher dissipation in bilayers also agrees with the lower on-set of nonlinearity in monolayer vs bilayer resonators predicted by simulations.¹⁷¹ For devices with a larger number of layers, other dissipation mechanisms besides interlayer friction may be more relevant in determining Q . In thicker devices, the mechanics transition from membrane to plate behavior and the material approaches aspect ratios more common to typical NEMS. As a result, other dissipation mechanisms which scale with thickness become more important, such as thermoelastic dissipation and dissipation from material defects.^{172,173} To probe the influence of interfacial dissipation in multilayer resonators, a similar statistical comparison between the dissipation of resonators containing different pristine interfaces (commensurate or incommensurate) and different number of layers would be necessary.

Most dramatically, dissipation in 2D resonators depends strongly on temperature, with the quality factor rising from $Q \sim 100$ at room temperature to $Q > 10^4$ at low temperature. Figure 9(c) shows the temperature dependence of the inverse quality factor in doubly clamped monolayer graphene resonators.²⁵ The exact trend depends strongly on the clamping. In doubly clamped resonators, for temperatures above $T \approx 100$ K, Q^{-1} scales roughly as $Q^{-1} \sim T^2$, whereas for lower temperatures, $Q^{-1} \sim T^{0.3} - T^{0.5}$.^{25,85} In contrast, fully clamped resonators show similar ranges, but with scaling $Q^{-1} \sim T^{-1}$, and no crossover.^{174,175} The more complex temperature scaling in doubly clamped membranes is a result of losses from edge modes at low temperature^{176,177} and changes in strain from thermal expansion on electrodes at higher temperature.¹⁷⁴ For the fully clamped membrane, the $Q^{-1} \sim T^{-1}$ scaling matches simulations based on thermal fluctuations, discussed later.¹⁷⁰ While the vast majority of studies focus on graphene resonators, other 2D resonators made from WSe₂ or graphene/NbSe₂ heterostructures show similar trends.^{50,62}

In comparison, carbon nanotube resonators, which are intrinsically doubly clamped and 1D but structurally similar to graphene, show very similar changeover in scaling laws as the doubly clamped graphene resonators.^{178,179} Meanwhile, conventional thin-film resonators show scaling $Q \sim T^{0.2-0.3}$ through all temperatures, meaning that the quality factor at low temperature is only a factor of 2–3 better than at room temperature. In contrast, in graphene and carbon nanotubes (CNTs) at sub-kelvin temperatures, the dissipation becomes very low, leading to some truly impressive quality factors given the size. Monolayer graphene resonators coupled to superconducting cavities achieved quality factors $Q > 10^5$ ^{126,138} while multilayer graphene resonators achieved $Q \sim 10^6$ at $T = 15$ mK.¹⁸⁰ These high-quality factors at low-temperature mean graphene and carbon nanotube resonators are good candidates for high-quality qubits or quantum information storage.

According to simulations, quality factor should strongly tune with strain, due to the increase in stored energy and higher frequency.^{170,181} This hypothesis has motivated several studies on strain engineering in 2D resonators through electrostatic gating, like the electrostatic frequency tuning studies discussed in Sec. IVD 1,^{43,182} heat shrinking of patterned SU8 clamps or thermal heaters to apply in-plane strain onto suspended graphene membranes.^{86,97,183} In practice, the experimental results are mixed because of the difficulty of unraveling strain from nonlinear effect, strain-induced slip, or morphology changes. For example, as shown in Fig. 7(b), the changeover in nonlinear response as a function of gate voltage makes it difficult to unravel the interaction of strain and nonlinear effects on the quality factor. As another example, using heat shrinking of patterned SU8 clamps to apply in-plane uniaxial strain onto doubly clamped graphene resonators showed an increase in quality factors up to $Q \sim 7000$ at room temperature.¹⁸³ However, as shown in Fig. 9(d), a more recent study explored the dependence of quality factor using thermally heated electrodes⁸⁶ to apply an in plane biaxial strain on a 2D membrane fully clamped by and SU8 expansion ring and an electrostatic gate. Each color corresponds with applying a different heating voltage to change the tension and morphology, while the data points within each color show the tuning of Q and frequency with gate voltage at that tension. The data show that different morphologies/strains lead to different tuning of both Q and frequency with gate, but the values are not significantly different from unstrained graphene resonators, and there are no clear trends with strain. The difference between these two studies might be due to the relative strains applied, or because of morphology and eigenmode changes in the double clamped resonators, as discussed in Fig. 4. In general, while the promise of strain engineering to modify dissipation is high, it will only be realized with creative new approaches to ensure large biaxial strain is uniformly applied to flat membranes.

2. Comparing mechanisms of dissipation in 2D NEMS

Unraveling the mechanisms underlying dissipation in NEMS in general is very challenging both experimentally and theoretically, yet very important, and still an active area of research. First, there are many competing mechanisms, and it is difficult to know which one should dominate without simply comparing every mechanism. Second, while it is possible to write down equations representing any individual mechanism, and infer scaling laws, actually calculating a value requires making assumptions on factors which are not provided by experiments—such as process-induced parameters like distribution of added mass, heterogeneity of clamping, heterogeneous stress and morphology, or density of defects. For a theory to be valid, it should predict both the scaling behavior and order of magnitude of dissipation. In general, conventional intrinsic and extrinsic dissipation mechanisms do not fully explain the measured behavior. Here, we will briefly compare commonly considered mechanisms of dissipation in NEMS and rule some of them out either based on experimental evidence or because the theory predicts negligible contributions for realistic assumptions. In Sec. IVD 3, we will discuss the most promising current theory.

In general, dissipation is classified into either extrinsic or intrinsic mechanisms.^{2,184} First, we will consider extrinsic dissipation mechanisms, which result from coupling the resonator to its environment or

from the transduction mechanism/experimental conditions. Examples include viscous gas damping, clamping/attachment losses, Ohmic heating, optomechanical coupling, or coupling with charges or two-level systems in the dielectric substrate.¹⁷² The strength of these different mechanisms varies by orders of magnitude. For example, viscous dissipation dominates for a resonator operating at atmospheric pressure, but is negligible at the pressures used in most studies (typically $P \sim 10^{-6}$ Torr).⁷⁸ Experimentally, Ohmic losses or optomechanical effects can be achieved under very large drive,^{79,127} but values are typically chosen to make them not dominant, when studying intrinsic behavior. At low drive, comparisons across studies show both electrically and optically actuated resonators have similar ranges of Q at both room and low temperature.^{25,42,43,50,79,91,163} Experiments, like those shown in Fig. 9(a), show the quality factor scales with membrane diameter, suggesting that clamping losses might be a dominant mechanism.⁹⁰ However, equations predicting the clamping or attachment losses predict at least three orders of magnitude higher-quality factors than those observed in experiment,¹⁷² suggesting that the mechanism might have the same scaling as clamping losses, but a different physical origin. Finally, losses from other mechanisms such as coupling of electrons in the 2D membrane to two-level systems or adhesion to the substrate are predicted to provide negligible dissipation.¹⁷²

Intrinsic mechanisms are more difficult to directly control and are still an active area of research in the broader MEMS/NEMS community. Intrinsic dissipation mechanisms result from material properties and may be further broken down into dissipation in ideal materials, such as conversion of energy into phonons through the thermoelastic or Akhiezer dissipation, or dissipation in imperfect materials due to coupling to defects within the material or surface states.² One of the original motivations for pushing to study 2D materials as NEMS was that their material properties are ideal for minimizing intrinsic mechanisms of dissipation—2D membranes are single crystal with no defects (except for CVD grown materials), and the van der Waals surface has no dangling bonds, which should minimize surface dissipation and can dominate dissipation in ultrathin amorphous or 3D crystalline resonators.^{2,185} Moreover, thermoelastic, Akhiezer, and clamping dissipation are all predicted to scale with thickness, so going to a monolayer should minimize those mechanisms.^{172,173} The actual measured values point to a more interesting and complex solution. At low temperature, 2D NEMS have a high-quality factor compared with silicon MEMS. However, there is a strong temperature dependence $Q^{-1} \sim T^{-1}$ for fully clamped resonators), and at room temperatures 2D NEMS end up with a lower-quality factor compared with silicon NEMS. While some intrinsic mechanisms like thermoelastic dissipation theories predict the $Q^{-1} \sim T^{-1}$ temperature dependence observed in 2D resonators, they also predict that 2D resonators should have four orders of magnitude higher-quality factors than conventional silicon MEMS even at room temperature, contrary to what is observed.¹⁷² As discussed in Sec. IV D, this disagreement has motivated a search for a new theory to describe dissipation in 2D NEMS.

3. FPUT dissipation from nonlinear thermal fluctuations

Over the last decade, theoretical and experimental studies suggest a new mechanism unique to 1D and 2D materials, though a complete theory is still in development. In ultra-high aspect ratio resonators, like carbon nanotube strings and 2D membranes, nonlinear thermal

fluctuations induce significant dissipation at room temperature.¹⁸⁶ This mechanism has roots in the dynamics of the Fermi–Pasta–Ulam–Tsingou problem, where the nonlinear coupling between modes thermalizes an otherwise dissipationless linear system.^{112,181}

To understand the origin of the Fermi–Pasta–Ulam–Tsingou thermalization in 2D NEMS, let us first consider the dissipation at low temperature. The high-quality factor of 2D resonators at low temperature allows direct measurement of the ringdown of the resonator in the time domain after the removal of drive, which is a more reliable measure of dissipation than the more common measurement of FWHM. This is because, in many cases, FWHM measurements tend to be averaged over a long period, and thus may be artificially spread due to fluctuations in the natural frequency.¹¹² Figure 10(a) shows the ringdown of a graphene drum coupled to a superconducting local gate at three different gate voltages (offset by a factor of 4 from each other).¹⁸⁰ In each measurement, there are two separate rates of ringdown, a fast one at high amplitude and a slower one after settling to a lower amplitude. The onset of higher, nonlinear loss occurs at very small amplitudes of ~ 100 pm. The slower decay time at low amplitude corresponds with impressively high-quality factors of $Q > 10^6$. The higher decay rate for larger amplitude is a result of nonlinear coupling of the driven fundamental eigenmode to undriven higher harmonics, which leads to an additional channel of loss for the resonator.

To further elucidate this mechanism, Fig. 10(b) is a molecular dynamics simulation of the time evolution of a graphene membrane, initially excited at the fundamental eigenmode and left to relax. The plot shows the spectral density at different time steps, and the color scale shows the area under the curve for the fundamental eigenmode. The inset shows the time evolution of the energy for the first 10 eigenmodes, showing the transfer of energy or phonons from the initially driven eigenmode to the higher modes due to nonlinear mode coupling.¹⁸¹ These MD simulations predict that the nonlinear thermal fluctuations lead to an effective enhanced dissipation out of any one eigenmode scaling linearly with temperature, as observed in the experimental measurements on fully clamped membranes. Similarly, multi-scale mechanics models demonstrate that nonlinear couplings between eigenmodes make a crucial source of dissipation in graphene membranes.^{187–189}

Intuitively, the low onset amplitude for nonlinear dissipation from mode coupling at low temperature explains the much lower-quality factors at room temperature. When compared with conventional MEMS, a distinctive feature of 2D material and other nanomaterial NEMS like carbon nanotubes and smaller nanowires is that the very high aspect ratio leads to very low spring constants. As seen in the earlier discussion on thermal motion and dynamic range, the thermal fluctuations at the drive frequency are small compared with the drive amplitude. However, following from Eq. (11), the total root mean square dynamic thermal fluctuation of a single eigenmode integrated over all frequencies at room temperature is much larger, $x_{rms} \sim 100$ pm. In other words, even before driving the system, the dynamic thermal fluctuations in nanomaterial NEMS are already large enough to drive the system into nonlinear coupling of eigenmodes.^{135,190}

While the role of FPUT nonlinear thermal fluctuations is clear at low temperature and in simulation [Figs. 10(a) and 10(b)], there has not yet been a direct measurement of how the fluctuations lead to the high dissipation of 2D resonators at room temperature. The best comparison comes from a similar system consisting of a carbon nanotube

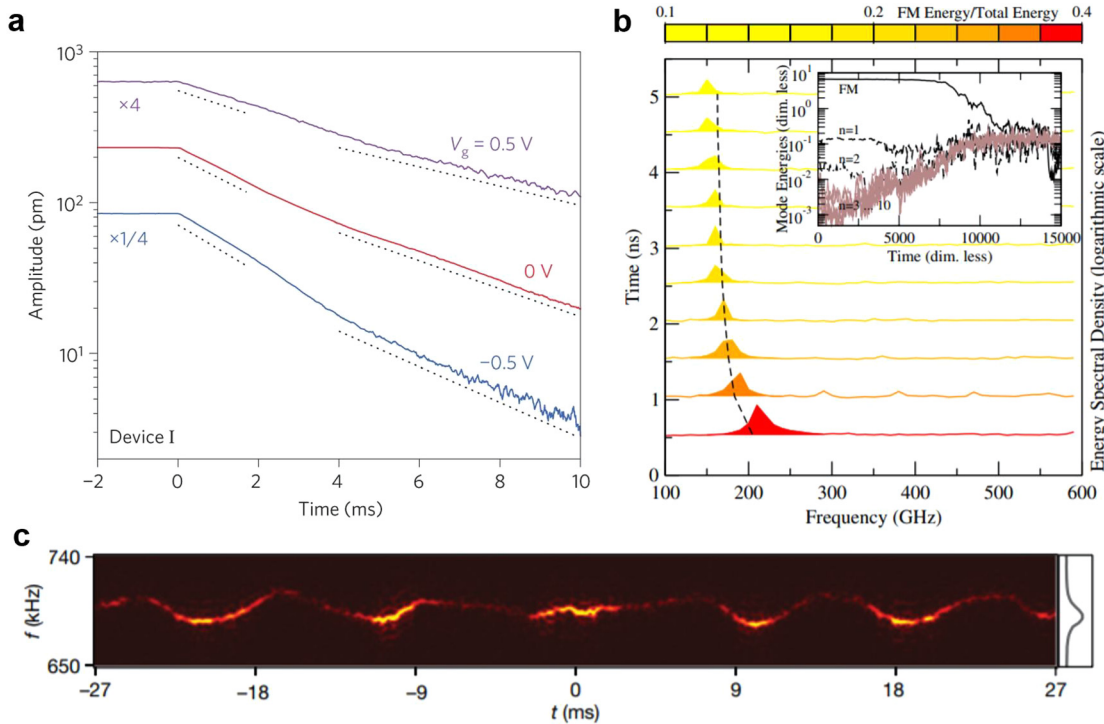


FIG. 10. Dissipation from nonlinear thermal fluctuations in nanomaterial NEMS. (a) Experimental ringdown measurement of a multilayer graphene resonator at cryogenic temperature for three different gate voltages. After $t = 0$, two distinct dissipation regimes are seen in the amplitude decay, with different damping coefficients. The different dissipation rates occur due to nonlinear mode coupling, which is more pronounced at high amplitudes, resulting in an additional energy escape channel.¹⁸⁰ Reprinted with permission from Güttinger *et al.*, Nat. Nanotechnol. **12**(7), 631–636 (2017). Copyright 2017 Springer Nature Customer Service Center GmbH: Nature Nanotechnology. (b) Ringdown simulation of a graphene membrane, which is initially excited at the fundamental eigenmode and then left to relax. The plot shows the spectral density at different time steps, and the color scale shows the area under the curve for the fundamental eigenmode. The inset shows the time evolution of the energy for the first 10 eigenmodes, showing the thermalization due to intrinsic nonlinear mode coupling.¹⁸¹ Reprinted with permission from Midtvedt *et al.*, Phys. Rev. Lett. **112**, 145503 (2014). Copyright 2014 American Physical Society. (c) Thermal dynamics of a carbon nanotube probed by an optical microcavity. The plot shows the wavelet transform of the time-dependent signal at different time steps around the main peak at $f \approx 700$ kHz, showing the fluctuating resonant frequency. The right plot shows the apparent resonance curve obtained with a longer integration time.¹¹² Reprinted with permission from Barnard *et al.*, Nature **566**(7742), 89–93 (2019). Copyright 2019 Springer Nature Customer Service Center GmbH: Nature.¹¹²

suspended over a micro-ring optical resonator, giving very high temporal fidelity. Figure 10(c) shows the amplitude of the dynamic thermal fluctuations of the carbon nanotube plotted vs time and frequency.¹¹² The data show that the instantaneous natural frequency of the nanotube fluctuates over time, resulting in a higher apparent dissipation, as shown by the time-integrated FWHM (plotted on the right). Whereas the apparent quality factor is about 40, the real quality factor is estimated as 4000–20 000 from the local time-series data. Effectively, the energy present in the higher eigenmodes translates to quasi-periodic changes on the stress of the membrane, leading to fluctuations in the frequency of the fundamental eigenmode, and broadening of the apparent time-averaged resonance.¹⁸⁶

There are several important implications of the nonlinear thermal fluctuations beyond dissipation. At room temperature, every eigenmode, not just the driven eigenmode, will be thermally occupied with high enough amplitude to drive the system nonlinearly, which can be enough to drastically alter the thermomechanical properties, like initial stress and apparent Young's modulus,⁸¹ thermal expansion coefficient,¹⁹¹ and heat transport.¹⁹² For static deformations, statistical mechanics and MD calculations provide the length scales and stress

values where the thermal fluctuations dominate over continuum mechanics models.^{193–198} However, a complete picture is still missing, which unravels the relative contributions of entropic and continuum mechanics on the dynamic behavior of 2D NEMS devices with different sizes and initial stresses.

V. COUPLED SYSTEMS

Many characteristics of 2D NEMS allow them to strongly couple to external coherent excitation and between different eigenmodes. For example, their high-frequency tunability and low onset of nonlinearity allow strong and tunable coupling between disparate eigenmodes.^{28,80,199} The high tunability of 2D resonators also permits building phononic crystals and waveguides with tunable response.^{123,200–202} The high light-matter interaction of 2D materials permits different forms of optomechanical coupling, such as photothermal back-action,⁷⁹ exciton-induced back-action,²⁰³ and valley optomechanics.²⁰⁴ In addition, the high mechanical flexibility of 2D layers allows their easy integration onto other M/NEMS to couple the motion of separate structures.^{205,206} Exploiting these couplings allows new forms of sensing and transducing exquisitely small forces across different physical

domains and between different systems, and can generate entirely new hybrid or metamaterials. In this section, we will review the diverse demonstrations of coupling in 2D NEMS.

A. Parametric coupling between eigenmodes in a single resonator

Parametric coupling of different eigenmodes within a single resonator is a phenomenon present in many classical and quantum systems,^{207,208} which has applications such as parametric drive, frequency stabilization, or multimode sensing.^{209–212} 2D NEMS are ideal systems to explore eigenmode coupling because of their frequency tunability and strong nonlinearity, giving the opportunity to tailor the harmonic alignment of the eigenmode frequencies, an important component of parametric coupling and an unusual capability in most M/NEMS.^{28,47,80,213,214} In this section, we will give a brief overview of parametric eigenmode coupling in 2D NEMS. A more in-depth analysis of this topic is given in two recent reviews on the dynamics of 2D membranes²¹⁵ and the thermomechanical physics of nanomechanical systems.¹⁸⁶

In the linear regime, eigenmodes of any mechanical resonator are by definition orthogonal and non-interacting, and each eigenmode can be treated as a distinct mass-spring-damper system. However, overlapping eigenmodes become coupled when considering the nonlinear phenomena discussed in Sec. IV D 3, such as the dynamic modulation of the tension in the membrane.²⁸ A more general form of Eq. (5) describes the dynamics of an eigenmode i , while including nonlinear interactions between other eigenmodes out to cubic order is^{190,215}

$$\ddot{z}_i + \gamma_i \dot{z}_i + \omega_i^2 z_i + \sum_{j=1}^N \sum_{k \geq j}^N C_{ijk} z_j z_k + \sum_{j=1}^N \sum_{k \geq j}^N \sum_{l \geq k}^N D_{ijkl} z_j z_k z_l = f_d \cos(\omega_d t). \quad (22)$$

Here, the terms C_{ijk} and D_{ijkl} are the nonlinear quadratic and cubic coupling coefficients describing the influence of eigenmodes j , k , and l on eigenmode i . As described in Sec. IV C 3, these terms rise from the geometry, and deflection of the membrane, but can also come from optical or electrostatic forces. For example, the case $i = j = k = l$ reduces C_{ijk} and D_{ijkl} to the quadratic and cubic nonlinearities of eigenmode i . These nonlinear coupling coefficients lead to energy exchange between eigenmodes and a host of new phenomena that are being actively explored. For example, they are related to the nonlinear dissipation from thermal fluctuations discussed in Sec. IV D 3.

Yet, another common form of coupling in NEMS, in general, and 2D NEMS, in particular, is parametric coupling.^{28,216} The equations governing the dynamics of two parametrically coupled eigenmodes are²⁸

$$\ddot{z}_i + \gamma_i \dot{z}_i + [\omega_i^2 + \Gamma_i \cos(\omega_p t)] z_i + \Lambda \cos(\omega_p t) z_j = f_i \cos(\omega_d t), \quad (23)$$

$$\ddot{z}_j + \gamma_j \dot{z}_j + [\omega_j^2 + \Gamma_j \cos(\omega_p t)] z_j + \Lambda \cos(\omega_p t) z_i = f_j \cos(\omega_d t), \quad (24)$$

where ω_p is the frequency of the parametric drive, also called the pump; Γ_i is the intramodal coupling constant of eigenmode i ; Λ is the

intermodal coupling constant; and ω_d is the drive frequency. In principle, the pump signal ω_p can be applied at any frequency. However, to achieve strong parametric coupling, the combined frequency of the coupling terms should resonate with the frequency of the eigenmodes being excited. As an example, suppose $\omega_d = \omega_i$ and the pump frequency is the detuning between the eigenmodes $\omega_p = \omega_j - \omega_i$. Then, the coupling terms will have solutions of the form $\cos(\omega_p t) \cos(\omega_d t) = \cos[(\omega_j - \omega_i)t] \cos(\omega_i t)$ which through mixing will produce terms of the form $\cos(\omega_j t)$. Thus, the coupling matches the frequency ω_j of the j -th eigenmode in Eq. (24), amplifying its motion near resonance.

The high tunability of 2D NEMS allows tuning not only the frequency of individual eigenmodes but also the strength of the coupling. For instance, because the different eigenmodes have large but different tuning rates with electrostatic voltage, many 2D resonators can be tuned to reach an avoided crossing, where two modes approach each other in frequency. In turn, the small frequency gap leads to large cooperativity,²⁰⁰ maximizing the strength of parametric coupling between the eigenmodes.

Figure 11(a) shows a schematic diagram of two parametrically coupled eigenmodes 1 and 2 in a monolayer graphene resonator.²⁸ By convention, the ordering of the eigenmodes is such that $\omega_2 > \omega_1$. Application of a pump signal with an angular frequency of $\omega_p = \omega_1 + \omega_2$ parametrically drives both eigenmodes. Figure 11(b) shows the effective dissipation rate γ_1 of the first eigenmode as a function of pump voltage V_p . The $4\times$ decrease in γ_1 from $V_p = 0$ to 2 V results from compensating the dissipation to the phonon bath by the pump energy.²⁸ Figures 11(a) and 11(b) represent the case of a pump in the blue sideband of eigenmode 2, because the pump frequency $\omega_p = \omega_2 + \omega_1$ is higher than ω_2 . In this situation, the pump amplifies the motion of both eigenmodes 1 and 2. Similarly, application of pump on the red sideband of eigenmode 2, that is, with frequency $\omega_p = \omega_2 - \omega_1$, also parametrically couples both eigenmodes, but leads to the opposite effect on eigenmode 1, damping or cooling the motion.²⁸ While cooling down eigenmodes through mechanical pumping is not capable to bring them to their quantum states, which is commonly done with optomechanical techniques,²¹⁷ it still holds promise as a method to manipulate phonon exchange between eigenmodes once they are in their quantum states.

As another example, Fig. 11(c) shows the schematic of a process involving three eigenmodes of a monolayer graphene resonator, whose frequencies are labeled ω_1 as the eigenmode of interest, ω_{sb} for the sideband eigenmode, and ω_c for the phonon cavity eigenmode.⁸⁰ In this scheme, the gate voltage is carefully tuned to bring the system to the point where $\omega_1 + \omega_{sb} = \omega_c$. The goal of aligning the three eigenmodes to this condition is to amplify the magnitude of the pump drive applied at ω_{sb} coupling the phonon cavity to the eigenmode of interest. Indeed, when the pump frequency resonates with the frequency of the sideband eigenmode, its effects are amplified by the quality factor of the sideband eigenmode. When weakly driving the resonator at frequency ω_1 while applying a pump voltage at ω_{sb} , phonons go from the first eigenmode into the phonon cavity eigenmode. Figure 11(d) shows the thermal noise density of the resonator around ω_1 for different pump voltages. The total energy or effective temperature of the first eigenmode decreases by $\sim 30\%$ for pumping voltages of 0–46 mV, which shows strong cooling strength compared to typical MEMS.⁸⁰

Finally, there is also the coupling between the low-frequency (MHz–GHz) out-of-plane vibration, which can also be thought of as flexural phonons, and the high-frequency (1–100 THz) intralayer

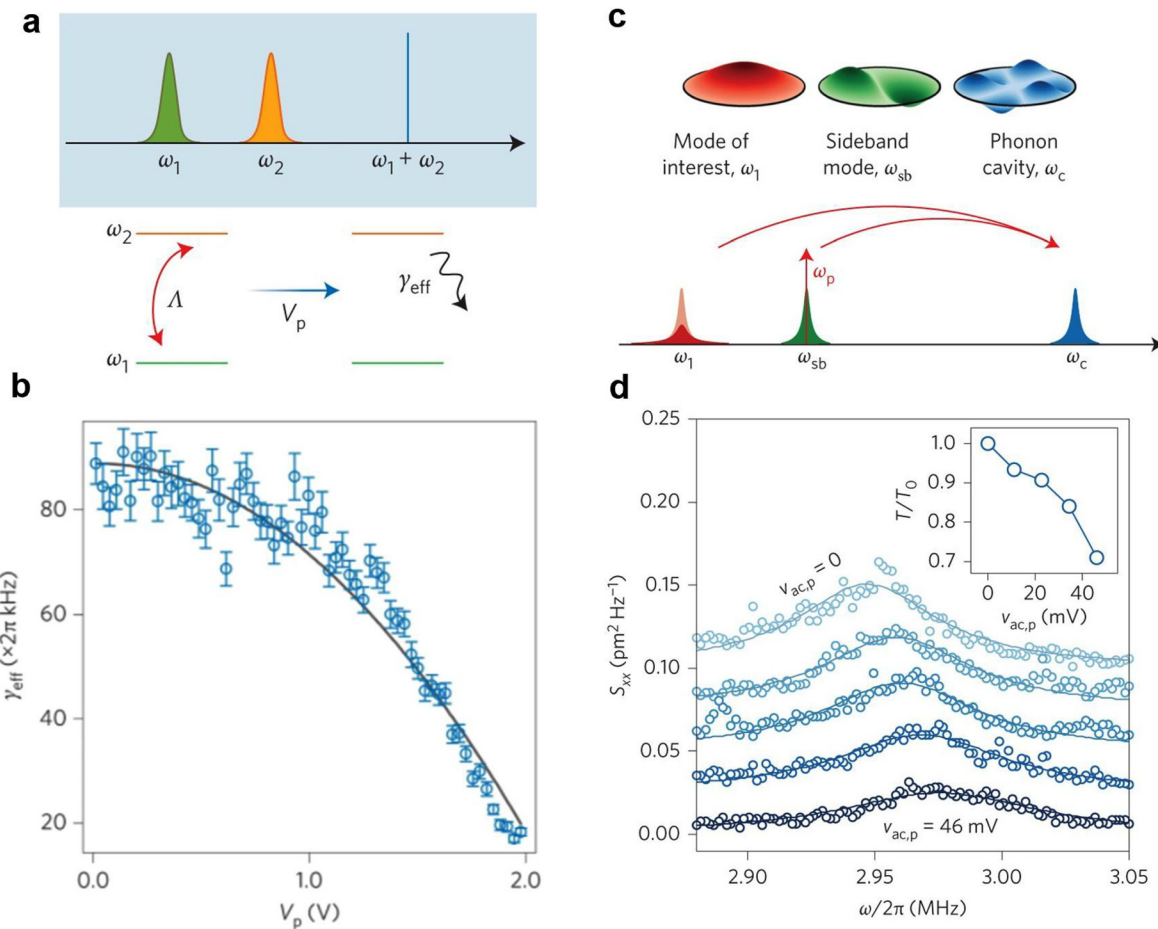


FIG. 11. Dynamics of coupled eigenmodes in 2D resonators. (a) Schematics of a Stokes sideband process for a monolayer graphene resonator.²⁸ Energy is pumped in the system by an RF voltage with frequency equal to the sum of the frequencies of two eigenmodes. (b) Reduction of the effective dissipation rate of an eigenmode with frequency $\omega_1/2\pi = 94.9 \text{ MHz}$ due to parametric amplification.²⁸ (c) Schematic of an anti-Stokes sideband process involving three mechanical eigenmodes of a monolayer graphene resonator.⁸⁰ (d) Response of the fundamental eigenmode ($\omega_1/2\pi = 3 \text{ MHz}$) as a function of a drive voltage applied with the frequency of the sideband eigenmode ($\omega_{\text{sb}}/2\pi = 3.8 \text{ MHz}$). The fundamental eigenmode is cooled as the energy is transferred to the phonon cavity eigenmode (with frequency $\omega_c/2\pi = 6.8 \text{ MHz}$).⁸⁰ Figures (a) and (b): adapted with permission from Mathew *et al.*, Nat. Nanotechnol. **11**, 747 (2016). Copyright 2016 Springer Nature Customer Service Center GmbH: Nature Nanotechnology. Figures (c) and (d): adapted with permission from De Alba *et al.*, Nat. Nanotechnol. **11**(9), 741–746 (2016). Copyright 2016 Springer Nature Customer Service Center GmbH: Nature Nanotechnology.

phonons from interatomic vibrations. This form of coupling has been observed by driving graphene and MoS₂ resonators in the nonlinear regime, while simultaneously probing the Raman spectra.^{218–220} The dynamic nonlinear motion leads to a change in strain in the membrane, which leads to a shift in the Raman modes. Because of the orders of magnitude frequency difference (MHz vs 100s of THz), there is a low cooperativity between the in-plane and flexural modes, so the low-frequency dynamic motion induces an average change in the tension and resulting phonon modes rather than the parametric coupling discussed in the previous examples.

B. Coupled resonators and mechanical metamaterials

Mechanically coupling two or more resonators with similar frequencies leads to overlap of the eigenmodes, nonlinear coupling, and

avoided crossing similar to that seen when two eigenmodes are degenerate in a single resonator. This mechanical coupling is most commonly achieved in MEMS by designing an overlap between the distinct resonators. In contrast, the strong in-plane moduli and weak van der Waals coupling to the substrate allow off resonance mechanical waves to propagate along 2D materials even when they are not suspended. This propagation allows coupling between distinct resonators, which might be connected by a long suspended bridge¹²³ or even unsuspended portions of 2D materials.^{221,222} The coupling strength Ω , seen as the splitting of frequencies in an avoided crossing, is as high as 11 MHz for 100 MHz resonances.²²² As a comparison, most coupled cantilever MEMS show coupling strengths on the order of a few kHz on the 100 kHz–10 MHz resonant frequency range.^{223,224}

Coupling an array of resonators together forms a phononic waveguide, a one-dimensional mechanical metamaterial.²²⁵ Phononic

waveguides have distinct band structures, which allows propagation or suppression of acoustic waves into well-defined frequency bands, with potential applications in RF filtering, in mechanical computing, and reconfigurable material properties.^{226,227} The first demonstration for a phononic waveguide from 2D materials used hexagonal boron nitride.²⁰¹ The hBN waveguide consisted of 10–40 couple resonators with frequency bands in the 15–50 MHz range. Wave guiding requires that the coupled resonators have very close natural frequencies, so a thick crystal (~ 40 nm) was chosen to avoid heterogeneity in membrane stress that often comes with 2D monolayers. For most purposes, this initial demonstration did not leverage the strengths of 2D materials, but the general idea is very promising. For example, 2D material-based phononic waveguides could be made tunable through electrostatic gating or may be used to couple the photonic properties of 2D materials to the mechanical band structure to creating new kinds of photonic–phononic converters and quantum transducers.

C. Optomechanical coupling

Optomechanical coupling and back action results from the coherent coupling between optical fields and mechanical vibrations, and has applications in active cooling to bring MEMS into the quantum regime to act as mechanical qubits.^{5,228} Typically, in MEMS, optomechanical coupling is achieved by integrating a mechanical resonator with a photonic resonator to achieve high fluence where light waves coherently interact with the mechanical resonance many times. Because of their strong light–matter interactions per unit thickness and high force sensitivity, 2D NEMS have enormously strong optomechanical coupling.^{79,203} Moreover, the unique valley physics of many transition metal dichalcogenides enable new forms of exciton coupling.²⁰⁴

The most commonly studied forms of optomechanical back action in typical MEMS/NEMS result from radiative pressure, which involve elastic momentum transfer of photons reflected off a material, and photothermal pressure resulting from the absorption of photons.²²⁹ In 2D NEMS, the strong light–matter interactions mean the photothermal pressure dominates. For instance, Fig. 12(a) shows the relation between the effective dissipation rates of a graphene resonator under increasing laser powers.⁷⁹ The inset shows the corresponding tuning of the resonance spectrum. Figure 12(b) shows the dynamical reflectance of a MoSe₂ resonator under a tunable laser with different wavelengths.²⁰³ In both cases, a diffraction limited laser spot is shined on the sample, generating a Fabry–Pérot interferometer of the 2D membrane with respect to a reflecting back gate. The intensity of the light incident on the 2D membrane depends on the distance with respect to the back gate. The vibration of the membrane leads to a change in absorption of photons and modulation of stress of the membrane as it vibrates, generating a position-dependent gradient in the photothermal force. These coherent interactions are distinct from static photothermal effect, say by heating a sample with a laser to change the average stress. In both graphene and MoSe₂, the gradient generated by the photothermal force either decreases or increases the effective dissipation depending on its phase relative to the phase of vibration.

Another way to couple light with 2D NEMS vibrations is through their excitonic properties. Figure 12(c) shows a schematic of valley optomechanical coupling in transition metal dichalcogenide resonators in a magnetic field gradient. Due to spin–orbit coupling, the

energetically degenerate K and K' valleys in monolayer transition metal dichalcogenides like MoS₂ have opposite spin states. As a result, left or right circularly polarized light shined on the monolayer will selectively excite either the K or K' valley, respectively, leading to a net spin polarization in the sample. This gives rises to an out-of-plane net force on the membrane with a magnitude proportional to the net valley population, $F \propto |N_K - N_{K'}| \nabla B$ when an external magnetic field gradient ∇B is applied. Figure 12(d) shows the frequency response of the MoS₂ membrane optically actuated by modulating the polarization of light in a fixed magnetic field gradient while keeping the intensity constant. When modulating between horizontally and vertically polarized light, no resonance is visible. However, modulating between left and right circularly polarized light leads to a resonance signal due to the magnetic force generated by coherently modulating the net valley population.²⁰⁴ There are also exciting predictions that have yet to be realized on quantum optomechanical coupling between 2D excitons and strain.^{230,231}

D. Hybrid coupled systems

While the previous examples focused on monolayer or multilayer membranes from single materials, most M/NEMS need more than one layer to operate. Enabling functionality and probing properties not available in single materials require integrating disparate materials together. In this section, we will review the integration and types of coupling in either heterostructures of different 2D materials or hybrid systems in which 2D materials are coupled to thin-film NEMS materials.

1. Interlayer interactions in 2D heterostructures

Utilizing NEMS from 2D heterostructures instead of single 2D materials provided new strategies such as enhancing functionalities and probing fundamental friction in van der Waals interfaces or enabling mechanical coupling to quantum states.

The sensitivity of 2D resonators is low enough to measure the very small forces resulting from dislocation motion or slip at van der Waals interfaces, creating a new tool for probing interfacial mechanics. Figure 13(a) represents the tuning curve of amplitude vs frequency and gate voltage obtained from a Bernal-stacked bilayer graphene resonator.²⁶ In contrast to the smooth tuning curve from the monolayer resonator shown in Fig. 6(a), the Bernal-stacked bilayer graphene shows stochastic jumps in the tuning curve (indicated with white arrows). These jumps originate from a change in the initial stress due to the creation and annihilation of single stacking faults (solitons) at the van der Waals interface and are instigated by the stress induced by the electrostatic gate. Meanwhile, not shown, the tuning from twisted bilayer graphene once again shows a smooth tuning curve due to the superlubric slip at the incommensurate interface, where the membrane effectively behaves as two independent monolayers. Using the same approaches has unraveled the effect of interfacial friction and adhesion on the resonance properties in bimorphs from 2D material heterostructures including graphene-MoS₂^{64,65} or graphene-hBN.^{66,67} These heterostructures are fabricated by stacking two layers. Depending on the procedure, this stacking process can lead to very clean interfaces or having process residue or bubbles stuck at the interface. Clean interfaces lead to smooth tuning curves similar to twisted bilayer graphene,⁶⁵ while small amounts of residue or bubbles lead to kinks, hysteresis,⁶⁴

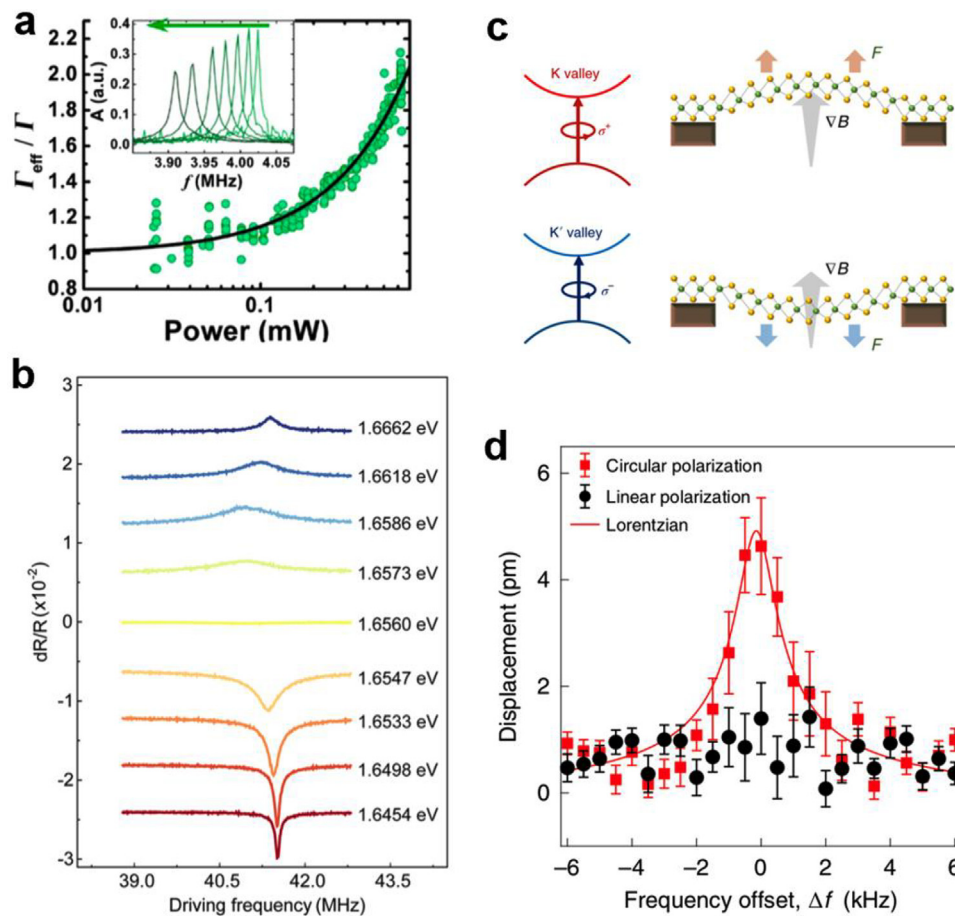


FIG. 12. Optomechanical coupling in 2D resonators.(a) Optomechanically induced dissipation in a graphene resonator, leading to enhancement of the effective dissipation rate with the laser power.⁷⁹ Reprinted with permission from Barton *et al.*, Nano Lett. **12**(9), 4681–4686 (2012). Copyright 2012 American Chemical Society. (b) Differential reflectance of a monolayer MoS₂ resonator under different driving frequencies and probing laser photon energies.²⁰³ Reprinted with permission from Xie *et al.*, Nano Lett. **21**(6), 2538–2543 (2021). Copyright 2021 American Chemical Society. (c) Schematic of suspended monolayer MoS₂ over the substrate coated with Ni/Fe Permalloy films. The Permalloy films generate field gradient by distortion of the local field. Pump laser modulated between left and right circularly polarized and probe laser is applied to the membrane.²⁰⁴ (d) Mechanical motion is actuated with circular polarization through valley–mechanical force.²⁰⁴ Figures (c) and (d): adapted with permission from Li *et al.*, Nat. Photonics **13**(6), 397–401 (2019). Copyright 2019 Springer Nature Customer Service Center GmbH: Nature Photonics.

23 July 2023 15:16:56

or dips⁶⁶ in the tuning curve from high friction slip at the interface or delamination in the bubbles.⁶⁷

An interesting, but so-far unexplored question, is how the out-of-plane flexural modes would affect the dynamic interlayer phonon modes. As discussed above in Sec. V A, there is a large frequency difference between the in-plane modes of 2D materials (\sim THz)²³² and out-of-plane flexural modes (\sim MHz). As a result, there is unlikely to be a parametric coupling. However, there could be a modulation of the mode frequency due to average changes in tension or changes in stacking from interlayer slip.

Another feature of heterostructures as 2D NEMS is that different materials may have different functionalities. For instance, there are many 2D materials, which have outstanding properties but are environmentally sensitive, so cannot make freestanding membranes without degradation during processing. Encapsulating NbSe₂ with graphene and suspending the structures as membranes allow the

creation of a superconducting 2D NEMS from a material, which is unstable by itself. The superconducting heterostructures showed impressively high-quality factors of 245 000 at low temperatures,⁶² which are comparable to the best-reported graphene resonators.^{126,138} In addition, the low intrinsic resistance of NbSe₂ preserved high-quality factors with an increase in gate voltages, which was one of the main challenges in graphene-based resonators.^{126,138} This research demonstrates that encapsulation 2D heterostructures provide a route to overcome challenges in single material 2D NEMS.

2. Coupled graphene-NEMS systems

Additionally, the features of 2D materials, like high mechanical strength, low mass, and high electronic mobility couple well with other NEMS. For example, graphene is an excellent massless electrode when integrated with SiN_x²³³ or AlN_x resonators.¹⁰⁷ Figure 13(b) shows

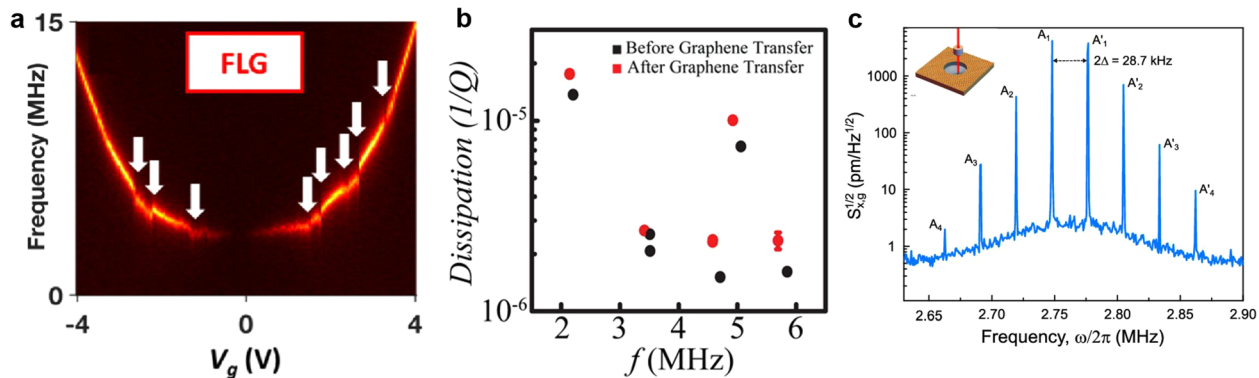


FIG. 13. Heterostructure-based 2D NEMS and hybrid systems. (a) 2D map of amplitude vs frequency and gate voltage obtained from Bernal-stacked bilayer graphene. Stochastic jumps are observed in the tuning curves, stemming from soliton creation and annihilation.²⁶ Reprinted with permission from Kim *et al.*, *Nano Lett.* **20**(2), 1201–1207 (2020). Copyright 2020 American Chemical Society. (b) Dissipation vs frequency for Si_3N_4 drum resonator before (black) and after (red) graphene.²³³ Reprinted with permission from Lee *et al.*, *Nano Lett.* **13**(9), 4275–4279 (2013). Copyright 2013 American Chemical Society. (c) Phononic frequency comb generated in a coupled graphene-SiN_x system, schematically shown on the top left. The 28.7 kHz separation between peaks is the same as the detuning between the two hybrid eigenmodes formed by coupling one graphene eigenmode to one SiN_x eigenmode.²³⁵ Reprinted with permission from Singh *et al.*, *Nano Lett.* **18**(11), 6719–6724 (2018). Copyright 2018 American Chemical Society.

dissipation vs frequency for a SiN_x drum resonator. Black and red points represent before and after graphene transfer, respectively. Using graphene in this setting showed an average reduction of less than 30% in the quality factors of the resonators. At the same time, the graphene can still be used to tune or actuate resonator motion. In contrast, polycrystalline metal films are both high density and have high internal friction, so depositing metal thin films onto the resonant portions of low mass NEMS causes mass loading that can dramatically alter both the frequency and quality factor. For example, depositing Cr films on SiN_x reduces the quality factor by more than a factor of 4.²³⁴ This shows great potential for using graphene as a massless electrode in NEMS.

Another way to create hybrid coupled systems is by embedding a graphene membrane into a larger silicon nitride membrane. The two systems are orders of magnitude different in size and mass, yet have similar resonance frequencies. This puts the resonators into strong parametric coupling leading to energy pumping from one system into the other in driven systems,²³⁵ as well as the undriven thermal fluctuations.²³⁶

This strong coupling may be combined with the tunability of graphene to generate new behavior. Electrostatically tuning the frequency of the graphene to one of the silicon nitride eigenmodes allows the modes to hybridize, which means one system can be used to drive the other system and parametrically amplify the motion.²³⁵ As shown in Fig. 13(c), this strong coupling leads to giant nonlinearity, which can be used to generate phononic frequency combs.²³⁷ Specifically, parametrically driving graphene into nonlinear motion tuned to the same frequency as a linear silicon nitride eigenmode leads to the formation of sidebands. Increasing the parametric amplification leads to additional sidebands and a phononic frequency comb in the graphene motion.

VI. APPLICATIONS

All the exquisite properties of 2D materials discussed in Secs. IV and V make 2D materials excellent candidates for the next generation of NEMS, from low-powered actuators, tunable transducers, and

exquisitely sensitive sensors. Moreover, the high responsivity of 2D resonators to changes in strain or internal forces makes 2D NEMS a valuable tool for probing fundamental material properties, phase transitions, and quantum phenomena that are difficult to detect or transduce with other techniques. In this section, we will review select state-of-the-art applications of 2D mechanical resonators. We will focus on applications, which specifically demand dynamic mechanical motion of the membrane, and will not cover the diverse other forms of transduction, which may be utilized in 2D devices, such as sensing via changes in conductivity of static suspended membranes.

A. Actuators

MEMS actuators are transducers that convert electrical signal to mechanical motion and vice versa. The main uses of MEMS actuators are in electronic applications such as switches and variable capacitors, or in devices that use mechanical displacements to modulate signals, such as speakers and scanning micro-mirrors. In most cases, attempts to further miniaturize MEMS actuators by utilizing 2D materials use the same operational principles and device structures. However, due to their ultra-thin nature, utilizing 2D materials generally leads to lower power consumption and higher transduction efficiencies. Table I summarizes the demonstrations of different kinds of electromechanical actuators made from graphene, as well as the relevant metrics of performance for each application.

1. Switches

Compared to electronic switches, such as transistors, MEMS switches provide higher on-off ratios and higher temperature and environmental stability. These MEMS switches have broad applications on components operating in harsh environments, as well as in low powered RF circuits for mobile communication. The simplest and most common types of MEMS switches are 2-terminals devices where one electrode is a suspended plate or cantilever, and the other is located underneath. By applying a critical pull-in voltage between the

TABLE I. Characteristics of 2D NEMS actuators.

Application	Principle	Material system	Reported range	Performance metrics	Advantages over MEMS	Challenges and limitations
Electro-mechanical switch	Electrostatically actuated 2-contact switch	Graphene (Refs. 238–241) FL Graphene (Refs. 240 and 242)	0–500 nA (max)	Pull-in voltage (min to max): 0.5–10 V Switching time (min to max): 40–100 ns	Lower pull-in voltage	Moderate number of cycles (50 000 max)
	Electrostatically actuated 3-contact switch	Graphene (Ref. 243)	0–30 nA	Pull-in voltage (min to max): 20–45 V	Lower pull-in voltage	Small number of switching cycles (30 max)
Voltage-controlled oscillator	Resonator controlled by feed-back-loop	Graphene (Ref. 97)	47–51 MHz	Tuning responsivity: 2.7 MHz V ⁻¹ Intrinsic phase noise: −73 dBc Hz ⁻¹	Higher tunability, compactness, lower power	High phase noise
Acoustic speaker	Thermoacoustic	Graphene (Ref. 244)	2–50 kHz	Power 0–0.25 W	Lower distortion (high frequencies), transparent	High distortion at low frequency
		Graphene on PDMS (Ref. 245)	111 kHz	Power 0–0.25 W	Transparent, flexible	High distortion at low frequency
	Electrostatically driven diaphragm	FL graphene (Ref. 246)	20 Hz –20 kHz	Power <1 μW	Lower distortion, lower power	No significant limitations

two terminals, the suspended component deflects and makes an electrical contact with the bottom electrode. Another design applies a 3-terminal geometry where source, drain, and gate are electrically isolated, whereas the source is electrically connected to a suspended element. Applying a voltage to the gate terminal pulls down the suspended portion, closing the contact between source and drain.

Figure 14(a) shows a schematic example of a 3-terminal graphene switch. Figure 14(b) shows the corresponding drain-source current vs gate voltages at a fixed source-drain bias of 4 V. Contact in the switch occurs at a gate voltage of about 30 V. Table I summarizes other examples of both 2-terminal and 3-terminal switches.^{238–243,247} The pull-in voltage is in the range of 0.5–10 V for device size ranging from 1 to 600 μm^2 in the 2-terminal geometry and 20–45 V in the 3-terminal case for a device size of $\sim 25 \mu\text{m}^2$. In comparison, typical MEMS switches have pull-in voltages in the range of 3–100 V for device sizes ranging from 7200 to 15 mm².²⁴⁸ The reason is the reduction of the pull-in voltage in MEMS require smaller spring constants, which typically require making larger structures, such as cantilevers, increasing the overall area occupied by the switch. Thus, utilizing graphene reduces the power consumption needed for actuation while occupying a fraction of the area of current MEMS switches. The downside of the smaller area is that much larger current densities are needed to drive the same on current. For all 2D switches, the source-drain currents are limited to the range of 0–1 μA , with the maximum current limited by Ohmic heating causing damage in the graphene. However, a second major limitation is the low number of cycles before failure resulting from irreversible stiction and tearing due to high mechanical stresses or excessive heating. The best demonstration so far only resulted in a maximum of 5000 cycles for single-crystal graphene vs several millions in commercial MEMS switches.²⁴⁸ Resolving this problem requires

improved uniformity of membrane stress and morphology for more uniform material adhesion.

2. Oscillators

MEMS-based oscillators generate output signals with higher-frequency precision, lower power, and smaller footprint compared to electronic oscillators and are frequently used in timing applications such as clock generators. A typical MEMS oscillator is composed of a mechanical resonator with a programmable integrated circuit that feed-backs the motion of the resonator as a voltage on the gate to amplify the thermally driven resonance. As summarized in Table I, a graphene drum head oscillator showed a tunable resonance of 47–51 MHz, controlled by electrostatically tuning the stress on the graphene. The 4 MHz range was only limited by the utilized feedback circuit,⁹⁶ and thus, it can be extended at least by a factor of 10.⁸⁵ The tuning sensitivity was 2.7 MHz/V, and phase noise was approximately −40 dBc/Hz at zero-offset frequency. Commercial MEMS-based voltage controlled oscillators (VCOs) have frequency ranges of 1–100 MHz while displaying phase noises < 80 dBc/Hz. However, the graphene VCO showed much lower power consumption of < 1 μW , compared with the mW range power consumption for typical MEMS VCOs (e.g., SiTime XO series). Thus, graphene oscillators have potential for applications in remote and ultra-miniaturized systems such as *in situ* mass sensing and RF signal processing.

3. Speakers

MEMS actuators have great potential in sound applications. Similar to oscillators, MEMS speakers work based on the vibrations of

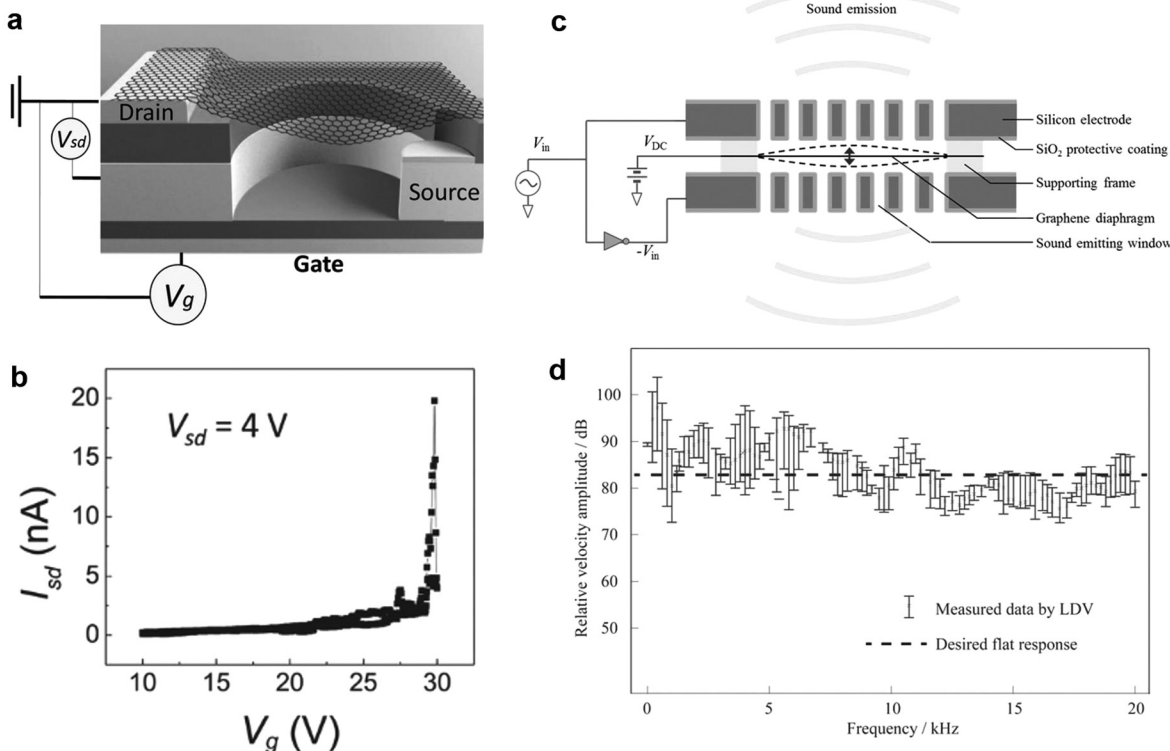


FIG. 14. Actuators from 2D NEMS. (a) schematic of a 3-terminal graphene-based NEMS switch.²⁴³ (b) Corresponding current I_{sd} vs gate voltage V_g for a graphene based a 3-terminal NEMS switch. The device switches at around $V_g = 30$ V.²⁴³ (c) Graphene speaker.²⁴⁶ The graphene is actuated by two perforated silicon electrodes that allow air in and out of the diaphragm. (d) Vibration velocity response of the membrane in the audible range. This measurement was done using laser Doppler velocimetry (LDV) on the membrane so does not include extrinsic effects rising from the final assembly of the speaker. Panels (a) and (b): Reprinted with permission from Liu et al., *Adv. Mater.* **26**(10), 1571–1576 (2014). Copyright 2014 Wiley-VCH GmbH. Panels (c) and (d): Reprinted permission from Q. Zhou and A. Zettl, *Appl. Phys. Lett.* **102**(22), 223109 (2013). Copyright 2013 AIP Publishing LLC.

a membrane (or diaphragm), which is actuated electrostatically or thermally to produce sounds. Compared to more conventional audio-transducers, MEMS devices have higher signal fidelity while occupying less space. Table I summarizes the performance of graphene speakers,^{244–246} while Fig. 14(c) shows the design of one specific electrostatic graphene speaker, composed of a multilayer graphene diaphragm with 7 mm diameter suspended between two perforated silicon plates that provide gates for actuation.²⁴⁶ Figure 14(d) shows the velocity amplitude for frequencies in the audible range (2–20 kHz). The nearly flat response curve is responsible for very small signal distortion and is close to that of an ideal speaker. The flatness is a result of the large dissipation of the graphene motion by the surrounding air, which is possible due to its ultra-high aspect ratio.

Another way of driving the motion of the membranes is to simply expand them through Joule heating, in the so-called thermoacoustic speakers. Both the electrostatic and thermoacoustic designs have advantages. Electrostatic speakers cover the entire audible range while consuming power that is six orders of magnitude less than the thermoacoustic design. The electrostatic speakers also have a much flatter frequency response curve compared to most commercial speakers.²⁴⁶ On the other hand, the main advantage of thermoacoustic speakers is that it can be made on a transparent substrate or integrated into screens.

B. Sensors

Another important application of MEMS is in sensing of external signals or forces: electronic, chemical, mechanical, quantum, etc. In general, the sensitivity limit of MEMS decreases for decreasing spring constant and mass, which means that 2D materials are intrinsically well suited for sensing. A second advantage is that 2D materials are both electrically active and mechanically strong, so they make up membranes, which self-sense their deflection to measure external signals rather than having to integrate mechanical and electronic components together as is typically done in conventional MEMS. 2D NEMS have been demonstrated for sensing of pressure,^{129,249–253} vibration/sound,^{70,254–257} force,^{111,138} acceleration,²⁵⁸ mass/chemicals,²⁵⁹ electromagnetic radiation,²⁶⁰ cell motion,²⁶¹ and flow rate.²⁶² Table II summarizes the demonstrations of different kinds of sensors made from 2D materials, as well as the relevant metrics of performance for each application. Most of these demonstrations are comparable to or outperform the state-of-the-art sensors. However, all suffer from low control and reproducibility that is a challenge across all nanomaterial devices.

1. Pressure sensors

MEMS pressure sensors transduce a pressure difference across a suspended membrane into an electrical signal. The main advantages of

TABLE II. Characteristics of 2D NEMS sensor applications.

Application	Principle	Material system	Reported range	Performance metrics	Advantages over MEMS	Challenges and limitations
Pressure sensing	Frequency shift	MoS ₂ (Ref. 128) Graphene (Refs. 129 and 131) FL graphene ¹³⁰ MXene ⁵⁸	10 ⁻³ –10 ³ mbar	Responsivity (min to max): 9–32 kHz mbar ⁻¹	Better sensitivity, compactness	Nonlinear response
	Piezoresistance	Graphene (Refs. 250 and 251), PtSe ₂ (Ref. 255)	0.2–1000 mbar	Responsivity (min to max): 4×10^{-6} to 5.5×10^{-4} mbar ⁻¹	Better sensitivity, compactness	Hermeticity
	Capacitance change	Graphene (Refs. 252 and 253)	0.5–1000 mbar	Responsivity: 0.1 aF Pa ⁻¹ (single) 47.8 aF Pa ⁻¹ mm ⁻² (array)	Better sensitivity, compactness	Hermeticity
Vibration sensing	Amplitude modulation	Graphene (Ref. 254)	1–100 MHz	Responsivity: 17 pA pm ⁻¹ Resolution: 7 pm Hz ^{-1/2}	Smaller size, high resolution ultrasonic imaging	...
2.5 cm Acoustic sensing	Condenser microphone	Graphene (Ref. 263)	0.1–500 kHz	Responsivity: 92 nm Pa ⁻¹ at 5.5 kHz	Higher fidelity, wider BW, lower power	...
	Fiber-optic-coupled Fabry-Pérot interferometry	FL graphene (Refs. 264 and 265) FL graphene (Refs. 255 and 257) MoS ₂ ²⁵⁶	0.1–1000 kHz	Responsivity: 1 mV Pa ⁻¹ at 10 kHz Resolution: 0.77 Pa Hz ^{-1/2} at 5 Hz	Wider BW, lower power	...
Force sensing	Force displacement	Graphene 300 K (Ref. 113) FL graphene 15 mK (Ref. 138)	BW: 35 kHz, (Ref. 113) 200 Hz (Ref. 138)	Resolution: 0.15 fN Hz ^{-1/2} , (Ref. 113) zN Hz ^{-1/2} (Ref. 138)	Better sensitivity	...
Acceleration sensing	Piezoresistance	Graphene (Ref. 258)	0–27 kHz	Resolution: 50 μ g Hz ^{-1/2} at 100 Hz	Smallest accelerometer	...
Mass sensing	Frequency shift	Graphene (Ref. 259)	5–8 ppb (H ₂ in Ar)	Minimum sensitivity: 886 zg	Better sensitivity	Selectivity
Bolometer	Frequency shift	Graphene (Ref. 260)	1–100 nW incident power	Resolution: 2 pW Hz ^{-1/2} BW: 0.01–1.3 MHz	Better sensitivity and higher speed	Limited BW for high-frequency transduction
Cell sensing	Membrane deflection	Graphene (Ref. 261)	0–60 nm	Resolution: 0.3 nm Hz ^{-1/2} at 1 Hz	Better sensitivity, speed and label-free detection	...
Flow sensing	Piezoresistance	Graphene (Ref. 262)	Flow speed 5–56 m/s	Responsivity: 710 ⁻⁸ m s ⁻¹	Compactness, large DR	Adsorption of molecules

MEMS-based pressure sensors are higher accuracy, fast response, compactness, and ease of integration with readout electronics. Table II shows the characteristics of pressure sensors made with 2D materials, which are classified into three categories depending on the sensing mechanism: the resonant frequency,^{129,130} piezoresistance,^{249–251} or capacitance change.^{252,253} Furthermore, each demonstration may be further classified with resonators that form cavities, which are hermetically sealed^{129,249–253} or not sealed (squeeze-film).¹³⁰ Regardless of

approach, 2D pressure sensors demonstrate sensitivity to measure pressure differentials of an atmosphere down to \sim 0.1 mbar. In contrast, most commercial MEMS sensors have ranges from hundreds of mbars to a few bars (e.g., STMicroelectronics LPS series). This improvement in sensitivity to pressure is because the responsivity of 2D sensors is orders of magnitudes larger. For example, the best responsivity of squeeze-film pressure sensors is 32 kHz/mbar¹²⁹ for graphene vs \sim 0.2 kHz/mbar for silicon.²⁶⁶ For most 2D pressure

sensors, the main challenge is guaranteeing hermeticity over long periods of time to avoid drifting of readout values because of internal leakages. Of smaller importance, the challenge in squeeze-film sensors is the non-linear responsivity, which requires more complex calibration and readout schemes compared to linear sensors.

Modifying the structure of the membrane allows pressure sensors to get turned into flow sensors. For example, in perforated graphene/SiN heterostructure membrane, different flow rates cause different pressure differentials across the membrane, which can be monitored through changes in the piezoresistance of the graphene.²⁶² The reported measurable range is 5–56 m/s, whereas typical MEMS flow sensors based on deflecting elements have ranges of 0–20 m/s.²⁶⁷ However, one challenge is the unwanted adsorption of gas molecules on the graphene surface, which modifies the conductivity, and requires additional calibrations of the flow–resistance relationship. Thus, the concept of a graphene flow sensor is worth further exploration, including operation based on shear stresses.²⁶⁸

2. Acoustic and vibration sensors

Both acoustic and vibration sensors transduce external mechanical sound or vibrations into an electrical or optical signal. The design of MEMS acoustic sensors is very similar to pressure sensors, usually consisting of a suspended membrane or thin plate that deflects upon application of sound pressure. In the case of vibration sensors, the effective mass of the suspended element provides the inertial driving force. As usual, the advantages of using MEMS for these applications are integration with electronics, small size, and low power without sacrificing sensitivity. Table II summarizes the characteristics of 2D NEMS-based vibration and acoustic sensors.^{254–257,263} For the 2D vibration sensor shown in Table II, mounting the substrate onto a vibrating piezoactuator induces vibrations of a monolayer graphene membrane, whose amplitude is electrically read and calibrated to the amplitude of motion of the substrate.²⁵⁴ The bandwidth covers most of the high-frequency (HF) and very-high-frequency (VHF) range of 1–100 MHz, and responsivity is on the order of $\sim 1 \text{ pA}/\text{pm}$. The high-frequency range makes 2D vibration sensors useful for nanotechnology applications such as ultrasound scanning probe microscopy.²⁵⁴ However, by increasing the mass of 2D resonators, such as by attaching proof-masses,²⁵⁸ it is possible to bring the resonances to a few kHz, which would make 2D vibration sensors useful for monitoring macroscopic systems such as industrial machines.

For acoustic sensors, Table II shows the characteristics of two types of devices: condenser microphones and fiber-coupled acoustic sensors. Condenser or electrostatic microphones share the same design principles of the electrostatic speakers shown in Figs. 14(c) and 14(d), but operate in the opposite way, converting ambient sounds into electrical signal based on changes of the gate capacitance.^{264,265} In fiber-coupled sensors, a 2D membrane is transferred to a ferrule attached to the tip of an optical fiber. Acoustic waves drive the membrane, and the motion is optically read by Fabry–Pérot interferometry of the reflected signal. Because of their design, the main application of condenser microphones is to transduce sounds in the audible range (hence the name microphone), whereas fiber-coupled sensors are typically designed to cover both audible and ultrasonic range and to operate in harsh environments, such as underwater or inside the body. Both types of sensors have similar mechanical response, with the acoustic

amplitude falling in the range of 0–100 Pa and BW of 0–0.8 MHz,²⁵⁶ while responsivity can be as high as 90 nm/Pa.²⁶³ In comparison, traditionally used materials in fiber-coupled sensors such as silica and silver have responsivity of ~ 10 –80 nm/kPa,^{269,270} whereas MEMS microphones typically have BW from audible frequencies up to 100 kHz and responsivity up to 3 nm/Pa.²⁶³ Thus, 2D materials show improvements of orders of magnitude. Because of their enhanced sensitivity, low manufacturing cost, and mechanical flexibility, 2D acoustic sensors can serve not only for sound capture but also as acoustic probes in situations ranging from well monitoring to bioimaging.

3. Other types of sensors

Most experimental papers reporting 2D NEMS-based sensors are focused on the previous two types of sensors. However, many other types of sensors are possible by measuring the response of 2D NEMS under different conditions. In general, there are three mechanisms of sensing an external variable through a resonator: either by monitoring its effect on the amplitude of motion, phase of motion, or in the resonant frequency. We will explore a selection of these sensor types, which are also summarized in Table II.

a. 2D NEMS bolometers. Bolometers are a class of sensor that transduces light into electricity by heating up a material, to measure small changes in electromagnetic radiation. The performance of a bolometer depends on the transduction speed and sensitivity, both of which are enhanced by decreasing the heat capacity of the system. Graphene is a promising candidate for nanomechanical bolometers due to its low heat capacity and high thermal stability. Figure 15(a) shows a schematic of a trampoline graphene nanomechanical bolometer (GNB) operating at room temperature.²⁶⁰ Unlike a conventional nanomechanical bolometer, which monitors deflection of a beam upon absorbed light, a graphene nanomechanical bolometer monitors the resonance frequency. Any absorption of light in GNB will induce an increase in temperature of the graphene membrane, causing thermal stress with shifting resonance frequency. Figure 15(b) plots the change in resonance frequency with respect to absorbed power obtained from a graphene-based bolometer. The GNB achieved a sensitivity of $2 \text{ pW}/\text{Hz}^{1/2}$, which is similar to the best-reported sensitivities at room temperature.^{278–281} In addition, utilizing the high thermal stability of graphene, GNB was tested for a high-temperature operation of $\sim 1213 \text{ K}$, where the device showed stable operation and no sign of damage. This makes the device very promising for harsh environment applications, such as in spaceships and exploration probes.

a. 2D NEMS accelerometers. Figure 15(c) shows a schematic drawing of an accelerometer formed by attaching a silicon proof mass to suspended graphene ribbons.²⁵⁸ Any change in acceleration forces triggers the displacement of proof mass leading to a change in strain of the suspended graphene ribbon, leading to a resistance change proportional to the actual acceleration. The corresponding sensing bandwidth and responsivity are displayed in Table II. Figure 15(d) shows the output voltage and change in resistance vs acceleration amplitude at 160 Hz. Assuming the same proof mass weight, the graphene-based accelerometer shows one order of magnitude higher change in resistance compared to other silicon-based piezoresistive accelerometers.^{275–278} In addition, the structure of

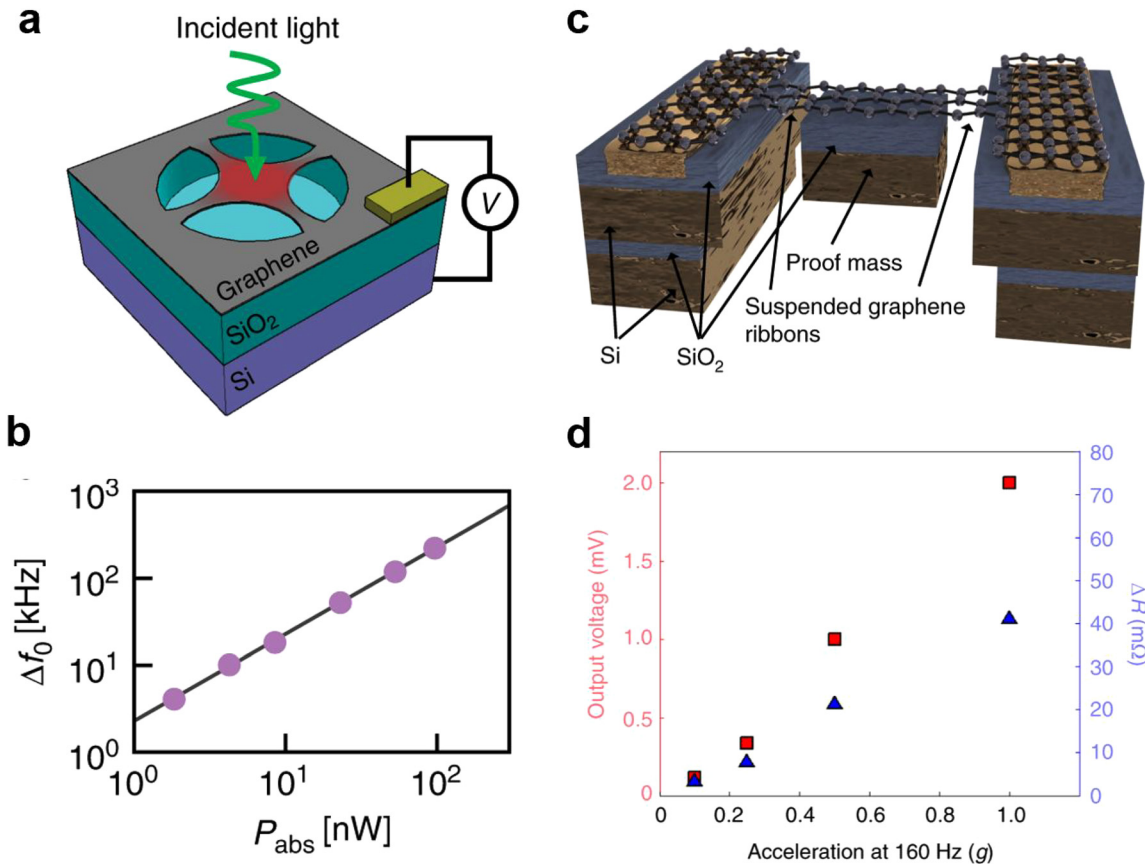


FIG. 15. Sensors from 2D NEMS. (a) Schematic of graphene-based bolometer.²⁶⁰ (b) Plot of resonance frequency change due to absorbed light. Solid line represents a fit to the data, producing 2.3 kHz nW^{-1} .²⁶⁰ (c) Schematic of an accelerometer based on suspended graphene nanoribbons with attached proof mass.²⁵⁸ (d) Output voltage (red) and change in resistance of graphene channel (blue) vs different accelerations at the graphene resonance frequency of 160 Hz.²⁵⁸ Panels (a) and (b): Reprinted with permission from Blaikie *et al.*, Nat. Commun. **10**(1), 4726 (2019). Copyright 2019 Authors, licensed under a Creative Commons Attribution Unported License. Panels (c) and (d): Reprinted with permission from Fan *et al.*, Nat. Electron. **2**(9), 394–404 (2019). Copyright 2019 Springer Nature Customer Service Center GmbH: Nature Electronics.

23 July 2023 15:16:56

graphene accelerometers has at least two orders of magnitude smaller area than silicon accelerometers.

b. 2D NEMS force sensors. Because of their high responsivity, 2D NEMS make excellent force sensors. However, the ultimate limit in force sensitivity at room temperature is determined by the thermal fluctuations and the sensitivity of any readout electronics. To create force sensors, graphene NEMS were coupled to a superconducting cavity as the gate, allowing very low sensitivity readout at low temperature.^{125,126,285} Any applied force produces a displacement of the membrane, which is read by monitoring the reflection coefficient of microwave photons from transmission lines to the superconducting cavity. The best force to displacement transduction will occur when the force is applied at the mechanical resonance frequency. At resonance, graphene force sensors reached sensitivities down to zetanewtons, comparable to carbon nanotube resonators.²⁸⁰ While these sensors can only operate in the sub-Kelvin regime, they have applicability in quantum sensing and transducing quantum states.

c. 2D NEMS mass sensors. MEMS-based mass sensors operate on the principle that any adsorbate shifts the resonant frequency. For a mass uniformly adsorbed on the area of a membrane, the ratio of the change in frequency is the same as the ratio of the adsorbed mass to the effective membrane mass as long as the stiffness of the adsorbed layer is zero. Since most applications of NEMS mass sensors are targeted for detecting very small amounts of gas or biochemical molecules, the zero-stiffness assumption is reasonable. The low effective masses of 2D NEMS make them excellent mass sensors compared with typical MEMS. Moreover, the high surface area of 2D membranes increases the number of adsorption events compared to other nanomaterials such as nanotubes. Experimentally, monolayer graphene NEMS showed mass sensitivities of $<900 \text{ zg}$ from adsorbed H₂ molecules.²⁵⁹ For these reasons, mass sensing is an exciting application of NEMS in applications like low concentration sensing of hazardous chemicals. However, a major challenge of MEMS-based mass sensors in general, especially in the cases of single molecule detection, is the frequency shift is very sensitive to the position of the molecular adsorption, and there is no selectivity of adsorption. Just like in any sensor, control of the selective binding

sites and their binding species are necessary for the technological feasibility of 2D NEMS mass sensors.

These examples exhibit that exceptional mechanical and electrical properties of 2D materials have shown great promise for becoming the next generation of sensors, exceeding the performance of commercially available state-of-the-art MEMS.

C. Probing material properties

The strong interaction between in-plane strain or deflection and material properties of 2D membranes enables new strategies to use 2D NEMS to probe and extract intrinsic material mechanical, thermal, and structural parameters. Additionally, 2D materials are able to host emergent quantum states, which have no analog in conventional MEMS yet are sensitive to strain or capacitance, or which will induce changes in stress in the membrane, enabling new methods for mechanical transduction of quantum states.

1. Mechanical properties

One obvious application of 2D NEMS is to extract the mechanical properties of the 2D materials by modeling their dynamical constants using continuum mechanics models followed by numerical fitting. For example, measuring the cubic spring constant of a graphene membrane yields a Young's modulus $E \sim 600$ GPa,²⁷ which is inside the range of E obtained with other techniques.¹⁸ As another example, resonators made with anisotropic 2D materials such as BP and As_2S_3 show resonant frequencies, which depend on the in-plane orientation of the anisotropic crystal structure with respect to the orientation of rectangular-shaped devices. This allows an estimate of the ratio between Young's modulus in different crystallographic directions, 2.5 for BP and 1.7 for As_2S_3 .^{33,34,53}

In addition to elastic properties, 2D NEMS are also well suited for studying the mechanics of interfaces by measuring the response of resonators using 2D heterostructures. For instance, phenomena such as soliton motion,²⁶ interlayer friction,¹⁶³ and adhesion⁶⁷ are relatable to dynamic properties of NEMS such as frequency tuning and dissipation. Extending this idea, a recent paper analyzed the interaction between a graphene resonator and its supporting substrate by measuring hysteresis loops in its frequency tuning curve caused by slip.²⁸¹

2. Thermal properties

2D NEMS probe the thermal conductivity and reveal the mechanisms of thermal transport of 2D materials by monitoring the change in membrane resonance frequency from a localized laser spot on the 2D membrane as a function of intensity and spot position, as well as substrate temperature. For example, Fig. 16(a) shows a resonant frequency map of a multi-layer black phosphorus membrane as a function of laser spot position.³⁵ Fitting the amount of strain change vs laser power and spot position with finite element models reveals that black phosphorus has anisotropic thermal conductivity with 3–4 times higher conductivity along the zigzag ($\sim 40 \text{ W m}^{-1} \text{ K}^{-1}$) vs armchair ($\sim 10 \text{ W m}^{-1} \text{ K}^{-1}$) directions. As another example, the temperature-dependent thermal conductance of monolayer MoSe_2 is mediated by diffusive phonon transport above 100 K and ballistic phonon transport for T below 100 K.⁵¹

In principle, other thermal properties like the coefficient of thermal expansion (CTE) could be inferred from the response of 2D NEMS or by correlating resonance properties with Raman spectroscopy. In practice, there is an enormous disagreement not just in the value but the sign of CTE of graphene.^{81,82,117,124,282} The reason for this disagreement is because of the nonlinear entropic fluctuations in 2D membranes discussed in the dissipation section (Sec. IV D). The magnitude of these fluctuations is tied to the size, stress, and temperature of the membrane. As such, they break the simple continuum mechanics models on which parameters like CTE are defined, and are more related to the entropic mechanics governing systems like free polymers.^{198–203} As a result, the value measured via one method (e.g., Raman peak shifts, rippling, resonant frequency tuning) or geometry (suspended or on surface, number of layers, clamping) cannot be easily extended to other systems. While adding complexity, this shows that there is still interesting physics to be understood governing the thermal and mechanical properties of materials in reduced dimensions.

3. Quantum phase transitions

When materials undergo quantum phase transitions, 2D NEMS allow us to probe the very small perturbations in strain or carrier density as changes in the frequency. This gives potential for 2D NEMS to probe or transduce a variety of quantum phenomena, from quantum hall states, to magnetic phases, to correlated electronic phases.

The strong coupling between the mechanics and electronic carrier density permits 2D NEMS to probe quantum states like the quantum Hall effect in graphene.^{88,283} Figure 16(b) shows the amplitude map of a graphene resonator for different frequencies and magnetic fields.⁸⁸ The frequencies show a saw-tooth like behavior as the magnetic field increases. The smooth frequency variation (between jumps) is due to the change in chemical potential of the graphene membrane within a Landau level [extracted and shown in right side of y axis in Fig. 16(b)]. The change in chemical potential modulates the electronic carrier density in the graphene and thus the electrostatic force on the membrane. This frequency shift is analogous to the capacitive softening discussed in Sec. IV B, except that now the capacitance is based on a finite rather than infinite density of states. The sudden frequency jumps are due to transition between Landau levels, causing discrete changes in the carrier density. The ability to directly measure chemical potentials without specialized tools is an advantage of the NEMS technique for studying Hall effect physics⁸⁸ and can be applied to other material systems to probe physics like the charge cores in flux vortices in superconducting membranes.⁷²

The last several years have brought a host of new magnetic 2D materials, which display layer-dependent paramagnetic, ferromagnetic, and antiferromagnetic phases. Figure 16(c) shows the resonant frequency (top) and magnetic circular dichroism (MCD, bottom) of a CrI_3 resonator as a function of external magnetic field.³⁸ The resonator consists of bilayer CrI_3 encapsulated between monolayer WSe_2 and few-layer graphene, used as the electrostatically active layer. Encapsulation prevented CrI_3 from air exposure. There are discrete and hysteretic jumps in the resonance frequency as a function of the applied magnetic field. These jumps are a result of an antiferromagnetic to ferromagnetic phase transition in the magnetic bilayer, where

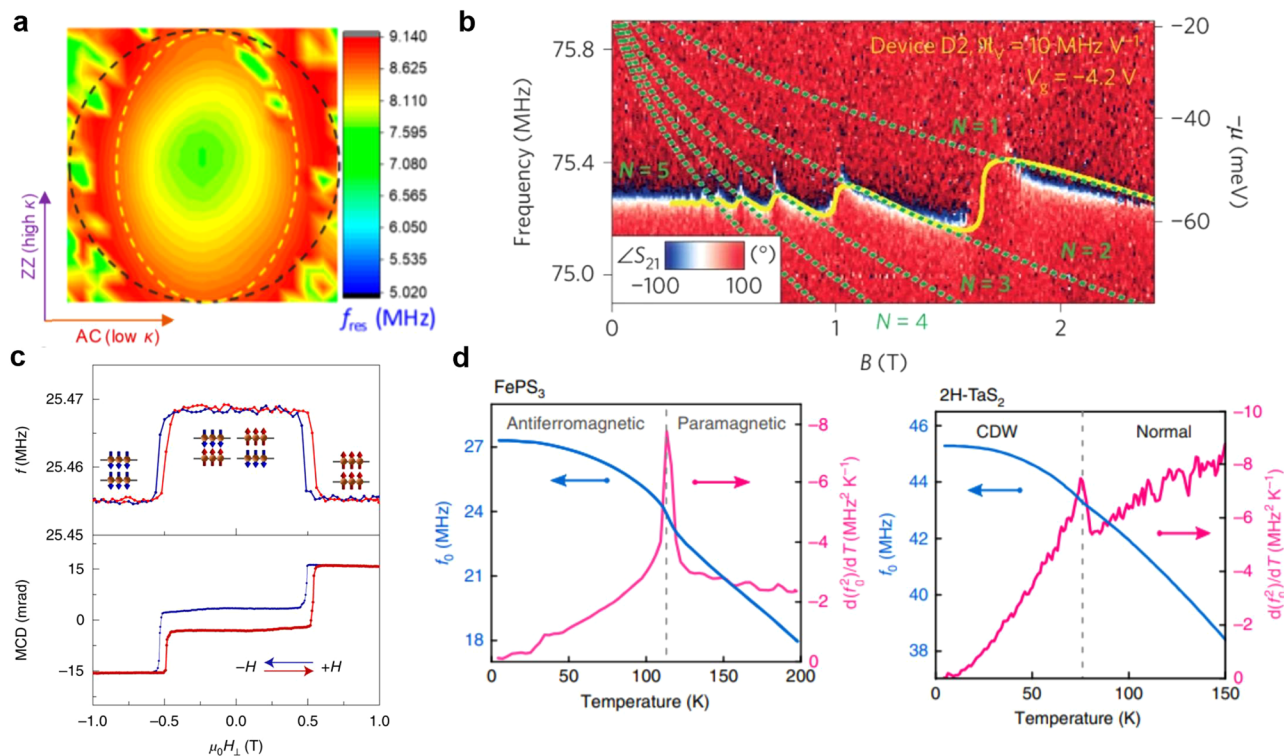


FIG. 16. Probing material and physical properties with 2D NEMS. (a) Resonant frequency mapping of a black phosphorus (BP) resonator as a function of the (x, y) coordinates of the excitation laser. The clamped edge of the resonator is shown by the dashed black line. The non-symmetric profile of the resonant frequency is a result of the different thermal conductivities of BP along its armchair (AC) and zigzag (ZZ) directions. Adapted with permission from Islam *et al.*, *Nano Lett.* **18**(12), 7683–7691 (2018). Copyright 2018 American Chemical Society.³⁵ (b) 2D map of phase vs frequency (chemical potential) and magnetic field (filling factor). The shift of frequency reveals the evolution of chemical potential (Yellow). Reprinted with permission from Chen *et al.*, “Modulation of mechanical resonance by chemical potential oscillation in graphene,” *Nat. Phys.* **12**(3), 240–244 (2016). Copyright 2016 Springer Nature Customer Service Center GmbH: Nature Nanotechnology.³⁸ (c) Resonant frequency (top) and MCD (bottom) vs applied magnetic field in bilayer CrI₃ resonator. Reprinted with permission from Jiang *et al.*, *Nat. Mater.* **19**(12), 1295–1299 (2020). Copyright 2020 Springer Nature Customer Service Center GmbH: Nature Materials.³⁸ (d) Resonant frequency vs temperature plots of FePS₃ (left) and TaS₂ resonators. The discontinuity in the second derivative of the frequency indicates a phase transition. Adapted with permission from Sijskens *et al.*, *Nat. Commun.* **11**(1), 2698 (2020). Copyright 2020 Authors, licensed under a Creative Commons Attribution Unported License.⁵⁹

23 July 2023 15:16:56

the antiferromagnetic phase corresponds with the two layers having opposite polarization and the ferromagnetic phase corresponds with the two layers having same polarization. When the magnetic field reaches ± 0.5 T, the aligned spin configuration becomes energetically favorable. The frequency shift is due to a magnetostrictive effect, causing a small change in strain between the two phases.

The last several years have also seen an explosion of 2D materials with complex correlated states. Many of these states only onset at low temperatures, and 2D NEMS may be used to probe those phase transitions as discrete changes in strain as a function of temperature.⁶¹ For example, Fig. 16(d) shows the resonant frequency for different temperatures of multilayer FePS₃ (left) and TaS₂ (right) resonators.⁵⁹ In both cases, discontinuities in the derivative of the square of the frequency (df_0^2/dT) are signatures of the phase transition. For FePS₃, the peak at 114 K represents an antiferromagnetic to paramagnetic phase transition, whereas for TaS₂, the peak at 77 K is a transition from a charge-density wave (CDW) to a disordered electronic phase. The phase transition induces a small change in lattice constants and the coefficient of thermal expansion, leading to a sudden change in the slope of the frequency vs temperature curve.⁵⁹

VII. PERSPECTIVES: CHALLENGES AND OPPORTUNITIES

In the sections above, we articulated how the discoveries of graphene and other 2D materials were a breakthrough in MEMS and NEMS, providing an easy route to access the nano- and sub-nanoscale regime with corresponding improvements in responsivity, transduction, tunability, and sensitivity. We have discussed the emerging applications and newly enabled fundamental scientific directions currently being explored. Next, we will discuss the key challenges of control and reproducibility that must be overcome for 2D NEMS to become a viable technology, and how these issues affect which applications are most likely to succeed first. Finally, we will speculate on some promising future frontiers that have not yet been realized.

A. Challenges

While 2D NEMS hold a great deal of potential, there are also important challenges in reproducibility, control, and scalable manufacturing that prevent their immediate incorporation as viable technologies. Many of the studies of 2D NEMS discussed above are of

hero devices, selected from many failures. Often systematic studies taken with the greatest care, including our own, show enormous device-to-device variation in frequency, dissipation, nonlinearity, and tunability of factors of 1–10 in magnitude on a single substrate. Some of these challenges are common to all 2D materials research, while some are specific to NEMS.

- Challenges common to all 2D materials. There are two broad challenges in scalability and control that are common to all 2D material applications: (1) scalable synthesis with deterministic control over material quality and uniformity and (2) scalable yet atomically precise fabrication processes. Regarding the scalable synthesis, there are several routes to produce 2D materials at wafer scales. However, at this stage, there is still not deterministic control over material quality, doping, or electronic mobility.²⁸⁴ Moreover, all processes must take into account detrimental effects from the environment, such as inhomogeneous doping from the substrate or atmosphere,^{8,285} as well as the air²⁸⁵ and water degradation of some 2D materials. Regarding the scalable fabrication processes, some of the notable challenges are scalable transfer methods to produce desired interfacial cleanliness and alignment;²⁸⁶ atomically precise fabrication methods for accessing individual layers within 2D heterostructures;⁴¹ and integration of new processes with traditional CMOS processes.^{287,288}
- Challenges specific to NEMS from 2D materials. In most MEMS technologies, one of the most difficult to control yet important parameters that determine the mechanical response is the film stress. Slight variations in processing conditions during thin-film deposition affect the stress in the film, and such variations must be taken into account in the system design and final calibration for any device. This challenge is aggravated in 2D materials because: (1) the very high responsivity of the membrane stiffness to stress and morphology combined with their low mass means even small deformations, such as wrinkles, as well as the smallest added mass from processing or atmospheric adsorption, will have dramatic effects on the mechanics. (2) Most methods of transferring 2D materials onto patterned substrates to make suspended membranes are not conducive to improved control of stress, since they rely on poorly controlled macroscale or capillary forces and adhesion mechanics.

Taken together, the current lack of predictive control cancels out many of the benefits in sensitivity, transduction, and responsivity for many technological applications, but is largely not a problem if not an opportunity for fundamental studies. The good news is most of these challenges are also crucial to many applications with nanomaterials, and a great deal of effort and funding is going into realizing nanoscale control. In the meantime, some applications are more robust against the inherent variability. For example, most applications based on sensing require careful calibration to make signals meaningful, and high device variability makes such calibration more difficult. In contrast, applications based on the tunability of 2D materials are less sensitive to variability because they intrinsically rely on dynamic control of the frequency over a wide range with an applied gate. Even more robust are applications that operate below the resonance frequency. For example, graphene-based acoustic devices are already being commercialized.^{289,290}

B. Frontiers and new opportunities

There is still much work to be done on improving control to incorporate existing 2D NEMS into technology, exploring the fundamental nonlinearity and entropic properties of atomic membranes, and to use 2D NEMS as a test bed to explore the properties of the more than 1000 currently predicted van der Waals materials, as well as other quasi-2D materials like complex oxides or superconducting materials.^{63,68–70,72} Moreover, mechanics could be used to transduce defects within the 2D materials, such as single-photon emitters made from hBN resonators.^{29,230,231} In addition to those examples, there are a few frontiers, which are ripe for new discoveries or which have been predicted but not yet realized.

- 2D membranes as structural elements in M/NEMS. There are many opportunities to utilize 2D membranes as mechanical elements. Early examples of this are seen in the accelerometers made from graphene supporting a silicon proof-mass²⁵⁸ and graphene membranes as a tunable coupler of two MEMS resonators.²⁰⁵ Extending this concept further, one can envision geometrically reconfigurable three-dimensional structures or metamaterials where graphene serves as springs, actuators, or hinges.^{291–295}
- 2D materials as active electronic and optoelectronic layers in M/NEMS. There are many opportunities that could leverage the diverse electronic and optoelectronic properties of 2D materials as active electronic materials, using mechanical waves to transduce the electronic properties or direct quasi particles. Examples in this direction are TMDC monolayers transferred onto surface acoustic wave (SAW) devices, which use strain waves to guide excitons in the 2D materials,^{296–299} or as the tunable membranes in acoustic waveguides.^{201,300} Using excitons or phonons as information carriers is promising for next-generation quantum technologies.³⁰¹
- Slippable M/NEMS with 2D superlubric interface. Many machines that work at the human scale become inoperable at the micro- and nanoscale because friction overwhelms other forces, putting limits on the size of systems like micromotors, microgears, sliding microactuators, and microswitches. The orders-of-magnitude lower friction resulting from the structural superlubricity in incommensurate 2D interfaces opens up new classes of NEMS based on slippable interfaces in 2D heterostructures. By applying lateral forces, it is possible to laterally slide and rotate 2D layers in heterostructures,¹⁶⁴ which could be utilized to actuate non-suspended MEMS on a surface. So far, such motion has only been demonstrated by pushing on heterostructures with AFM or STM tips.^{302–304} However, there have been several intriguing device concepts proposed, but not yet realized, based on lateral motion in electrostatically actuated heterostructures for low dissipation nanoswitches or nanogenerators.^{305–309}
- 2D NEMS as qubits. 2D NEMS are excellent candidates for qubits for quantum information. The high frequency of 2D resonators means they will reach the quantum limit (zero-point) of motion at comparatively high temperatures.³¹⁰ As a result, utilizing a combination of cryogenic and optomechanical or electronic back action, 2D membranes may be cooled to a few or single phonon occupation.^{279,311} In addition, the high-quality factor and low spring constant mean that there will be a large and

detectable amplitude of motion in the quantum limit of >1 pm, and a long coherence time.

- 2D NEMS for multi-domain quantum transduction. The properties of 2D materials allow easy multi-domain transduction by integrating the 2D membranes with superconducting and photonic resonators, coupling photons with microwave to optical energies with phonons in the quantum limit.^{125,126,279,312} Even more interesting, the low onset of nonlinearity in 2D membranes offers a unique opportunity to use 2D NEMS to host nonlinear quantum dynamical effects, which could be used to transduce between qubit states³¹⁰ and lead to non-Gaussian states.^{313,314}

Taken together, it has now been 15 years since the first graphene resonator was demonstrated. Since then, the field of 2D NEMS has undergone explosive growth, segmenting into several categories such as leveraging the favorable scaling for enhanced performance compared with existing MEMS technologies, to probing and coupling the properties of a diverse and growing class of materials to mechanics, and to fundamental studies of the nature of nonlinear and thermal mechanics in the atomic limit. As we look to the future, we are seeing new applications emerge, which are not just improved by 2D NEMS, but uniquely enabled by them, promising to make the next 15 years even more exciting than the last.

ACKNOWLEDGMENTS

The authors acknowledge support from NSF-CAREER Award No. CMMI-184673.

AUTHOR DECLARATIONS

Conflict of Interest

The authors have no conflicts to disclose.

Author Contributions

Paolo Furlanetto Ferrari: Conceptualization (equal); Investigation (equal); Writing – original draft (equal); Writing – review & editing (supporting). **Sunphil Kim:** Conceptualization (equal); Investigation (equal); Writing – original draft (equal); Writing – review & editing (supporting). **Arend Marcel van der Zande:** Conceptualization (equal); Funding acquisition (lead); Project administration (lead); Supervision (lead); Writing – original draft (supporting); Writing – review & editing (lead).

DATA AVAILABILITY

The data that support the findings of this study are available from the corresponding author upon reasonable request.

REFERENCES

- ¹H. G. Craighead, “Nanoelectromechanical systems,” *Science* **290**(5496), 1532–1535 (2000).
- ²K. L. Ekinci and M. L. Roukes, “Nanoelectromechanical systems,” *Rev. Sci. Instrum.* **76**(6), 061101 (2005).
- ³K. L. Ekinci, X. M. H. Huang, and M. L. Roukes, “Ultrasensitive nanoelectromechanical mass detection,” *Appl. Phys. Lett.* **84**(22), 4469–4471 (2004).
- ⁴J. A. Sidles, J. L. Garbini, K. J. Bruland, D. Rugar, O. Züger, S. Hoen, and C. S. Yannoni, “Magnetic resonance force microscopy,” *Rev. Mod. Phys.* **67**, 249–265 (1995).
- ⁵M. D. LaHaye, O. Buu, B. Camarota, and K. C. Schwab, “Approaching the quantum limit of a nanomechanical resonator,” *Science* **304**(5667), 74–77 (2004).
- ⁶M. Morita, T. Ohmi, E. Hasegawa, M. Kawakami, and M. Ohwada, “Growth of native oxide on a silicon surface,” *J. Appl. Phys.* **68**(3), 1272–1281 (1990).
- ⁷K. I. Bolotin, K. J. Sikes, Z. Jiang, M. Klima, G. Fudenberg, J. Hone, P. Kim, and H. L. Stormer, “Ultrahigh electron mobility in suspended graphene,” *Solid State Commun.* **146**(9), 351–355 (2008).
- ⁸L. Wang, I. Meric, P. Y. Huang, Q. Gao, Y. Gao, H. Tran, T. Taniguchi, K. Watanabe, L. M. Campos, D. A. Muller, J. Guo, P. Kim, J. Hone, K. L. Shepard, and C. R. Dean, “One-dimensional electrical contact to a two-dimensional material,” *Science* **342**(6158), 614–617 (2013).
- ⁹K. F. Mak, C. Lee, J. Hone, J. Shan, and T. F. Heinz, “Atomically thin mos₂: A new direct-gap semiconductor,” *Phys. Rev. Lett.* **105**, 136805 (2010).
- ¹⁰J. Cheng, C. Wang, X. Zou, and L. Liao, “Recent advances in optoelectronic devices based on 2D materials and their heterostructures,” *Adv. Opt. Mater.* **7**(1), 1800441 (2019).
- ¹¹R. R. Nair, P. Blake, A. N. Grigorenko, K. S. Novoselov, T. J. Booth, T. Stauber, N. M. R. Peres, and A. K. Geim, “Fine structure constant defines visual transparency of graphene,” *Science* **320**(5881), 1308–1308 (2008).
- ¹²B. L. Evans, P. A. Young, and R. W. Ditchburn, “Optical absorption and dispersion in molybdenum disulphide,” *Proc. R. Soc. A* **284**(1398), 402–422 (1965).
- ¹³C. Lee, X. Wei, J. W. Kysar, and J. Hone, “Measurement of the elastic properties and intrinsic strength of monolayer graphene,” *Science* **321**(5887), 385–388 (2008).
- ¹⁴E. Han, J. Yu, E. Annevelink, J. Son, D. A. Kang, K. Watanabe, T. Taniguchi, E. Ertekin, P. Y. Huang, and A. M. van der Zande, “Ultrasoft slip-mediated bending in few-layer graphene,” *Nat. Mater.* **19**, 305–309 (2019).
- ¹⁵G. Wang, Z. Dai, J. Xiao, S. Feng, C. Weng, L. Liu, Z. Xu, R. Huang, and Z. Zhang, “Bending of multilayer van der Waals materials,” *Phys. Rev. Lett.* **123**, 116101 (2019).
- ¹⁶J. Yu, E. Han, M. A. Hossain, K. Watanabe, T. Taniguchi, E. Ertekin, A. M. van der Zande, and P. Y. Huang, “Designing the bending stiffness of 2D material heterostructures,” *Adv. Mater.* **33**(9), 2007269 (2021).
- ¹⁷D. Akinwande, C. J. Brennan, J. S. Bunch, P. Egberts, J. R. Felts, H. Gao, R. Huang, J.-S. Kim, T. Li, Y. Li, K. M. Liechti, N. Lu, H. S. Park, E. J. Reed, P. Wang, B. I. Yakobson, T. Zhang, Y.-W. Zhang, Y. Zhou, and Y. Zhu, “A review on mechanics and mechanical properties of 2D materials—Graphene and beyond,” *Extreme Mech. Lett.* **13**, 42–77 (2017).
- ¹⁸A. Castellanos-Gomez, V. Singh, H. S. J. van der Zant, and G. A. Steele, “Mechanics of freely-suspended ultrathin layered materials,” *Ann. Phys.* **527**(1–2), 27–44 (2015).
- ¹⁹C. Androulidakis, K. Zhang, M. Robertson, and S. Tawfick, “Tailoring the mechanical properties of 2D materials and heterostructures,” *2D Mater.* **5**(3), 032005 (2018).
- ²⁰R. Frisenda, E. Navarro-Moratalla, P. Gant, D. Pérez De Lara, P. Jarillo-Herrero, R. V. Gorbachev, and A. Castellanos-Gomez, “Recent progress in the assembly of nanodevices and van der Waals heterostructures by deterministic placement of 2D materials,” *Chem. Soc. Rev.* **47**, 53–68 (2018).
- ²¹R. A. Barton, J. Parpia, and H. G. Craighead, “Fabrication and performance of graphene nanoelectromechanical systems,” *J. Vac. Sci. Technol. B* **29**(5), 050801 (2011).
- ²²C. Chen and J. Hone, “Graphene nanoelectromechanical systems,” *Proc. IEEE* **101**(7), 1766–1779 (2013).
- ²³Z. H. Khan, A. R. Kermany, A. Öchsner, and F. Iacopi, “Mechanical and electromechanical properties of graphene and their potential application in MEMS,” *J. Phys. D* **50**(5), 053003 (2017).
- ²⁴J. S. Bunch, “Putting a damper on nanoresonators,” *Nat. Nanotechnol.* **6**(6), 331–332 (2011).
- ²⁵A. M. van der Zande, R. A. Barton, J. S. Alden, C. S. Ruiz-Vargas, W. S. Whitney, P. H. Q. Pham, J. Park, J. M. Parpia, H. G. Craighead, and P. L. McEuen, “Large-scale arrays of single-layer graphene resonators,” *Nano Lett.* **10**(12), 4869–4873 (2010).
- ²⁶S. Kim, E. Annevelink, E. Han, J. Yu, P. Y. Huang, E. Ertekin, and A. M. van der Zande, “Stochastic stress jumps due to soliton dynamics in two-dimensional van der Waals interfaces,” *Nano Lett.* **20**(2), 1201–1207 (2020).

- ²⁷D. Davidovikj, F. Alijani, S. J. Cartamil-Bueno, H. S. J. van der Zant, M. Amabili, and P. G. Steeneken, "Nonlinear dynamic characterization of two-dimensional materials," *Nat. Commun.* **8**(1), 1253 (2017).
- ²⁸J. P. Mathew, R. N. Patel, A. Borah, R. Vijay, and M. M. Deshmukh, "Dynamical strong coupling and parametric amplification of mechanical modes of graphene drums," *Nat. Nanotechnol.* **11**, 747 (2016).
- ²⁹X. Gao, Z.-Q. Yin, and T. Li, "High-speed quantum transducer with a single-photon emitter in a 2D resonator," *Ann. Phys.* **532**(10), 2000233 (2020).
- ³⁰J. S. Bunch, A. M. van der Zande, S. S. Verbridge, I. W. Frank, D. M. Tanenbaum, J. M. Parpia, H. G. Craighead, and P. L. McEuen, "Electromechanical resonators from graphene sheets," *Science* **315**(5811), 490–493 (2007).
- ³¹K. S. Novoselov, A. K. Geim, S. V. Morozov, D. Jiang, Y. Zhang, S. V. Dubonos, I. V. Grigorieva, and A. A. Firsov, "Electric field effect in atomically thin carbon films," *Science* **306**(5696), 666–669 (2004).
- ³²B. Xu, P. Zhang, J. Zhu, Z. Liu, A. Eichler, X.-Q. Zheng, J. Lee, A. Dash, S. More, S. Wu, Y. Wang, H. Jia, A. Naik, A. Bachtold, R. Yang, P. X.-L. Feng, and Z. Wang, "Nanomechanical resonators: Toward atomic scale," *ACS Nano* **16**(10), 15545–15585 (2022).
- ³³Z. Wang and P. X.-L. Feng, "Design of black phosphorus 2D nanomechanical resonators by exploiting the intrinsic mechanical anisotropy," *2D Mater.* **2**(2), 021001 (2015).
- ³⁴Z. Wang, H. Jia, X.-Q. Zheng, R. Yang, G. J. Ye, X. H. Chen, and P. X.-L. Feng, "Resolving and tuning mechanical anisotropy in black phosphorus via nanomechanical multimode resonance spectromicroscopy," *Nano Lett.* **16**(9), 5394–5400 (2016).
- ³⁵A. Islam, A. van den Akker, and P. X. L. Feng, "Anisotropic thermal conductivity of suspended black phosphorus probed by opto-thermomechanical resonance spectromicroscopy," *Nano Lett.* **18**(12), 7683–7691 (2018).
- ³⁶A. Raja, L. Waldecker, J. Zipfel, Y. Cho, S. Brem, J. D. Ziegler, M. Kulig, T. Taniguchi, K. Watanabe, E. Malic, T. F. Heinz, T. C. Berkelbach, and A. Chernikov, "Dielectric disorder in two-dimensional materials," *Nat. Nanotechnol.* **14**(9), 832–837 (2019).
- ³⁷B. Huang, G. Clark, E. Navarro-Moratalla, D. R. Klein, R. Cheng, K. L. Seyler, D. Zhong, E. Schmidgall, M. A. McGuire, D. H. Cobden, W. Yao, D. Xiao, P. Jarillo-Herrero, and X. Xu, "Layer-dependent ferromagnetism in a van der Waals crystal down to the monolayer limit," *Nature* **546**(7657), 270–273 (2017).
- ³⁸S. Jiang, H. Xie, J. Shan, and K. F. Mak, "Exchange magnetostriction in two-dimensional antiferromagnets," *Nat. Mater.* **19**(12), 1295–1299 (2020).
- ³⁹S. Shivaraman, R. A. Barton, X. Yu, J. Alden, L. Herman, M. V. S. Chandrasekhar, J. Park, P. L. McEuen, J. M. Parpia, H. G. Craighead, and M. G. Spencer, "Free-standing epitaxial graphene," *Nano Lett.* **9**(9), 3100–3105 (2009).
- ⁴⁰J. T. Robinson, M. Zalalutdinov, J. W. Baldwin, E. S. Snow, Z. Wei, P. Sheehan, and B. H. Houston, "Wafer-scale reduced graphene oxide films for nanomechanical devices," *Nano Lett.* **8**(10), 3441–3445 (2008).
- ⁴¹J. Son, J. Kwon, S. Kim, Y. Lv, J. Yu, J.-Y. Lee, H. Ryu, K. Watanabe, T. Taniguchi, R. Garrido-Menacho, N. Mason, E. Ertekin, P. Y. Huang, G.-H. Lee, and A. M. van der Zande, "Atomically precise graphene etch stops for three dimensional integrated systems from two dimensional material heterostructures," *Nat. Commun.* **9**(1), 3988 (2018).
- ⁴²J. Lee, Z. Wang, K. He, J. Shan, and P. X. L. Feng, "High frequency MoS₂ nanomechanical resonators," *ACS Nano* **7**(7), 6086–6091 (2013).
- ⁴³J. Lee, Z. Wang, K. He, R. Yang, J. Shan, and P. X.-L. Feng, "Electrically tunable single- and few-layer MoS₂ nanoelectromechanical systems with broad dynamic range," *Sci. Adv.* **4**(3), eaao6653 (2018).
- ⁴⁴A. Castellanos-Gomez, R. van Leeuwen, M. Buscema, H. S. J. van der Zant, G. A. Steele, and W. J. Venstra, "Single-layer MoS₂ mechanical resonators," *Adv. Mater.* **25**(46), 6719–6723 (2013).
- ⁴⁵S. Manzeli, D. Dumcenco, G. Migliato Marega, and A. Kis, "Self-sensing, tunable monolayer MoS₂ nanoelectromechanical resonators," *Nat. Commun.* **10**(1), 4831 (2019).
- ⁴⁶C. Samanta, N. Arora, V. Kranthi Kumar, S. Raghavan, and A. K. Naik, "The effect of strain on effective duffing nonlinearity in the CVD-MoS₂ resonator," *Nanoscale* **11**, 8394–8401 (2019).
- ⁴⁷C. Samanta, P. R. Yasasvi Gangavarapu, and A. K. Naik, "Nonlinear mode coupling and internal resonances in MoS₂ nanoelectromechanical system," *Appl. Phys. Lett.* **107**(17), 173110 (2015).
- ⁴⁸B. R. Matis, B. H. Houston, and J. W. Baldwin, "Energy dissipation pathways in few-layer MoS₂ nanoelectromechanical systems," *Sci. Rep.* **7**(1), 5656–5656 (2017).
- ⁴⁹P. Prasad, N. Arora, and A. K. Naik, "Parametric amplification in MoS₂ drum resonator," *Nanoscale* **9**, 18299–18304 (2017).
- ⁵⁰N. Morell, A. Reserbat-Plantey, I. Tsoutsios, K. G. Schädler, F. Dubin, F. H. L. Koppens, and A. Bachtold, "High quality factor mechanical resonators based on WS₂ monolayers," *Nano Lett.* **16**(8), 5102–5108 (2016).
- ⁵¹N. Morell, S. Tepsic, A. Reserbat-Plantey, A. Cepellotti, M. Manca, I. Epstein, A. Isacsson, X. Marie, F. Mauri, and A. Bachtold, "Optomechanical measurement of thermal transport in two-dimensional MoSe₂ lattices," *Nano Lett.* **19**(5), 3143–3150 (2019).
- ⁵²J. Lee, F. Ye, Z. Wang, R. Yang, J. Hu, Z. Mao, J. Wei, and P. X.-L. Feng, "Single- and few-layer WTe₂ and their suspended nanostructures: Raman signatures and nanomechanical resonances," *Nanoscale* **8**, 7854–7860 (2016).
- ⁵³M. Šiškins, M. Lee, F. Alijani, M. R. van Blankenstein, D. Davidovikj, H. S. J. van der Zant, and P. G. Steeneken, "Highly anisotropic mechanical and optical properties of 2D layered As₂S₃ membranes," *ACS Nano* **13**(9), 10845–10851 (2019).
- ⁵⁴X.-Q. Zheng, J. Lee, and P. X. L. Feng, "Hexagonal boron nitride nanomechanical resonators with spatially visualized motion," *Microsyst. Nanoeng.* **3**(1), 17038 (2017).
- ⁵⁵S. J. Cartamil-Bueno, M. Cavalieri, R. Wang, S. Houri, S. Hofmann, and H. S. J. van der Zant, "Mechanical characterization and cleaning of CVD single-layer h-BN resonators," *npj 2D Mater. Appl.* **1**(1), 16 (2017).
- ⁵⁶P. K. Shandilya, J. E. Fröch, M. Mitchell, D. P. Lake, S. Kim, M. Toth, B. Behera, C. Healey, I. Aharonovich, and P. E. Barclay, "Hexagonal boron nitride cavity optomechanics," *Nano Lett.* **19**(2), 1343–1350 (2019).
- ⁵⁷S. J. Cartamil-Bueno, P. G. Steeneken, F. D. Tichelaar, E. Navarro-Moratalla, W. J. Venstra, R. van Leeuwen, E. Coronado, H. S. J. van der Zant, G. A. Steele, and A. Castellanos-Gomez, "High-quality-factor tantalum oxide nanomechanical resonators by laser oxidation of TaSe₂," *Nano Res.* **8**(9), 2842–2849 (2015).
- ⁵⁸B. Xu, J. Zhu, F. Xiao, N. Liu, Y. Liang, C. Jiao, J. Li, Q. Deng, S. Wu, T. Wen, S. Pei, H. Wan, X. Xiao, J. Xia, and Z. Wang, "Electrically tunable mxene nanomechanical resonators vibrating at very high frequencies," *ACS Nano* **16**(12), 20229–20237 (2022).
- ⁵⁹M. Šiškins, M. Lee, S. Mañas-Valero, E. Coronado, Y. M. Blanter, H. S. J. van der Zant, and P. G. Steeneken, "Magnetic and electronic phase transitions probed by nanomechanical resonators," *Nat. Commun.* **11**(1), 2698 (2020).
- ⁶⁰M. Šiškins, S. Kurdi, M. Lee, B. J. M. Slotboom, W. Xing, S. Mañas-Valero, E. Coronado, S. Jia, W. Han, T. van der Sar, H. S. J. van der Zant, and P. G. Steeneken, "Nanomechanical probing and strain tuning of the curie temperature in suspended cr₂ge₂te₆-based heterostructures," *npj 2D Mater. Appl.* **6**(1), 41 (2022).
- ⁶¹S. Sengupta, H. S. Solanki, V. Singh, S. Dhara, and M. M. Deshmukh, "Electromechanical resonators as probes of the charge density wave transition at the nanoscale in nbse₂," *Phys. Rev. B* **82**, 155432 (2010).
- ⁶²M. Will, M. Hamer, M. Müller, A. Noury, P. Weber, A. Bachtold, R. V. Gorbachev, C. Stampfer, and J. Güttinger, "High quality factor graphene-based two-dimensional heterostructure mechanical resonator," *Nano Lett.* **17**(10), 5950–5955 (2017).
- ⁶³M. Lee, M. Šiškins, S. Mañas-Valero, E. Coronado, P. G. Steeneken, and H. S. J. van der Zant, "Study of charge density waves in suspended 2H-TaS₂ and 2H-TaSe₂ by nanomechanical resonance," *Appl. Phys. Lett.* **118**(19), 193105 (2021).
- ⁶⁴S. Kim, J. Yu, and A. M. van der Zande, "Nano-electromechanical drumhead resonators from two-dimensional material bimorphs," *Nano Lett.* **18**(11), 6686–6695 (2018).
- ⁶⁵F. Ye, J. Lee, and P. X.-L. Feng, "Atomic layer MoS₂-graphene van der Waals heterostructure nanomechanical resonators," *Nanoscale* **9**, 18208–18215 (2017).
- ⁶⁶R. Kumar, D. W. Session, R. Tsuchikawa, M. Homer, H. Paas, K. Watanabe, T. Taniguchi, and V. V. Deshpande, "Circular electromechanical resonators based on hexagonal-boron nitride-graphene heterostructures," *Appl. Phys. Lett.* **117**(18), 183103 (2020).

- ⁶⁷L. D. Varma Sangani, S. Mandal, S. Ghosh, K. Watanabe, T. Taniguchi, and M. M. Deshmukh, "Dynamics of interfacial bubble controls adhesion mechanics in van der Waals heterostructure," *Nano Lett.* **22**(9), 3612–3619 (2022).
- ⁶⁸D. Davidovikj, D. J. Groenendijk, A. M. R. V. L. Monteiro, A. Dijkhoff, D. Afanasyev, M. Šiškins, M. Lee, Y. Huang, E. van Heumen, H. S. J. van der Zant, A. D. Caviglia, and P. G. Steeneken, "Ultrathin complex oxide nanomechanical resonators," *Commun. Phys.* **3**(1), 163 (2020).
- ⁶⁹V. Harbola, S. Crossley, S. S. Hong, D. Lu, Y. A. Birkholzer, Y. Hikita, and H. Y. Hwang, "Strain gradient elasticity in SrTiO₃ membranes: Bending versus stretching," *Nano Lett.* **21**(6), 2470–2475 (2021).
- ⁷⁰M. Lee, M. P. Robin, R. H. Guis, U. Filippozzi, D. H. Shin, T. C. van Thiel, S. P. Paardekooper, J. R. Renshof, H. S. J. van der Zant, A. D. Caviglia, G. J. Verbiest, and P. G. Steeneken, "Self-sealing complex oxide resonators," *Nano Lett.* **22**(4), 1475–1482 (2022).
- ⁷¹S. K. Sahu, J. Vaidya, F. Schmidt, D. Jangade, A. Thamizhavel, G. Steele, M. M. Deshmukh, and V. Singh, "Nanoelectromechanical resonators from high- T_c superconducting crystals of Bi₂Sr₂Ca₁Cu₂O_{8+δ}," *2D Mater.* **6**(2), 025027 (2019).
- ⁷²S. K. Sahu, S. Mandal, S. Ghosh, M. M. Deshmukh, and V. Singh, "Superconducting vortex-charge measurement using cavity electromechanics," *Nano Lett.* **22**(4), 1665–1671 (2022).
- ⁷³W. Bao, F. Miao, Z. Chen, H. Zhang, W. Jang, C. Dames, and C. N. Lau, "Controlled ripple texturing of suspended graphene and ultrathin graphite membranes," *Nat. Nanotechnol.* **4**(9), 562–566 (2009).
- ⁷⁴S. Deng and V. Berry, "Wrinkled, rippled and crumpled graphene: An overview of formation mechanism, electronic properties, and applications," *Mater. Today* **19**(4), 197–212 (2016).
- ⁷⁵E. Cerda and L. Mahadevan, "Geometry and physics of wrinkling," *Phys. Rev. Lett.* **90**, 074302 (2003).
- ⁷⁶D. Garcia-Sanchez, A. M. van der Zande, A. S. Paulo, B. Lassagne, P. L. McEuen, and A. Bachtold, "Imaging mechanical vibrations in suspended graphene sheets," *Nano Lett.* **8**(5), 1399–1403 (2008).
- ⁷⁷D. Davidovikj, J. J. Slim, S. J. Cartamil-Bueno, H. S. J. van der Zant, P. G. Steeneken, and W. J. Venstra, "Visualizing the motion of graphene nanodrums," *Nano Lett.* **16**(4), 2768–2773 (2016).
- ⁷⁸J. S. Bunch, S. S. Verbridge, J. S. Alden, A. M. van der Zande, J. M. Parpia, H. G. Craighead, and P. L. McEuen, "Impermeable atomic membranes from graphene sheets," *Nano Lett.* **8**(8), 2458–2462 (2008).
- ⁷⁹R. A. Barton, I. R. Storch, V. P. Adiga, R. Sakakibara, B. R. Cipriany, B. Ilic, S. P. Wang, P. Ong, P. L. McEuen, J. M. Parpia, and H. G. Craighead, "Photothermal self-oscillation and laser cooling of graphene optomechanical systems," *Nano Lett.* **12**(9), 4681–4686 (2012).
- ⁸⁰R. De Alba, F. Massel, I. R. Storch, T. S. Abhilash, A. Hui, P. L. McEuen, H. G. Craighead, and J. M. Parpia, "Tunable phonon-cavity coupling in graphene membranes," *Nat. Nanotechnol.* **11**(9), 741–746 (2016).
- ⁸¹I. R. Storch, R. De Alba, V. P. Adiga, T. S. Abhilash, R. A. Barton, H. G. Craighead, J. M. Parpia, and P. L. McEuen, "Young's modulus and thermal expansion of tensioned graphene membranes," *Phys. Rev. B* **98**, 085408 (2018).
- ⁸²R. De Alba, T. S. Abhilash, A. Hui, I. R. Storch, H. G. Craighead, and J. M. Parpia, "Temperature-dependence of stress and elasticity in wet-transferred graphene membranes," *J. Appl. Phys.* **123**(9), 095109 (2018).
- ⁸³C.-H. Liu, I. S. Kim, and L. J. Lauhon, "Optical control of mechanical mode-coupling within a Mo₂ resonator in the strong-coupling regime," *Nano Lett.* **15**(10), 6727–6731 (2015).
- ⁸⁴S. P. Koenig, N. G. Boddeti, M. L. Dunn, and J. S. Bunch, "Ultrastrong adhesion of graphene membranes," *Nat. Nanotechnol.* **6**(9), 543–546 (2011).
- ⁸⁵C. Chen, S. Rosenblatt, K. I. Bolotin, W. Kalb, P. Kim, I. Kymissis, H. L. Stormer, T. F. Heinz, and J. Hone, "Performance of monolayer graphene nanomechanical resonators with electrical readout," *Nat. Nanotechnol.* **4**(12), 861–867 (2009).
- ⁸⁶D. Davidovikj, M. Poot, S. J. Cartamil-Bueno, H. S. J. van der Zant, and P. G. Steeneken, "On-chip heaters for tension tuning of graphene nanodrums," *Nano Lett.* **18**(5), 2852–2858 (2018).
- ⁸⁷Y. Xie, J. Lee, Y. Wang, and P. X.-L. Feng, "Straining and tuning atomic layer nanoelectromechanical resonators via comb-drive MEMS actuators," *Adv. Mater. Technol.* **6**(2), 2000794 (2021).
- ⁸⁸C. Chen, V. V. Deshpande, M. Koshino, S. Lee, A. Gondarenko, A. H. MacDonald, P. Kim, and J. Hone, "Modulation of mechanical resonance by chemical potential oscillation in graphene," *Nat. Phys.* **12**(3), 240–244 (2016).
- ⁸⁹E. Stolyarova, D. Stolyarov, K. Bolotin, S. Ryu, L. Liu, K. T. Rim, M. Klime, M. Hybertsen, I. Pogorelsky, I. Pavlishin, K. Kusche, J. Hone, P. Kim, H. L. Stormer, V. Yakimenko, and G. Flynn, "Observation of graphene bubbles and effective mass transport under graphene films," *Nano Lett.* **9**(1), 332–337 (2009).
- ⁹⁰R. A. Barton, B. Ilic, A. M. van der Zande, W. S. Whitney, P. L. McEuen, J. M. Parpia, and H. G. Craighead, "High, size-dependent quality factor in an array of graphene mechanical resonators," *Nano Lett.* **11**(3), 1232–1236 (2011).
- ⁹¹H. Jia, R. Yang, A. E. Nguyen, S. N. Alvillar, T. Empante, L. Bartels, and P. X.-L. Feng, "Large-scale arrays of single- and few-layer Mo₂ nanomechanical resonators," *Nanoscale* **8**, 10677–10685 (2016).
- ⁹²Z. Wang and P. X. L. Feng, "Interferometric motion detection in atomic layer 2D nanostructures: Visualizing signal transduction efficiency and optimization pathways," *Sci. Rep.* **6**, 28923 (2016).
- ⁹³Y. Ben-Shimon and A. Ya'akovovitz, "Magnetic excitation and dissipation of multilayer two-dimensional resonators," *Appl. Phys. Lett.* **118**(6), 063103 (2021).
- ⁹⁴V. Sazonova, Y. Yaish, H. Üstünel, D. Roundy, T. A. Arias, and P. L. McEuen, "A tunable carbon nanotube electromechanical oscillator," *Nature* **431**, 284 (2004).
- ⁹⁵Y. Xu, C. Chen, V. V. Deshpande, F. A. DiRenno, A. Gondarenko, D. B. Heinz, S. Liu, P. Kim, and J. Hone, "Radio frequency electrical transduction of graphene mechanical resonators," *Appl. Phys. Lett.* **97**(24), 243111 (2010).
- ⁹⁶C. Chen, S. Lee, V. V. Deshpande, G.-H. Lee, M. Lekas, K. Shepard, and J. Hone, "Graphene mechanical oscillators with tunable frequency," *Nat. Nanotechnol.* **8**(12), 923–927 (2013).
- ⁹⁷S. Lee, C. Chen, V. V. Deshpande, G.-H. Lee, I. Lee, M. Lekas, A. Gondarenko, Y.-J. Yu, K. Shepard, P. Kim, and J. Hone, "Electrically integrated SU-8 clamped graphene drum resonators for strain engineering," *Appl. Phys. Lett.* **102**(15), 153101 (2013).
- ⁹⁸V. Gouttenoire, T. Barois, S. Perisanu, J.-L. Leclercq, S. T. Purcell, P. Vincent, and A. Ayari, "Digital and FM demodulation of a doubly clamped single-walled carbon-nanotube oscillator: Towards a nanotube cell phone," *Small* **6**(9), 1060–1065 (2010).
- ⁹⁹B. Lassagne, Y. Tarakanov, J. Kinaret, D. Garcia-Sanchez, and A. Bachtold, "Coupling mechanics to charge transport in carbon nanotube mechanical resonators," *Science* **325**(5944), 1107–1110 (2009).
- ¹⁰⁰G. A. Steele, A. K. Hüttel, B. Witkamp, M. Poot, H. B. Meerwaldt, L. P. Kouwenhoven, and H. S. J. van der Zant, "Strong coupling between single-electron tunneling and nanomechanical motion," *Science* **325**(5944), 1103–1107 (2009).
- ¹⁰¹H. Zhu, Y. Wang, J. Xiao, M. Liu, S. Xiong, Z. J. Wong, Z. Ye, Y. Ye, X. Yin, and X. Zhang, "Observation of piezoelectricity in free-standing monolayer Mo₂," *Nat. Nanotechnol.* **10**(2), 151–155 (2015).
- ¹⁰²S. Tadigadapa and K. Mateti, "Piezoelectric MEMS sensors: State-of-the-art and perspectives," *Meas. Sci. Technol.* **20**(9), 092001 (2009).
- ¹⁰³H. Liu, J. Zhong, C. Lee, S.-W. Lee, and L. Lin, "A comprehensive review on piezoelectric energy harvesting technology: Materials, mechanisms, and applications," *Appl. Phys. Rev.* **5**(4), 041306 (2018).
- ¹⁰⁴K.-A. N. Duerloo, M. T. Ong, and E. J. Reed, "Intrinsic piezoelectricity in two-dimensional materials," *J. Phys. Chem. Lett.* **3**(19), 2871–2876 (2012).
- ¹⁰⁵Y. Zhou, W. Liu, X. Huang, A. Zhang, Y. Zhang, and Z. L. Wang, "Theoretical study on two-dimensional Mo₂ piezoelectric nanogenerators," *Nano Res.* **9**(3), 800–807 (2016).
- ¹⁰⁶G. Pillai and S.-S. Li, "Piezoelectric MEMS resonators: A review," *IEEE Sens. J.* **21**(11), 12589–12605 (2021).
- ¹⁰⁷Z. Qian, F. Liu, Y. Hui, S. Kar, and M. Rinaldi, "Graphene as a massless electrode for ultrahigh-frequency piezoelectric nanoelectromechanical systems," *Nano Lett.* **15**(7), 4599–4604 (2015).
- ¹⁰⁸L. Khine, J. B. W. Soon, and J. M. Tsai, "Piezoelectric ALN MEMS resonators with high coupling coefficient," in *2011 16th International Solid-State Sensors, Actuators and Microsystems Conference*, Beijing, China, 5–9 June 2011 (IEEE, 2011), pp. 526–529.

- ¹⁰⁹R. Lu, Y. Yang, S. Link, and S. Gong, "Al resonators in 128° Y-cut lithium niobate with electromechanical coupling of 46.4%," *J. Microelectromech. Syst.* **29**(3), 313–319 (2020).
- ¹¹⁰Y. Liu, J. Guo, E. Zhu, L. Liao, S.-J. Lee, M. Ding, I. Shakir, V. Gambin, Y. Huang, and X. Duan, "Approaching the Schottky-Mott limit in van der Waals metal-semiconductor junctions," *Nature* **557**(7707), 696–700 (May 2018).
- ¹¹¹R. M. Cole, G. A. Brawley, V. P. Adiga, R. De Alba, J. M. Parpia, B. Illic, H. G. Craighead, and W. P. Bowen, "Evanescent-field optical readout of graphene mechanical motion at room temperature," *Phys. Rev. Appl.* **3**, 024004 (2015).
- ¹¹²A. W. Barnard, M. Zhang, G. S. Wiederhecker, M. Lipson, and P. L. McEuen, "Real-time vibrations of a carbon nanotube," *Nature* **566**(7742), 89–93 (2019).
- ¹¹³J. Zhu, L. Wang, J. Wu, Y. Liang, F. Xiao, B. Xu, Z. Zhang, X. Fan, Y. Zhou, J. Xia, and Z. Wang, "Achieving 1.2 fm/Hz^{1/2} displacement sensitivity with laser interferometry in two-dimensional nanomechanical resonators: Pathways towards quantum-noise-limited measurement at room temperature," *Chin. Phys. Lett.* **40**(3), 038102 (2023).
- ¹¹⁴M. Amabili, *Nonlinear Mechanics of Shells and Plates in Composite, Soft and Biological Materials* (Cambridge University Press, 2018).
- ¹¹⁵V. Kaajakari, *Practical MEMS* (Small Gear Publications, Las Vegas, Nevada, 2009).
- ¹¹⁶T. Wah, "Vibration of circular plates," *J. Acoust. Soc. Am.* **34**(3), 275–281 (1962).
- ¹¹⁷R. J. Nicholl, H. J. Conley, N. V. Lavrik, I. Vlassiuk, Y. S. Puzyrev, V. P. Sreenivas, S. T. Pantelides, and K. I. Bolotin, "The effect of intrinsic crumpling on the mechanics of free-standing graphene," *Nat. Commun.* **6**(1), 8789 (2015).
- ¹¹⁸Z. Wang, J. Lee, K. He, J. Shan, and P. X.-L. Feng, "Embracing structural nonidealities and asymmetries in two-dimensional nanomechanical resonators," *Sci. Rep.* **4**(1), 3919 (2014).
- ¹¹⁹E. Kramer, J. van Dorp, R. van Leeuwen, and W. J. Venstra, "Strain-dependent damping in nanomechanical resonators from thin MoS₂ crystals," *Appl. Phys. Lett.* **107**(9), 091903 (2015).
- ¹²⁰S. Afyouni Akbari, V. Ghafarinia, T. Larsen, M. M. Parmar, and L. G. Villanueva, "Large suspended monolayer and bilayer graphene membranes with diameter up to 750 μm," *Sci. Rep.* **10**(1), 6426 (2020).
- ¹²¹J. Zhu, B. Xu, F. Xiao, Y. Liang, C. Jiao, J. Li, Q. Deng, S. Wu, T. Wen, S. Pei, J. Xia, and Z. Wang, "Frequency scaling, elastic transition, and broad-range frequency tuning in WSe₂ nanomechanical resonators," *Nano Lett.* **22**(13), 5107–5113 (2022).
- ¹²²M. C. Lemme, S. Wagner, K. Lee, X. Fan, G. J. Verbiest, S. Wittmann, S. Lukas, R. J. Dolleman, F. Niklaus, H. S. J. van der Zant, G. S. Duesberg, and P. G. Steeneken, "Nanoelectromechanical sensors based on suspended 2D materials," *Research* **2020**, 8748602.
- ¹²³M. Šiskins, E. Sokolovskaya, M. Lee, S. Mañas-Valero, D. Davidovikj, H. S. J. van der Zant, and P. G. Steeneken, "Tunable strong coupling of mechanical resonance between spatially separated FePS₃ nanodrums," *Nano Lett.* **22**(1), 36–42 (2022).
- ¹²⁴V. Singh, S. Sengupta, H. S. Solanki, R. Dhall, A. Allain, S. Dhara, P. Pant, and M. M. Deshmukh, "Probing thermal expansion of graphene and modal dispersion at low-temperature using graphene nanoelectromechanical systems resonators," *Nanotechnology* **21**(16), 165204 (2010).
- ¹²⁵P. Weber, J. Güttinger, I. Tsoutsios, D. E. Chang, and A. Bachtold, "Coupling graphene mechanical resonators to superconducting microwave cavities," *Nano Lett.* **14**(5), 2854–2860 (2014).
- ¹²⁶V. Singh, S. J. Bosman, B. H. Schneider, Y. M. Blanter, A. Castellanos-Gómez, and G. A. Steele, "Optomechanical coupling between a multilayer graphene mechanical resonator and a superconducting microwave cavity," *Nat. Nanotechnol.* **9**(10), 820–824 (2014).
- ¹²⁷F. Ye, J. Lee, and P. X. L. Feng, "Electrothermally tunable graphene resonators operating at very high temperature up to 1200 K," *Nano Lett.* **18**(3), 1678–1685 (2018).
- ¹²⁸J. Lee, Z. Wang, K. He, J. Shan, and P. X.-L. Feng, "Air damping of atomically thin MoS₂ nanomechanical resonators," *Appl. Phys. Lett.* **105**(2), 023104 (2014).
- ¹²⁹M. Lee, D. Davidovikj, B. Sajadi, M. Šiskins, F. Alijani, H. S. J. van der Zant, and P. G. Steeneken, "Sealing graphene nanodrums," *Nano Lett.* **19**(8), 5313–5318 (2019).
- ¹³⁰R. J. Dolleman, D. Davidovikj, S. J. Cartamil-Bueno, H. S. J. van der Zant, and P. G. Steeneken, "Graphene squeeze-film pressure sensors," *Nano Lett.* **16**(1), 568–571 (2016).
- ¹³¹R. J. Dolleman, D. Chakraborty, D. R. Ladiges, H. S. J. van der Zant, J. E. Sader, and P. G. Steeneken, "Squeeze-film effect on atomically thin resonators in the high-pressure limit," *Nano Lett.* **21**(18), 7617–7624 (2021).
- ¹³²R. J. Dolleman, P. Belardinelli, S. Houri, H. S. J. van der Zant, F. Alijani, and P. G. Steeneken, "High-frequency stochastic switching of graphene resonators near room temperature," *Nano Lett.* **19**(2), 1282–1288 (2019).
- ¹³³A. Eichler, J. Moser, J. Chaste, M. Zdrojek, I. Wilson-Rae, and A. Bachtold, "Nonlinear damping in mechanical resonators made from carbon nanotubes and graphene," *Nat. Nanotechnol.* **6**(6), 339–342 (2011).
- ¹³⁴R. Lifshitz and M. C. Cross, *Nonlinear Dynamics of Nanomechanical and Micromechanical Resonators* (John Wiley & Sons, Ltd, 2009), Chap. 1, pp. 1–52.
- ¹³⁵H. W. C. Postma, I. Kozinsky, A. Husain, and M. L. Roukes, "Dynamic range of nanotube- and nanowire-based electromechanical systems," *Appl. Phys. Lett.* **86**(22), 223105 (2005).
- ¹³⁶Q. Lu and R. Huang, "Nonlinear mechanics of single-atomic-layer graphene sheets," *Int. J. Appl. Mech.* **01**(03), 443–467 (2009).
- ¹³⁷R. J. Dolleman, D. Davidovikj, H. S. J. van der Zant, and P. G. Steeneken, "Amplitude calibration of 2D mechanical resonators by nonlinear optical transduction," *Appl. Phys. Lett.* **111**(25), 253104 (2017).
- ¹³⁸P. Weber, J. Güttinger, A. Noury, J. Vergara-Cruz, and A. Bachtold, "Force sensitivity of multilayer graphene optomechanical devices," *Nat. Commun.* **7**, 12496 (2016).
- ¹³⁹J. Zhu, P. Zhang, R. Yang, and Z. Wang, "Analyzing electrostatic modulation of signal transduction efficiency in MoS₂ nanoelectromechanical resonators with interferometric readout," *Sci. China Inf. Sci.* **65**(2), 122409 (2022).
- ¹⁴⁰Z. Wang and P. X.-L. Feng, "Dynamic range of atomically thin vibrating nanomechanical resonators," *Appl. Phys. Lett.* **104**(10), 103109 (2014).
- ¹⁴¹M. Kumar and H. Bhaskaran, "Ultrasensitive room-temperature piezoresistive transduction in graphene-based nanoelectromechanical systems," *Nano Lett.* **15**(4), 2562–2567 (2015).
- ¹⁴²M. H. Matheny, L. G. Villanueva, R. B. Karabalin, J. E. Sader, and M. L. Roukes, "Nonlinear mode-coupling in nanomechanical systems," *Nano Lett.* **13**(4), 1622–1626 (2013).
- ¹⁴³L. G. Villanueva, R. B. Karabalin, M. H. Matheny, E. Kenig, M. C. Cross, and M. L. Roukes, "A nanoscale parametric feedback oscillator," *Nano Lett.* **11**(11), 5054–5059 (2011).
- ¹⁴⁴X. L. Feng, C. J. White, A. Hajimiri, and M. L. Roukes, "A self-sustaining ultrahigh-frequency nanoelectromechanical oscillator," *Nat. Nanotechnol.* **3**(6), 342–346 (2008).
- ¹⁴⁵C.-H. Song and K.-A. Wen, "Integration design of wide-dynamic-range MEMS magnetometer and oscillator," in *2018 IEEE International Conference on Semiconductor Electronics (ICSE)*, Kuala Lumpur, Malaysia, 15–17 August 2018 (IEEE, 2018), pp. 17–20.
- ¹⁴⁶K. Azgin, T. Akin, and L. Valdevit, "Ultrahigh-dynamic-range resonant MEMS load cells for micromechanical test frames," *J. Microelectromech. Syst.* **21**(6), 1519–1529 (2012).
- ¹⁴⁷I. Kozinsky, H. W. C. Postma, I. Bargatin, and M. L. Roukes, "Tuning nonlinearity, dynamic range, and frequency of nanomechanical resonators," *Appl. Phys. Lett.* **88**(25), 253101 (2006).
- ¹⁴⁸C. Samanta, N. Arora, and A. K. Naik, "Tuning of geometric nonlinearity in ultrathin nanoelectromechanical systems," *Appl. Phys. Lett.* **113**(11), 113101 (2018).
- ¹⁴⁹A. H. Nayfeh and D. T. Mook, *Nonlinear Oscillations* (John Wiley & Sons, Ltd, 2007).
- ¹⁵⁰X. Song, M. Oksanen, M. A. Sillanpää, H. G. Craighead, J. M. Parpia, and P. J. Hakonen, "Stamp transferred suspended graphene mechanical resonators for radio frequency electrical readout," *Nano Lett.* **12**(1), 198–202 (2012).
- ¹⁵¹W. J. Venstra, H. J. R. Westra, and H. S. J. van der Zant, "Stochastic switching of cantilever motion," *Nat. Commun.* **4**(1), 2624 (2013).
- ¹⁵²S. Mitatha, K. Dejhan, P. P. Yupapin, and N. Pornsuwancharoen, "Chaotic signal generation and coding using a nonlinear micro ring resonator," *Optik* **121**(1), 120–125 (2010).

- ¹⁵³V. B. Braginsky, V. P. Mitrofanov, and V. I. Panov, *Systems with Small Dissipation* (University of Chicago Press, 1985).
- ¹⁵⁴G. Anetsberger, O. Arcizet, Q. P. Unterreithmeier, R. Rivière, A. Schliesser, E. M. Weig, J. P. Kotthaus, and T. J. Kippenberg, "Near-field cavity optomechanics with nanomechanical oscillators," *Nat. Phys.* **5**(12), 909–914 (2009).
- ¹⁵⁵J. T. M. van Beek and R. Puers, "A review of MEMS oscillators for frequency reference and timing applications," *J. Micromech. Microeng.* **22**(1), 013001 (2011).
- ¹⁵⁶S. Ghaffari, S. A. Chandorkar, S. Wang, E. J. Ng, C. H. Ahn, V. Hong, Y. Yang, and T. W. Kenny, "Quantum limit of quality factor in silicon micro and nano mechanical resonators," *Sci. Rep.* **3**(1), 3244 (2013).
- ¹⁵⁷T. Bagci, A. Simonsen, S. Schmid, L. G. Villanueva, E. Zeuthen, J. Appel, J. M. Taylor, A. Sørensen, K. Usami, A. Schliesser, and E. S. Polzik, "Optical detection of radio waves through a nanomechanical transducer," *Nature* **507**(7490), 81–85 (2014).
- ¹⁵⁸M. Fischeneder, M. Oposich, M. Schneider, and U. Schmid, "Tunable Q-factor of MEMS cantilevers with integrated piezoelectric thin films," *Sensors* **18**(11), 3842 (2018).
- ¹⁵⁹Y. Deimerly, P. Rey, P. Robert, T. Bourouina, and G. Jourdan, "Electromechanical damping in MEMS accelerometers: A way towards single chip gyrometer accelerometer co-integration," in *2014 IEEE 27th International Conference on Micro Electro Mechanical Systems (MEMS)*, San Francisco, CA, 26–30 January 2014 (IEEE, 2014), pp. 725–728.
- ¹⁶⁰S. S. Verbridge, H. G. Craighead, and J. M. Parpia, "A megahertz nanomechanical resonator with room temperature quality factor over a million," *Appl. Phys. Lett.* **92**(1), 013112 (2008).
- ¹⁶¹B. M. Zwickl, W. E. Shanks, A. M. Jayich, C. Yang, A. C. Bleszynski Jayich, J. D. Thompson, and J. G. E. Harris, "High quality mechanical and optical properties of commercial silicon nitride membranes," *Appl. Phys. Lett.* **92**(10), 103125 (2008).
- ¹⁶²J.-W. Jiang, H. S. Park, and T. Rabczuk, "MoS₂ nanoresonators: Intrinsically better than graphene?", *Nanoscale* **6**, 3618–3625 (2014).
- ¹⁶³P. F. Ferrari, S. Kim, and A. M. van der Zande, "Dissipation from interlayer friction in graphene nanoelectromechanical resonators," *Nano Lett.* **21**(19), 8058–8065 (2021).
- ¹⁶⁴E. Koren, E. Lörtscher, C. Rawlings, A. W. Knoll, and U. Duerig, "Adhesion and friction in mesoscopic graphite contacts," *Science* **348**(6235), 679–683 (2015).
- ¹⁶⁵M. Takamura, H. Okamoto, K. Furukawa, H. Yamaguchi, and H. Hibino, "Energy dissipation in graphene mechanical resonators with and without free edges," *Micromachines* **7**(9), 158 (2016).
- ¹⁶⁶M. Dienwiebel, G. S. Verhoeven, N. Pradeep, J. W. M. Frenken, J. A. Heimberg, and H. W. Zandbergen, "Superlubricity of graphite," *Phys. Rev. Lett.* **92**, 126101 (2004).
- ¹⁶⁷Z. Liu, J. Yang, F. Grey, J. Z. Liu, Y. Liu, Y. Wang, Y. Yang, Y. Cheng, and Q. Zheng, "Observation of microscale superlubricity in graphite," *Phys. Rev. Lett.* **108**, 205503 (2012).
- ¹⁶⁸C. Androulidakis, E. N. Koukaras, G. Paterakis, G. Trakakis, and C. Galiotis, "Tunable macroscale structural superlubricity in two-layer graphene via strain engineering," *Nat. Commun.* **11**(1), 1595 (2020).
- ¹⁶⁹C. W. de Silva, *Vibration and Shock Handbook. Mechanical and Aerospace Engineering Series* (CRC Press, 2005).
- ¹⁷⁰S. Y. Kim and H. S. Park, "Multilayer friction and attachment effects on energy dissipation in graphene nanoresonators," *Appl. Phys. Lett.* **94**(10), 101918 (2009).
- ¹⁷¹R. Liu and L. Wang, "Nonlinear forced vibration of bilayer van der Waals materials drum resonator," *J. Appl. Phys.* **128**(14), 145105 (2020).
- ¹⁷²C. Seoáñez, F. Guinea, and A. H. Castro Neto, "Dissipation in graphene and nanotube resonators," *Phys. Rev. B* **76**, 125427 (2007).
- ¹⁷³M. Imboden and P. Mohanty, "Dissipation in nanoelectromechanical systems," *Phys. Rep.* **534**(3), 89–146 (2014).
- ¹⁷⁴M. Takamura, H. Okamoto, K. Furukawa, H. Yamaguchi, and H. Hibino, "Energy dissipation in edged and edgeless graphene mechanical resonators," *J. Appl. Phys.* **116**(6), 064304 (2014).
- ¹⁷⁵T. Miao, S. Yeom, P. Wang, B. Standley, and M. Bockrath, "Graphene nanoelectromechanical systems as stochastic-frequency oscillators," *Nano Lett.* **14**(6), 2982–2987 (2014).
- ¹⁷⁶S. Y. Kim and H. S. Park, "The importance of edge effects on the intrinsic loss mechanisms of graphene nanoresonators," *Nano Lett.* **9**(3), 969–974 (2009).
- ¹⁷⁷J.-W. Jiang and J.-S. Wang, "Why edge effects are important on the intrinsic loss mechanisms of graphene nanoresonators," *J. Appl. Phys.* **111**(5), 054314 (2012).
- ¹⁷⁸A. K. Hüttel, G. A. Steele, B. Witkamp, M. Poot, L. P. Kouwenhoven, and H. S. J. van der Zant, "Carbon nanotubes as ultrahigh quality factor mechanical resonators," *Nano Lett.* **9**(7), 2547–2552 (2009).
- ¹⁷⁹V. A. Sazonova, *A Tunable Carbon Nanotube Resonator* (Cornell University, 2006).
- ¹⁸⁰J. Güttinger, A. Noury, P. Weber, A. M. Eriksson, C. Lagoin, J. Moser, C. Eichler, A. Wallraff, A. Isacsson, and A. Bachtold, "Energy-dependent path of dissipation in nanomechanical resonators," *Nat. Nanotechnol.* **12**(7), 631–636 (2017).
- ¹⁸¹D. Midtvedt, A. Croy, A. Isacsson, Z. Qi, and H. S. Park, "Fermi-Pasta-Ulam physics with nanomechanical graphene resonators: Intrinsic relaxation and thermalization from flexural mode coupling," *Phys. Rev. Lett.* **112**, 145503 (2014).
- ¹⁸²P. Zhang, Y. Jia, M. Xie, Z. Liu, S. Shen, J. Wei, and R. Yang, "Strain-modulated dissipation in two-dimensional molybdenum disulfide nanoelectromechanical resonators," *ACS Nano* **16**(2), 2261–2270 (2022).
- ¹⁸³Y. Oshidari, T. Hatakeyama, R. Kometani, S. Warisawa, and S. Ishihara, "High quality factor graphene resonator fabrication using resist shrinkage-induced strain," *Appl. Phys. Express* **5**(11), 117201 (2012).
- ¹⁸⁴R. Lifshitz, "Phonon-mediated dissipation in micro- and nano-mechanical systems," *Physica B* **316–317**, 397–399 (2002).
- ¹⁸⁵V. P. Adiga, B. Ilic, R. A. Barton, I. Wilson-Rae, H. G. Craighead, and J. M. Parpia, "Approaching intrinsic performance in ultra-thin silicon nitride drum resonators," *J. Appl. Phys.* **112**(6), 064323 (2012).
- ¹⁸⁶A. Bachtold, J. Moser, and M. I. Dykman, "Mesoscopic physics of nanomechanical systems," *Rev. Mod. Phys.* **94**, 045005 (2022).
- ¹⁸⁷A. Croy, D. Midtvedt, A. Isacsson, and J. M. Kinaret, "Nonlinear damping in graphene resonators," *Phys. Rev. B* **86**, 235435 (2012).
- ¹⁸⁸S. De, K. Kunal, and N. R. Aluru, "Nonlinear intrinsic dissipation in single layer MoS₂ resonators," *RSC Adv.* **7**, 6403–6410 (2017).
- ¹⁸⁹S. De, A. van der Zande, and N. R. Aluru, "Intrinsic dissipation due to mode coupling in two-dimensional-material resonators revealed through a multi-scale approach," *Phys. Rev. Appl.* **14**, 034062 (2020).
- ¹⁹⁰A. M. Eriksson, D. Midtvedt, A. Croy, and A. Isacsson, "Frequency tuning, nonlinearities and mode coupling in circular mechanical graphene resonators," *Nanotechnology* **24**(39), 395702 (2013).
- ¹⁹¹W. Gao and R. Huang, "Thermomechanics of monolayer graphene: Rippling, thermal expansion and elasticity," *J. Mech. Phys. Solids* **66**, 42–58 (2014).
- ¹⁹²H. Liu, M. Lee, M. Sijskins, H. S. J. van der Zant, P. G. Steeneken, and G. J. Verbiest, "Tension tuning of sound and heat transport in graphene," *arXiv:2204.06877* (2022).
- ¹⁹³P. L. de Andres, F. Guinea, and M. I. Katsnelson, "Bending modes, anharmonic effects, and thermal expansion coefficient in single-layer and multilayer graphene," *Phys. Rev. B* **86**, 144103 (2012).
- ¹⁹⁴M. I. Katsnelson and A. Fasolino, "Graphene as a prototype crystalline membrane," *Acc. Chem. Res.* **46**(1), 97–105 (2013).
- ¹⁹⁵A. Košmrlj and D. R. Nelson, "Response of thermalized ribbons to pulling and bending," *Phys. Rev. B* **93**, 125431 (2016).
- ¹⁹⁶J. H. Los, A. Fasolino, and M. I. Katsnelson, "Scaling behavior and strain dependence of in-plane elastic properties of graphene," *Phys. Rev. Lett.* **116**, 015901 (2016).
- ¹⁹⁷M. J. Bowick, A. Košmrlj, D. R. Nelson, and R. Sknepnek, "Non-hookean statistical mechanics of clamped graphene ribbons," *Phys. Rev. B* **95**, 104109 (2017).
- ¹⁹⁸A. Morshedifar, M. Ruiz-García, M. J. Abdolhosseini Qomi, and A. Košmrlj, "Buckling of thermalized elastic sheets," *J. Mech. Phys. Solids* **149**, 104296 (2021).
- ¹⁹⁹P. Prasad, N. Arora, and A. K. Naik, "Gate tunable cooperativity between vibrational modes," *Nano Lett.* **19**(9), 5862–5867 (2019).
- ²⁰⁰Z.-Z. Zhang, X.-X. Song, G. Luo, Z.-J. Su, K.-L. Wang, G. Cao, H.-O. Li, M. Xiao, G.-C. Guo, L. Tian, G.-W. Deng, and G.-P. Guo, "Coherent phonon

- dynamics in spatially-separated graphene mechanical resonators," *Proc. Natl. Acad. Sci. U. S. A.* **117**(11), 5582–5587 (2020).
- ²⁰¹Y. Wang, J. Lee, X.-Q. Zheng, Y. Xie, and P. X.-L. Feng, "Hexagonal boron nitride phononic crystal waveguides," *ACS Photonics* **6**(12), 3225–3232 (2019).
- ²⁰²J. N. Kirchhoff, K. Weinel, S. Heeg, V. Deinhart, S. Kovalchuk, K. Höflich, and K. I. Bolotin, "Tunable graphene phononic crystal," *Nano Lett.* **21**(5), 2174–2182 (2021).
- ²⁰³H. Xie, S. Jiang, D. A. Rhodes, J. C. Hone, J. Shan, and K. F. Mak, "Tunable exciton-optomechanical coupling in suspended monolayer MoSe₂," *Nano Lett.* **21**(6), 2538–2543 (2021).
- ²⁰⁴H.-K. Li, K. Y. Fong, H. Zhu, Q. Li, S. Wang, S. Yang, Y. Wang, and X. Zhang, "Valley optomechanics in a monolayer semiconductor," *Nat. Photonics* **13**(6), 397–401 (2019).
- ²⁰⁵G. J. Verbiest, M. Goldsche, J. Sonntag, T. Khodkov, N. von den Driesch, D. Buca, and C. Stampfer, "Tunable coupling of two mechanical resonators by a graphene membrane," *2D Mater.* **8**(3), 035039 (2021).
- ²⁰⁶R. Singh, A. Sarkar, C. Guria, R. J. T. Nicholl, S. Chakraborty, K. I. Bolotin, and S. Ghosh, "Giant tunable mechanical nonlinearity in graphene-silicon nitride hybrid resonator," *Nano Lett.* **20**(6), 4659–4666 (2020).
- ²⁰⁷I. Mahboob, V. Nier, K. Nishiguchi, A. Fujiwara, and H. Yamaguchi, "Multi-mode parametric coupling in an electromechanical resonator," *Appl. Phys. Lett.* **103**(15), 153105 (2013).
- ²⁰⁸A. A. Clerk, K. W. Lehnert, P. Bertet, J. R. Petta, and Y. Nakamura, "Hybrid quantum systems with circuit quantum electrodynamics," *Nat. Phys.* **16**(3), 257–267 (2020).
- ²⁰⁹D. Antonio, D. H. Zanette, and D. López, "Frequency stabilization in nonlinear micromechanical oscillators," *Nat. Commun.* **3**(1), 806 (2012).
- ²¹⁰A. Z. Hajjaj, M. A. Hafiz, and M. I. Younis, "Mode coupling and nonlinear resonances of MEMS arch resonators for bandpass filters," *Sci. Rep.* **7**(1), 41820 (2017).
- ²¹¹M. Spletzer, A. Raman, A. Q. Wu, X. Xu, and R. Reifenberger, "Ultrasensitive mass sensing using mode localization in coupled microcantilevers," *Appl. Phys. Lett.* **88**(25), 254102 (2006).
- ²¹²K. Asadi, J. Yu, and H. Cho, "Nonlinear couplings and energy transfers in micro- and nano-mechanical resonators: Intermodal coupling, internal resonance and synchronization," *Philos. Trans. R. Soc., A* **376**(2127), 20170141 (2018).
- ²¹³S. Shiva, P. Nathamgari, S. Dong, L. Medina, N. Moldovan, D. Rosenmann, R. Divan, D. Lopez, L. J. Lauhon, and H. D. Espinosa, "Nonlinear mode coupling and one-to-one internal resonances in a monolayer WS₂ nanoresonator," *Nano Lett.* **19**(6), 4052–4059 (2019).
- ²¹⁴A. Chiout, F. Correia, M.-Q. Zhao, A. T. C. Johnson, D. Pierucci, F. Oehler, A. Ouerghi, and J. Chaste, "Multi-order phononic frequency comb generation within a MoS₂ electromechanical resonator," *Appl. Phys. Lett.* **119**(17), 173102 (2021).
- ²¹⁵P. G. Steeneken, R. J. Dolleman, D. Davidovikj, F. Aljani, and H. S. J. van der Zant, "Dynamics of 2D material membranes," *2D Mater.* **8**(4), 042001 (2021).
- ²¹⁶H. Okamoto, A. Gourgout, C.-Y. Chang, K. Onomitsu, I. Mahboob, E. Y. Chang, and H. Yamaguchi, "Coherent phonon manipulation in coupled mechanical resonators," *Nat. Phys.* **9**(8), 480–484 (2013).
- ²¹⁷D. Kleckner and D. Bouwmeester, "Sub-kelvin optical cooling of a micromechanical resonator," *Nature* **444**(7115), 75–78 (2006).
- ²¹⁸A. Reserbat-Plantey, L. Marty, O. Arcizet, N. Bendib, and V. Bouchiat, "A local optical probe for measuring motion and stress in a nanoelectromechanical system," *Nat. Nanotechnol.* **7**(3), 151–155 (2012).
- ²¹⁹X. Zhang, K. Makles, L. Colombier, D. Metten, H. Majjad, P. Verlot, and S. Berciaud, "Dynamically-enhanced strain in atomically thin resonators," *Nat. Commun.* **11**(1), 5526 (2020).
- ²²⁰R. Yang, S. M. E. H. Yousuf, J. Lee, P. Zhang, Z. Liu, and P. X.-L. Feng, "Raman spectroscopic probe for nonlinear MoS₂ nanoelectromechanical resonators," *Nano Lett.* **22**(14), 5780–5787 (2022).
- ²²¹G. Luo, Z.-Z. Zhang, G.-W. Deng, H.-O. Li, G. Cao, M. Xiao, G.-C. Guo, L. Tian, and G.-P. Guo, "Strong indirect coupling between graphene-based mechanical resonators via a phonon cavity," *Nat. Commun.* **9**, 383 (2018).
- ²²²Z.-Z. Zhang, X.-X. Song, G. Luo, Z.-J. Su, K.-L. Wang, G. Cao, H.-O. Li, M. Xiao, G.-C. Guo, L. Tian, G.-W. Deng, and G.-P. Guo, "Coherent phonon dynamics in spatially separated graphene mechanical resonators," *Proc. Natl. Acad. Sci. U. S. A.* **117**(11), 5582–5587 (2020).
- ²²³H. M. Ouakad, S. Ilyas, and M. I. Younis, "Investigating mode localization at lower- and higher-order modes in mechanically coupled MEMS resonators," *J. Comput. Nonlinear Dyn.* **15**(3), 031001 (2020).
- ²²⁴T. Rabenimanana, V. Walter, N. Kacem, P. Le Moal, G. Bourbon, and J. Lardiès, "Mass sensor using mode localization in two weakly coupled MEMS cantilevers with different lengths: Design and experimental model validation," *Sens. Actuators, A* **295**, 643–652 (2019).
- ²²⁵D. Hatanaka, I. Mahboob, K. Onomitsu, and H. Yamaguchi, "Phonon waveguides for electromechanical circuits," *Nat. Nanotechnol.* **9**(7), 520–524 (2014).
- ²²⁶J. Cha and C. Daraio, "Electrical tuning of elastic wave propagation in nanomechanical lattices at MHz frequencies," *Nat. Nanotechnol.* **13**(11), 1016–1020 (2018).
- ²²⁷S. Kim, J. Bunyan, P. F. Ferrari, A. Kanj, A. F. Vakakis, A. M. van der Zande, and S. Tawfick, "Buckling-mediated phase transitions in nano-electromechanical phononic waveguides," *Nano Lett.* **21**(15), 6416–6424 (2021).
- ²²⁸A. D. O'Connell, M. Hofheinz, M. Ansmann, R. C. Bialczak, M. Lenander, E. Lucero, M. Neeley, D. Sank, H. Wang, M. Weides, J. Wenner, J. M. Martinis, and A. N. Cleland, "Quantum ground state and single-phonon control of a mechanical resonator," *Nature* **464**(7289), 697–703 (2010).
- ²²⁹M. Aspelmeyer, T. J. Kippenberg, and F. Marquardt, "Cavity optomechanics," *Rev. Mod. Phys.* **86**, 1391–1452 (2014).
- ²³⁰M. Abdi, M.-J. Hwang, M. Aghtar, and M. B. Plenio, "Spin-mechanical scheme with color centers in hexagonal boron nitride membranes," *Phys. Rev. Lett.* **119**, 233602 (2017).
- ²³¹M. Abdi and M. B. Plenio, "Quantum effects in a mechanically modulated single-photon emitter," *Phys. Rev. Lett.* **122**, 023602 (2019).
- ²³²S. Huang, L. Liang, X. Ling, A. A. Puretzky, D. B. Geohegan, B. G. Sumpter, J. Kong, V. Meunier, and M. S. Dresselhaus, "Low-frequency interlayer Raman modes to probe interface of twisted bilayer MoS₂," *Nano Lett.* **16**(2), 1435–1444 (2016).
- ²³³S. Lee, V. P. Adiga, R. A. Barton, A. M. van der Zande, G.-H. Lee, B. Rob Ilic, A. Gondarenko, J. M. Parpia, H. G. Craighead, and J. Hone, "Graphene metalization of high-stress silicon nitride resonators for electrical integration," *Nano Lett.* **13**(9), 4275–4279 (2013).
- ²³⁴L. Sekaric, D. W. Carr, S. Evoy, J. M. Parpia, and H. G. Craighead, "Nanomechanical resonant structures in silicon nitride: Fabrication, operation and dissipation issues," *Sens. Actuators, A* **101**(1), 215–219 (2002).
- ²³⁵R. Singh, R. J. Nicholl, K. I. Bolotin, and S. Ghosh, "Motion transduction with thermo-mechanically squeezed graphene resonator modes," *Nano Lett.* **18**(11), 6719–6724 (2018).
- ²³⁶C. Schwarz, B. Pigeau, L. Mercier de Lépinay, A. G. Kuhn, D. Kalita, N. Bendib, L. Marty, V. Bouchiat, and O. Arcizet, "Deviation from the normal mode expansion in a coupled graphene-nanomechanical system," *Phys. Rev. Appl.* **6**, 064021 (2016).
- ²³⁷R. Singh, A. Sarkar, C. Guria, R. J. Nicholl, S. Chakraborty, K. I. Bolotin, and S. Ghosh, "Giant tunable mechanical nonlinearity in graphene–silicon nitride hybrid resonator," *Nano Lett.* **20**(6), 4659–4666 (2020).
- ²³⁸Z. Shi, H. Lu, L. Zhang, R. Yang, Y. Wang, D. Liu, H. Guo, D. Shi, H. Gao, E. Wang, and G. Zhang, "Studies of graphene-based nanoelectromechanical switches," *Nano Res.* **5**(2), 82–87 (February 2012).
- ²³⁹K. M. Milaninia, M. A. Baldo, A. Reina, and J. Kong, "All graphene electromechanical switch fabricated by chemical vapor deposition," *Appl. Phys. Lett.* **95**(18), 183105 (2009).
- ²⁴⁰P. Li, Z. You, G. Haugstad, and T. Cui, "Graphene fixed-end beam arrays based on mechanical exfoliation," *Appl. Phys. Lett.* **98**(25), 253105 (2011).
- ²⁴¹M. Muruganathan, N. H. Van, M. E. Schmidt, and H. Mizuta, "Sub 0.5 volt graphene-hBN van der Waals nanoelectromechanical (NEM) switches," *Adv. Funct. Mater.* **32**(52), 2209151 (2022).
- ²⁴²S. M. Kim, E. B. Song, S. Lee, S. Seo, D. H. Seo, Y. Hwang, R. Candler, and K. L. Wang, "Suspended few-layer graphene beam electromechanical switch with

- abrupt on-off characteristics and minimal leakage current," *Appl. Phys. Lett.* **99**(2), 023103 (2011).
- ²⁴³X. Liu, J. W. Suk, N. G. Boddeti, L. Cantley, L. Wang, J. M. Gray, H. J. Hall, V. M. Bright, C. T. Rogers, M. L. Dunn, R. S. Ruoff, and J. S. Bunch, "Large arrays and properties of 3-terminal graphene nanoelectromechanical switches," *Adv. Mater.* **26**(10), 1571–1576 (2014).
- ²⁴⁴H. Tian, D. Xie, Y. Yang, T.-L. Ren, Y.-F. Wang, C.-J. Zhou, P.-G. Peng, L.-G. Wang, and L.-T. Liu, "Single-layer graphene sound-emitting devices: Experiments and modeling," *Nanoscale* **4**, 2272–2277 (2012).
- ²⁴⁵J. W. Suk, K. Kirk, Y. Hao, N. A. Hall, and R. S. Ruoff, "Thermoacoustic sound generation from monolayer graphene for transparent and flexible sound sources," *Adv. Mater.* **24**(47), 6342–6347 (2012).
- ²⁴⁶Q. Zhou and A. Zettl, "Electrostatic graphene loudspeaker," *Appl. Phys. Lett.* **102**(22), 223109 (2013).
- ²⁴⁷P. Li, G. Jing, B. Zhang, S. Sando, and T. Cui, "Single-crystalline monolayer and multilayer graphene nano switches," *Appl. Phys. Lett.* **104**(11), 113110 (2014).
- ²⁴⁸T. Cao, T. Hu, and Y. Zhao, "Research status and development trend of MEMS switches: A review," *Micromachines* **11**(7), 694 (2020).
- ²⁴⁹S. Wagner, C. Yim, N. McEvoy, S. Kataria, V. Yokaribas, A. Kuc, S. Pindl, C.-P. Fritzen, T. Heine, G. S. Duesberg, and M. C. Lemme, "Highly sensitive electromechanical piezoresistive pressure sensors based on large-area layered PtSe₂ films," *Nano Lett.* **18**(6), 3738–3745 (2018).
- ²⁵⁰A. D. Smith, F. Niklaus, A. Paussa, S. Vaziri, A. C. Fischer, M. Sterner, F. Forsberg, A. Delin, D. Esseni, P. Palestri, M. Östling, and M. C. Lemme, "Electromechanical piezoresistive sensing in suspended graphene membranes," *Nano Lett.* **13**(7), 3237–3242 (2013).
- ²⁵¹Q. Wang, W. Hong, and L. Dong, "Graphene 'microdrums' on a freestanding perforated thin membrane for high sensitivity MEMS pressure sensors," *Nanoscale* **8**, 7663–7671 (2016).
- ²⁵²D. Davidovikj, P. H. Scheepers, H. S. J. van der Zant, and P. G. Steeneken, "Static capacitive pressure sensing using a single graphene drum," *ACS Appl. Mater. Interfaces* **9**(49), 43205–43210 (2017).
- ²⁵³M. Šiškins, M. Lee, D. Wehenkel, R. van Rijn, T. W. de Jong, J. R. Renshof, B. C. Hopman, W. S. J. M. Peters, D. Davidovikj, H. S. J. van der Zant, and P. G. Steeneken, "Sensitive capacitive pressure sensors based on graphene membrane arrays," *Microsyst. Nanoeng.* **6**(1), 102 (2020).
- ²⁵⁴G. J. Verbiest, J. N. Kirchhoff, J. Sonntag, M. Goldsche, T. Khodkov, and C. Stampfer, "Detecting ultrasound vibrations with graphene resonators," *Nano Lett.* **18**(8), 5132–5137 (2018).
- ²⁵⁵C. Li, X. Gao, T. Guo, J. Xiao, S. Fan, and W. Jin, "Analyzing the applicability of miniature ultra-high sensitivity Fabry–Perot acoustic sensor using a nano-thick graphene diaphragm," *Meas. Sci. Technol.* **26**(8), 085101 (2015).
- ²⁵⁶F. Yu, Q. Liu, X. Gan, M. Hu, T. Zhang, C. Li, F. Kang, M. Terrones, and R. Lv, "Ultrasensitive pressure detection of few-layer MoS₂," *Adv. Mater.* **29**(4), 1603266 (2017).
- ²⁵⁷W. Ni, P. Lu, X. Fu, W. Zhang, P. P. Shum, H. Sun, C. Yang, D. Liu, and J. Zhang, "Ultrathin graphene diaphragm-based extrinsic Fabry–Perot interferometer for ultra-wideband fiber optic acoustic sensing," *Opt. Express* **26**(16), 20758–20767 (2018).
- ²⁵⁸X. Fan, F. Forsberg, A. D. Smith, S. Schröder, S. Wagner, H. Rödjemård, A. C. Fischer, M. Östling, M. C. Lemme, and F. Niklaus, "Graphene ribbons with suspended masses as transducers in ultra-small nanoelectromechanical accelerometers," *Nat. Electron.* **2**(9), 394–404 (2019).
- ²⁵⁹M. Muruganathan, H. Miyashita, J. Kulothungan, M. E. Schmidt, and H. Mizuta, "Zeptogram level mass sensing of light weight gas molecules using graphene nanomechanical (GNEM) resonator," in *2018 IEEE SENSORS*, New Delhi, India (IEEE, 2018), pp. 1–4.
- ²⁶⁰A. Blaikie, D. Miller, and B. J. Alemán, "A fast and sensitive room-temperature graphene nanomechanical bolometer," *Nat. Commun.* **10**(1), 4726 (2019).
- ²⁶¹I. E. Rosloń, A. Japaridze, P. G. Steeneken, C. Dekker, and F. Alijani, "Probing nanomotion of single bacteria with graphene drums," *Nat. Nanotechnol.* **17**, 637–642 (2022).
- ²⁶²Q. Wang, Y. Wang, and L. Dong, "MEMS flow sensor using suspended graphene diaphragm with microhole arrays," *J. Microelectromech. Syst.* **27**(6), 951–953 (2018).
- ²⁶³R. Pezone, G. Baglioni, P. M. Sarro, P. G. Steeneken, and S. Vollebregt, "Sensitive transfer-free wafer-scale graphene microphones," *ACS Appl. Mater. Interfaces* **14**(18), 21705–21712 (2022).
- ²⁶⁴Q. Zhou, J. Zheng, S. Onishi, M. F. Crommie, and A. K. Zettl, "Graphene electrostatic microphone and ultrasonic radio," *Proc. Natl. Acad. Sci. U. S. A.* **112**(29), 8942–8946 (2015).
- ²⁶⁵D. Todorović, A. Matković, M. Milićević, D. Jovanović, R. Gajić, I. Salom, and M. Spasenović, "Multilayer graphene condenser microphone," *2D Mater.* **2**(4), 045013 (2015).
- ²⁶⁶D. R. Southworth, H. G. Craighead, and J. M. Parpia, "Pressure dependent resonant frequency of micromechanical drumhead resonators," *Appl. Phys. Lett.* **94**(21), 213506 (2009).
- ²⁶⁷F. Ejéian, S. Azadi, A. Razmjou, Y. Orooji, A. Kottapalli, M. Ebrahimi Warkiani, and M. Asadnia, "Design and applications of MEMS flow sensors: A review," *Sens. Actuators, A* **295**, 483–502 (2019).
- ²⁶⁸A. A. Yazdi, J. Xu, and V. Berry, "Phononics of graphene interfaced with flowing ionic fluid: An avenue for high spatial resolution flow sensor applications," *ACS Nano* **15**(4), 6998–7005 (2021).
- ²⁶⁹W. Wang, N. Wu, Y. Tian, C. Niezrecki, and X. Wang, "Miniature all-silica optical fiber pressure sensor with an ultrathin uniform diaphragm," *Opt. Express* **18**(9), 9006–9014 (2010).
- ²⁷⁰F. Xu, D. Ren, X. Shi, C. Li, W. Lu, L. Lu, L. Lu, and B. Yu, "High-sensitivity Fabry–Perot interferometric pressure sensor based on a nanothick silver diaphragm," *Opt. Lett.* **37**(2), 133–135 (2012).
- ²⁷¹L. Laurent, J.-J. Yon, J.-S. Moulet, M. Roukes, and L. Duraffour, "12-μm-pitch electromechanical resonator for thermal sensing," *Phys. Rev. Appl.* **9**, 024016 (2018).
- ²⁷²T. Endoh, S. Tohyama, T. Yamazaki, Y. Tanaka, K. Okuyama, S. Kurashina, M. Miyoshi, K. Katoh, T. Yamamoto, Y. Okuda, T. Sasaki, H. Ishizaki, T. Nakajima, K. Shinoda, and T. Tsuchiya, "Uncooled infrared detector with 12 μm pixel pitch video graphics array," *Proc. SPIE* **8704**, 87041G (2013).
- ²⁷³U. Mizrahi, N. Argaman, S. Elkind, A. Giladi, Y. Hirsh, M. Labilov, I. Pivnik, N. Shiloah, M. Singer, A. Tuito, M. Ben-Ezra, and I. Shtrichman, "Large-format 17 μm high-end VO_x μ-bolometer infrared detector," *Proc. SPIE* **8704**, 87041H (2013).
- ²⁷⁴G. D. Skidmore, C. J. Han, and C. Li, "Uncooled microbolometers at DRS and elsewhere through 2013," *Proc. SPIE* **9100**, 910003 (2013).
- ²⁷⁵T.-S. Wung, Y.-T. Ning, K.-H. Chang, S. Tang, and Y.-X. Tsai, "Vertical-plate-type microaccelerometer with high linearity and low cross-axis sensitivity," *Sens. Actuators, A* **222**, 284–292 (2015).
- ²⁷⁶A. L. Roy and T. K. Bhattacharyya, "Design, fabrication and characterization of high performance SOI MEMS piezoresistive accelerometers," *Microsyst. Technol.* **21**(1), 55–63 (2015).
- ²⁷⁷L. Zhang, J. Lu, Y. Kurashima, H. Takagi, and R. Maeda, "Development and application of planar piezoresistive vibration sensor," *Microelectron. Eng.* **119**, 70–74 (2014).
- ²⁷⁸E. Cabruja, A. Collado, J. A. Plaza, and J. Esteve, "Piezoresistive accelerometers for MCM-package—Part II: The packaging," *J. Microelectromech. Syst.* **14**(4), 806–811 (2005).
- ²⁷⁹X. Song, M. Oksanen, J. Li, P. J. Hakonen, and M. A. Sillanpää, "Graphene optomechanics realized at microwave frequencies," *Phys. Rev. Lett.* **113**, 027404 (2014).
- ²⁸⁰J. Moser, J. Güttinger, A. Eichler, M. J. Esplandiu, D. E. Liu, M. I. Dykman, and A. Bachtold, "Ultrasensitive force detection with a nanotube mechanical resonator," *Nat. Nanotechnol.* **8**(7), 493–496 (2013).
- ²⁸¹Y. Ying, Z.-Z. Zhang, J. Moser, Z.-J. Su, X.-X. Song, and G.-P. Guo, "Sliding nanomechanical resonators," *Nat. Commun.* **13**(1), 6392 (2022).
- ²⁸²H. Conley, N. V. Lavrik, D. Prasai, and K. I. Bolotin, "Graphene bimetallic-like cantilevers: Probing graphene/substrate interactions," *Nano Lett.* **11**(11), 4748–4752 (2011).
- ²⁸³V. Singh, B. Irfan, G. Subramanian, H. S. Solanki, S. Sengupta, S. Dubey, A. Kumar, S. Ramakrishnan, and M. M. Deshmukh, "Coupling between quantum Hall state and electromechanics in suspended graphene resonator," *Appl. Phys. Lett.* **100**(23), 233103 (2012).
- ²⁸⁴H. Gao, H. Gao, J. Suh, J. Suh, M. C. Cao, A. Y. Joe, F. Mujid, K. H. Lee, K. H. Lee, S. Xie, S. Xie, P. Poddar, J. U. Lee, J. U. Lee, K. Kang, K. Kang, P. Kim,

- D. A. Muller, and J. Park, "Tuning electrical conductance of MoS₂ monolayers through substitutional doping," *Nano Lett.* **20**(6), 4095–4101 (2020).
- ²⁸⁵J. Gao, B. Li, J. Tan, P. Chow, T. M. Lu, and N. Koratkar, "Aging of transition metal dichalcogenide monolayers," *ACS Nano* **10**(2), 2628–2635 (2016).
- ²⁸⁶K. Kang, K. H. Lee, Y. Han, H. Gao, S. Xie, D. A. Muller, and J. Park, "Layer-by-layer assembly of two-dimensional materials into wafer-scale heterostructures," *Nature* **550**, 229–233 (2017).
- ²⁸⁷D. Neumaier, S. Pindl, and M. C. Lemme, "Integrating graphene into semiconductor fabrication lines," *Nat. Mater.* **18**(6), 525–529 (2019).
- ²⁸⁸A. Quellmalz, X. Wang, S. Sawallich, B. Uzlu, M. Otto, S. Wagner, Z. Wang, M. Precht, O. Hartwig, S. Luo, G. S. Duesberg, M. C. Lemme, K. B. Gylfason, N. Roxhed, G. Stemme, and F. Niklaus, "Large-area integration of two-dimensional materials and their heterostructures by wafer bonding," *Nat. Commun.* **12**(1), 917 (2021).
- ²⁸⁹Ora graphene audio, accessed on dec. 30, 2022 at <https://www.ora-sound.com/gq-headphones>.
- ²⁹⁰Graphaudio, accessed on dec. 30, 2022 at <https://www.graphaudio.com>.
- ²⁹¹M. K. Blees, A. W. Barnard, P. A. Rose, S. P. Roberts, K. L. McGill, P. Y. Huang, A. R. Ruyack, J. W. Kevek, B. Kobrin, D. A. Muller, and P. L. McEuen, "Graphene kirigami," *Nature* **524**(7564), 204–207 (2015).
- ²⁹²M. Z. Miskin, K. J. Dorsey, B. Bircan, Y. Han, D. A. Muller, P. L. McEuen, and I. Cohen, "Graphene-based bimorphs for micron-sized, autonomous origami machines," *Proc. Natl. Acad. Sci. U. S. A.* **115**(3), 466–470 (2018).
- ²⁹³M. Z. Miskin, A. J. Cortese, K. Dorsey, E. P. Esposito, M. F. Reynolds, Q. Liu, M. Cao, D. A. Muller, P. L. McEuen, and I. Cohen, "Electronically integrated, mass-manufactured, microscopic robots," *Nature* **584**(7822), 557–561 (2020).
- ²⁹⁴M. F. Reynolds, K. L. McGill, M. A. Wang, H. Gao, F. Mujid, K. Kang, J. Park, M. Z. Miskin, I. Cohen, and P. L. McEuen, "Capillary origami with atomically thin membranes," *Nano Lett.* **19**(9), 6221–6226 (2019).
- ²⁹⁵W. Xu, Z. Qin, C.-T. Chen, H. R. Kwag, Q. Ma, A. Sarkar, M. J. Buehler, and D. H. Gracias, "Ultrathin thermoresponsive self-folding 3D graphene," *Sci. Adv.* **3**(10), e1701084 (2017).
- ²⁹⁶A. Castellanos-Gomez, R. Roldán, E. Cappelluti, M. Buscema, F. Guinea, H. S. J. van der Zant, and G. A. Steele, "Local strain engineering in atomically thin MoS₂," *Nano Lett.* **13**(11), 5361–5366 (2013).
- ²⁹⁷A. R. Rezk, B. Carey, A. F. Chrimis, D. W. M. Lau, B. C. Gibson, C. Zheng, M. S. Fuhrer, L. Y. Yeo, and K. Kalantar-zadeh, "Acoustically-driven trion and exciton modulation in piezoelectric two-dimensional MoS₂," *Nano Lett.* **16**(2), 849–855 (2016).
- ²⁹⁸R. Peng, A. Ripin, Y. Ye, J. Zhu, C. Wu, S. Lee, H. Li, T. Taniguchi, K. Watanabe, T. Cao, X. Xu, and M. Li, "Long-range transport of 2D excitons with acoustic waves," *Nat. Commun.* **13**(1), 1334 (2022).
- ²⁹⁹K. Datta, Z. Lyu, Z. Li, T. Taniguchi, K. Watanabe, and P. B. Deotare, "Spatiotemporally controlled room-temperature exciton transport under dynamic strain," *Nat. Photonics* **16**(3), 242–247 (2022).
- ³⁰⁰D. Hatanaka, A. Bachtold, and H. Yamaguchi, "Electrostatically induced photonic crystal," *Phys. Rev. Appl.* **11**, 024024 (2019).
- ³⁰¹P. Delsing, A. N. Cleland, M. J. A. Schuetz, J. Knörzer, G. Giedke, J. I. Cirac, K. Srinivasan, M. Wu, K. C. Balram, C. Bäuerle, T. Meunier, C. J. B. Ford, P. V. Santos, E. Cerdá-Méndez, H. Wang, H. J. Krenner, E. D. S. Nysten, M. Weiß, G. R. Nash, L. Thevenard, C. Gourdon, P. Rovillain, M. Marangolo, J.-Y. Duquesne, G. Fischerauer, W. Ruile, A. Reiner, B. Paschke, D. Denysenko, D. Volkmer, A. Wixforth, H. Bruus, M. Wiklund, J. Reboud, J. M. Cooper, Y. Fu, M. S. Brugger, F. Rehfeldt, and C. Westerhausen, "The 2019 surface acoustic waves roadmap," *J. Phys. D* **52**(35), 353001 (2019).
- ³⁰²T. Chari, R. Ribeiro-Palau, C. R. Dean, and K. Shepard, "Resistivity of rotated graphite-graphene contacts," *Nano Lett.* **16**(7), 4477–4482 (2016).
- ³⁰³R. Ribeiro-Palau, C. Zhang, K. Watanabe, T. Taniguchi, J. Hone, and C. R. Dean, "Twistable electronics with dynamically rotatable heterostructures," *Science* **361**(6403), 690–693 (2018).
- ³⁰⁴N. R. Finney, M. Yankowitz, L. Muraleetharan, K. Watanabe, T. Taniguchi, C. R. Dean, and J. Hone, "Tunable crystal symmetry in graphene–boron nitride heterostructures with coexisting moiré superlattices," *Nat. Nanotechnol.* **14**, 1029 (2019).
- ³⁰⁵X. Huang, L. Lin, and Q. Zheng, "Theoretical study of superlubric nanogenerators with superb performances," *Nano Energy* **70**, 104494 (2020).
- ³⁰⁶M. Luo, Z. Zhang, and B. I. Yakobson, "Tunable gigahertz oscillators of gliding incommensurate bilayer graphene sheets," *J. Appl. Mech.* **80**(4), 040906 (2013).
- ³⁰⁷S. Young Kim, S.-Y. Cho, K.-S. Kim, and J. Won Kang, "Developing nanoscale inertial sensor based on graphite-flake with self-retracting motion," *Physica E* **50**, 44–50 (2013).
- ³⁰⁸U. T. Duerig, A. W. Knoll, E. Koren, and E. Loertscher, "Electromechanical switching device with electrodes having 2D layered materials with distinct functional areas," U.S. Patent 10,546,708 (28 January 2020).
- ³⁰⁹X. Huang, X. Xiang, J. Nie, D. Peng, F. Yang, Z. Wu, H. Jiang, Z. Xu, and Q. Zheng, "Microscale Schottky superlubric generator with high direct-current density and ultralong life," *Nat. Commun.* **12**(1), 2268 (2021).
- ³¹⁰J. Lee, M. D. LaHaye, and P. X.-L. Feng, "Design of strongly nonlinear graphene nanoelectromechanical systems in quantum regime," *Appl. Phys. Lett.* **120**(1), 014001 (2022).
- ³¹¹C. Urgell, W. Yang, S. L. De Bonis, C. Samanta, M. J. Esplandiu, Q. Dong, Y. Jin, and A. Bachtold, "Cooling and self-oscillation in a nanotube electromechanical resonator," *Nat. Phys.* **16**(1), 32–37 (2020).
- ³¹²M. Tasnimul Haque, M. Will, A. Zyuzin, D. Golubev, and P. Hakonen, "Thermal self-oscillations in monolayer graphene coupled to a superconducting microwave cavity," *New J. Phys.* **24**, 103008 (2022).
- ³¹³N. Lörch, J. Qian, A. Clerk, F. Marquardt, and K. Hammerer, "Laser theory for optomechanics: Limit cycles in the quantum regime," *Phys. Rev. X* **4**, 011015 (2014).
- ³¹⁴J. Qian, A. A. Clerk, K. Hammerer, and F. Marquardt, "Quantum signatures of the optomechanical instability," *Phys. Rev. Lett.* **109**, 253601 (2012).